UNIVERSITÀ DEGLI STUDI DI BERGAMO
Facoltà di Ingegneria
Dipartimento di Ingegneria Industriale

DOTTORATO DI RICERCA
IN
TECNOLOGIE PER L'ENERGIA E L'AMBIENTE

XXV ciclo

anno 2014

AERO-THERMAL PERFORMANCE OF A FILM-COOLED HIGH PRESSURE TURBINE BLADE/VANE: A TEST CASE FOR NUMERICAL CODES VALIDATION

Doctoral thesis:
Fabrizio Fontaneto

Supervisor:
Prof. Giovanna Barigozzi

Dipartimento di Ingegneria Industriale. Università degli studi di Bergamo
ISBN XXX-XX-XXXXX-XX-X
Open access copy available at: http://hdl.handle.net/XXXXX/XXXXX

Abstract

Nowadays companies are making a massive use of Computational Fluid Dynamics (CFD) since the early stages of the development of new components. Given therefore the critical role that numerical codes are playing, their reliability must be rigorously checked through detailed comparisons between numerical and experimental results. The present thesis concentrates on the experimental activity carried in the frame of two different measurement campaigns, both focused on the creation of an experimental test-case for turbomachinery codes validation.
The first experimental activity, funded by "Ansaldo Energia" and carried out at the *Energy Systems and Turbomachinery Laboratory* of the University of Bergamo (Italy), dealt with the characterization of the effect that the endwall cooling system of a high pressure turbine rotor has on both, the thermal and the aerodynamic performance, with a particular attention paid to the study of the interaction between the cooling jets and secondary flows. Starting from the original geometry, a full-scale model was designed and tested in an open-loop suction-type wind tunnel as a seven blade linear cascade. Aerodynamic measurements, performed by means of a 5-hole miniaturized pressure probe, evidenced a marked asymmetry of the secondary flows between the upper and the lower semi-channels. The latter had to be related to the presence of the fillet between the blade and the cooled endwall and it demonstrated to provide a significant reduction of

the aerodynamic losses. Injection seemed not to affect at all the secondary flows pattern: at every injection rate, the cooling jets kept attached to the endwall surface and confined in the boundary layer. Such a result was confirmed by the adiabatic effectiveness distribution which was retrieved by thermochromic liquid crystals. The thermal protection was continuously growing with the injection rate and no separation was identified. The high performance of the cooling system had to be related to the extreme tangential arrangement of the holes. In the end, a good agreement was found between the experimental data and the results of simulations run by the company.
The second measurement campaign was held at the von Karman Institute for Fluid Dynamics (VKI) (Belgium) and funded by the Japanese Central Research Institute of Electric Power Industry (CRIEPI). A film-cooled transonic turbine vane was investigated in a five blades linear cascade configuration and at engine-like conditions in terms of Reynolds number and Mach number. The inlet free-stream turbulence was fully characterized by means of hot-wire anemometry: the evolution along the inlet channel of the turbulence intensity, of the turbulent kinetic energy and of the turbulence scales all showed results in complete agreement with partial past results and literature. The aerodynamic performance of the cascade was assessed by traversing a 3-hole pressure probe in the downstream section. Injection was found to slightly enhance total pressure wakes, with a weak increase in terms of aerodynamic losses. In particular, it has been demonstrated how, in supersonic conditions, the presence of a strong shock in the rear part of the suction side is responsible for a marked degradation of the performance of the cascade. Thin-films thermometers have been used to retrieve the blade convective heat transfer coefficient (h) distribution. The non-cooled tests demonstrated that, for every main-stream condition, the tripping effect of the film-cooling holes is the responsible for a transition of the boundary layer state. The thermal protection of the suction side always increases with the injection rate, showing therefore a high resistance to separation. On the pressure side, on the contrary, the portion of the blade surface placed immediately downstream the injection point is characterised by values of h higher than those of the non-cooled case: already at

low injection rates, the coolant momentum is high enough to break down the boundary layer, putting therefore in direct contact the blade surface with the hot main-stream. In any case, the rear part of the pressure side always benefits from an enhanced injection.

Contents

List of Figures

List of Tables

Nomenclature

Roman Symbols

A	Area	[m^2]
C	Chord	[m]
C_{ax}	Axial chord	[m]
c_p	Isobaric specific heat	[$Jkg^{-1}K^{-1}$]
d	Diameter	[m]
E_b	Wheatstone's bridge output	[V]
f_s	Sampling frequency	[Hz]
g	Pitch	[m]
H	Blade height	[m]
h	Convective heat transfer coefficient	[W/m^2K]
I	Momentum-flux ratio	[-]
k	Thermal conductivity	[$Wm^{-1}K^{-1}$]
K	Turbulent kinetic energy	[$J\ Kg^{-1}$]
$\dot{m}$	Mass-flow	[kgs^{-1}]
L_1	Integral length scale	[m]
M_{inlet}	Inlet loss-free blowing ratio	[-]
Ma	Mach number	[-]
Nu	Nusselt number	[-]
o	Throat	[m]
P	Pressure	[Pa]
$\dot{q}$	Heat flux	[Wm^{-2}]
R	Radius	[m]

Re	Reynolds number	[-]
S	Curvilinear abscissa	[m]
t	Time	[s]
T	Temperature	[K]
Tu	Turbulence intensity	[%]

Greek Symbols

α	Thermal diffusivity	[m^2s^{-1}]
β	Relative flow angle	[°]
Δ	Variation, difference	[-]
ϵ	Turbulence decay	[J Kg^{-1} s^{-1}]
η	Temperature recovery factor	[-]
η_{aw}	Film-cooling adiabatic effectiveness	[-]
γ	Specific heat ratio	[-]
λ_1	Taylor's length scale	[m]
μ	Dynamic viscosity	[Pa·s]
Ω	Non-dimensional vorticity	[-]
ρ	Density	[kgm^{-3}]
ζ	Kinetic loss coefficient	[-]
ζ_{th}	Thermodynamic loss coefficient	[-]

Subscript

ax	Axial direction
aw	Adiabatic wall
c	Relative to cooling, coolant stream
$hole$	Relative to hole's exit section
$init$	Initial
s	Isentropic
ref	Reference value

tip	Relative to tip, rotor blade tip
tg	Tangential direction, turbine axis
w	Wall, relative to the surface
wire	Relative to hot-wire sensing element
0	Total quantity, absolute conditions
1	Cascade inlet
2	Cascade exit
∞	Relative to main-stream

Acronyms

BR	Blowing ratio, mass-flux ratio
CC	Constant current
Cd	Discharge coefficient
CFD	Computational Fluid Dynamics
DR	Density ratio
FFT	Fast Fourier Transform
HW	Hot-wire
HWA	Hot-wire anemometry
LE	Leading edge
LDV	Laser doppler velocimetry
MFR	mass-flow ratio
PS	Pressure Side
RANS	Reynolds Averaged Navier-Stokes solver
SS	Suction Side
TC	ThermoCouple
TE	Trailing Edge
TF	Transfer function
TLCs	Thermochromic liquid crystals
VKI	von Karman Institute for Fluid Dynamics

Chapter 1

Introduction

1.1 The role of experimentation in the development of CFD codes

Nobody talks any more of replacement of wind tunnels by the computer and I am really happy to find that - *Peter Sacher 1988*

This is what Peter Sacher, in his quality of Technical Evaluator of the Advisory Group For Aerospace Research and Development (AGARD), concluded at the end of the symposium titled "Validation of Computational Fluid Dynamics", held in Lisbon in 1988 [65]. In the previous years in fact, the trend of growth of computational power joined with improvements made in the field of Computational Fluid Dynamics (CFD), were letting the expectations of scientists flying high. It did not take too much time, anyway, to realize that any numerical improvement could not exclude a solid experimental base.

As soon as numericists started spending their efforts in the development of more sophisticated models, the lack of completeness of experimental campaigns became immediately clear: it was impossible to retrieve in literature

a full explanatory experimental set were all the required inputs were measured. Further in [65], in the so called Round Table Discussions (RTD), it is Sacher again who gave a foreword to the synergistic research that would have been started in few years: *"I got the impression that experimental and numerical engineers are coming more and more together...this meeting is a good example for this interaction between those disciplines, which have been too long separated in the past"*. It was during the AGARD Symposium 437 [65] that, for the first time was stated the need of *ad-hoc* experiments, designed uniquely for CFD testing: the so called experimental test-cases.

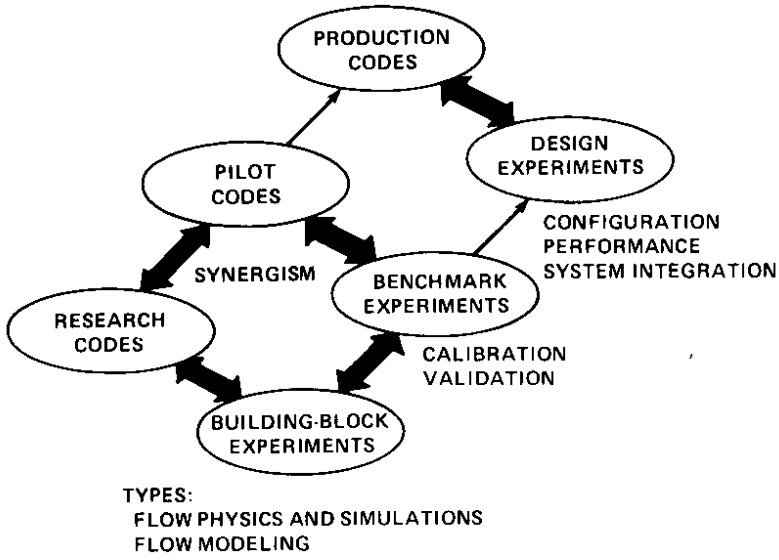

Figure 1.1: The CFD development philosophy and the role of experimentation. Marvin, 1988 [49]

Marvin [49] in 1988 gaves a clear description of the features that an experimental test case for numerical applications must provide. At first instance, the author summarized in 1.1 the development stages of a code. At the base he foresees basic fundamental experiments, performed to un-

derstand the flow physics and used to guide the development of a research code. A "pilot code" is a more mature development, it is the result of the synergistic work between the code developers and the support experimentalists and its target is in fact the parametrization of the models: at this phase, calibration and validation experiments are required to identify the range of applicability and to asses their reliability. Only in its final stage the code can be used alone (or in combination with verification experiments) since its performance is well known from the previous steps.

The concepts of "validation" and "calibration" were introduced already by Bradley [10] in 1987 but it is again Marvin the first who provided a clear definition for "CFD-validation" and "CFD-calibration" experiments. They are herein reported in their original form since they actually became accepted standards:

- ***CFD-validation experiment:*** *detailed surface and flow-field comparisons with experimental data to verify the code's ability to accurately model the critical physics of the flow. Validation can occur only when the accuracy and limitations of the experimental data are known and thoroughly understood and when the accuracy and limitations of the code's numerical algorithms, grid-density effects and physical basis are equally known and understood over a range of specified parameters.*

- ***CFD-calibration experiment:*** *the comparison of CFD code results with experimental data for realistic geometries, similar to the ones of design interest, made in order to provide a measure of the code's ability to predict specific parameters that are of importance to the design objectives without necessarily verifying that all the features of the flow are correctly modelled.*

Even though the previous definitions imply that a validation experiment can be profitably used for calibration purposes and not vice-versa, it is also clear that an experimental test-case must always show two fundamental characteristics:

- **COMPLETENESS:** besides the flow features under investigation, experimental boundary conditions must be all measured. Free stream conditions, initial conditions and test-section geometries are some examples.

- **ACCURACY:** without a clear and robust uncertainty analysis on the measured data, there is no means to quantify ranges of applicability of codes. Error estimates are a prerequisite and must be given for both, the measured variables and the boundary conditions. The methodology applied for the evaluation of uncertainties must be standardized and clearly stated in order to allow an independent assessment.

1.2 Experimental test cases for turbomachinery codes validation

In his contribution to the "Validation of Computational Fluid Dynamics" symposium [65], Povinelli resumes the laboratory activities at the Lewis Research Center (Cleveland, Ohio) in the field of turbomachinery codes validation in 1988. Emphasis is given mainly on the natural unsteadiness of turbomachinery flows and therefore on the need to validate the closure equations used in in-house unsteady Reynolds averaged Navier-Stokes codes (URANS). Different types of experiments were underway at that time on several turbomachinery components and they were all related to three main topics: measurement of the turbulent kinetic energy, shock-boundary layer interaction and boundary layer transition characterization.
These early researches in fact, defined and described a sort of "road map" for experimentalists who dealt in the following years with CFD-oriented measurements: efforts have been spent on the development of the proper instrumentation, able to provide higher frequency response and smaller measuring volumes/insertion effects, in order to fulfil the numericists needs. Other measurement campaigns were activated in those years and some of them are reported and critically revised by Hirsch at the occasion of the

AGARD lecture series 195 [38]. In his long contribution, the author firstly describes the performance of different turbulence models with respect to some experimental benchmarks and, subsequently, moves the focus on code validations for 3D turbomachinery flows. The so called *Durham turbine cascade* (see Fig. 1.2) by Gregory Smith et. al is an example of the test cases researchers were interested in at that time: a high turning turbine blade characterized by strong transitional flows. Surprisingly, 6 years after the first AGARD symposium on CFD validation, the attention was still concentrated on the flow parameters that Povinelli identified and, in fact, the conclusion of Hirsch was straight forward: he stated that a continuous effort on turbomachinery validation should have been pursued to enhance the understanding of turbulence and its effects on boundary layers, introducing new validation criteria such as Reynolds stresses, temperature profiles and heat transfer coefficient distributions.

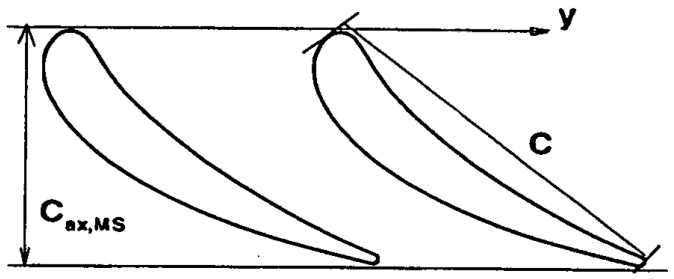

Figure 1.2: Durham cascade geometry - from Hirsch [38]

Ten years after the first validation symposium, in 1998, AGARD set up a new working group whose aim was to perform independent validations on two test cases: the NASA compressor blade 37 and a DLR turbine stator cascade (Fig. 1.3). Several codes were used and, in most of the cases, results were not in agreement with the experimental data. They were found to be unable to tackle properly the secondary flows pattern, highly underestimating the pressure loss. Massive differences were then identified in the predicted Reynolds stress values and, consequentially, in the definition of

the transition point of the boundary layer. The conclusions presented in the advisory report [22] are therefore the same ones of ten years before: *"There is still a need for detail experimental measurements as a basis for future developments in turbomachinery CFD"* and *"Similar studies should be undertaken, specifically on heat transfer predictions in turbomachinery"*.

Figure 1.3: DLR cascade geometry and computed endwall streamlines - [22]

This one-page-long story of the efforts done by AGARD over ten years to obtain solid turbomachinery test cases, gives the opportunity to summarize the salient features that an experiment must provide to be efficiently used in the validation process:

- Inlet free stream turbulence should be measured in the most explicative way possible: depending on the turbulence model used, turbulence intensity, turbulent kinetic energy, decay and length scales must be known as they are an input to the calculations.
- A wrong prediction of the position of the transition point determines a biased evolution of the boundary layer that, in turns, necessarily leads

to a wrong estimation of losses. Blade static pressure distribution can be efficiently used to tune the transition model.

- Convective heat transfer coefficient distribution provides complementary data on the boundary layer, allowing the identification of its precise state at different positions along the blade surface.

- Upstream and downstream main flow quantities are inputs to the codes (e.g. total inlet pressure and temperature, downstream static pressure). As suggested by several authors in the works cited previously, integral parameters such as an average loss coefficient are always a useful benchmark to quantify the goodness of the prediction.

1.3 Motivation of the doctoral thesis

Even though the attention on basic flow understanding experiments is still active, the quest now is strongly devoted to the parametrization of predictions as they are still geometry/conditions dependent. Moreover, since companies are making a massive use of CFD as a primary design tool, nowadays a boost in the direction of codes validation comes mostly from industries that are either running commercial or in-house codes.
The present manuscript reports on the experimental activity performed in the frame of two different measurement campaigns requested by two different industrial entities. Both of them aimed at performing a detailed aero-thermal characterization of typical high pressure turbine geometries, in the view of providing the companies with reliable data to benchmark the performance and the limits of the normally used CFD tools.

The first activity, funded by "Ansaldo Energia" and entirely carried out at the *Energy Systems and Turbomachinery Laboratory* of the University of Bergamo (Italy), was justified be the need of the company to calibrate the in-house code on the new design of the first stage rotor geometry of a land-based gas turbine. The measurements aimed at quantifying the effect

on the thermal protection and on the aerodynamic performance due the presence of a rack of ten film-cooling holes on the endwall of a linear rotor blade cascade. The endwall adiabatic film-cooling effectiveness and the aerodynamic efficiency of the cascade was investigated for several injection rates in subsonic conditions.

The second part of the doctoral thesis describes the experimental campaign held at the *von Karman Institute for Fluid Dynamics* (VKI) (Belgium) in order to provide the Japanese "Central Research Institute of Electric Power Industry" (CRIEPI) with an experimental test-case for validation purposes. The project, that actually configures itself as a follow-up of the efforts done previously at VKI in the frame of codes validation [6], dealt with the aero-thermal characterization of a high pressure turbine stator blade, cooled by two rows of staggered holes on both, the suction and the pressure sides. The model was investigated at different Reynolds numbers and Mach numbers, ranging from high-subsonic to low-supersonic conditions. Besides the main-stream quantities, the inlet free-stream turbulence was carefully quantified by means of hot-wire anemometry while the downstream total pressure wakes and the blade convective heat transfer coefficient distribution were assessed by the use of a 3-hole pneumatic pressure probe and of thin-films gages respectively. Thermal and aerodynamic measurements were performed at several injection conditions and cooling flow temperatures.

In the following chapters, a brief introduction to the film-cooling technology will be firstly given. The target is to identify the parameters defining the quality of a film-cooling ejection and the physical quantities that must be measured for their computation. Successively, the measurement techniques will be introduced with the intent of providing the complete experimental boundary conditions and techniques limitations. In the end, the two different experimental investigations will be described in detail: the test-section geometry, the facilities and the test conditions will be pointed out while results will be presented and discussed in depth. The uncertainty analysis will be always given at the end.

Chapter 2

Film-cooling technology

2.1 Overview on film-cooling technology

Historically, the first cooling technology introduced in turbomachinery was the so called *internal cooling*. The coolant flow was made passing through internal U-shaped channels to be discharged then in the main-stream through the trailing edge of the blade. This practice supported the development of gas turbine engines until the 1950 when military and commercial engines started to be equipped with film-cooling. The impact of its introduction on the development of new engines was crucial: the firing temperatures started to grow at a higher rate (Fig. 2.1) and so did the overall pressure ratio (Fig. 2.2), following exactly the same trend. If one now compares the evolution of the film-cooling effectiveness over the years (Fig. 2.3), it is straight forward to understand that the performance of modern machines in terms of power and efficiency are strongly related to the improvements achieved in the quality of the thermal protection.

The previous considerations allow to draw a first important conclusion: the film-cooling technology grant to highly increase the turbine inlet temperature (TIT) further over the metal maximum allowable limit ($\sim$1200 [K]). The physical principle on which it is based can be understood by the

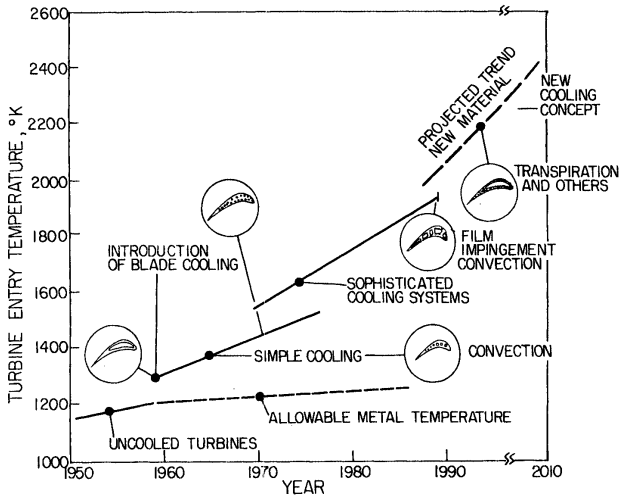

Figure 2.1: Turbine inlet temperature increase with respect to the evolution of the cooling technologies - from Lakshminarayana [45]

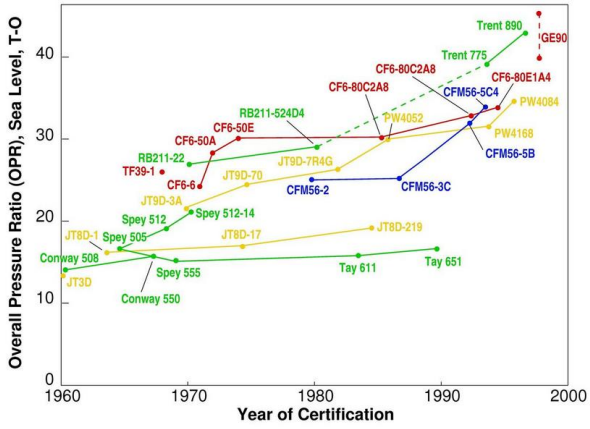

Figure 2.2: Time Evolution of the overall pressure ratio for different families of gas turbine engines - from Jane's Aero-Engines book [33]

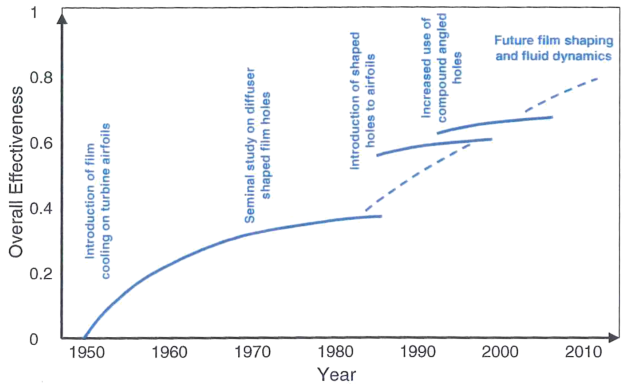

Figure 2.3: Overall cooling effectiveness progression in function of the evolution of the film-cooling technology - from Bunker [12]

simplified case depicted in the following figures. By placing a thin layer of air (Fig. 2.4-b) at a temperature $T_{film} < T_{flow}$, the temperature of the metal at the surface T_w tends to be lower than for the original case (Fig. 2.4-a) leading, moreover, to a reduced heat load and lower thermal stresses.

Generally speaking, the phenomenon introduced above, has its best effectiveness when the film remains attached to the solid interface, covering homogeneously the complete surface: a condition that directly tends to the limit of a porous substrate, through which the coolant is ejected. Nowadays, research is still far producing a material that grants a porous ejection and a good structural resistance and this is why, historically, great efforts have been spent in simulating such a homogeneous protection by means of discrete holes racks. In his contribution to the lecture series on film-cooling held at VKI in 2007 [12], Bunker described the methodology applied to the design of the cooling system of a modern gas turbine. Once the so called "cooling budget" (the percentage of total mass-flow processed by the compressor and used for cooling) is defined, it is distributed on every component that needs to be cooled. At this stage, the number and the shape of holes as well as their position on the surfaces is already determined: besides the required thermal protection, decisions are taken also considering the impact

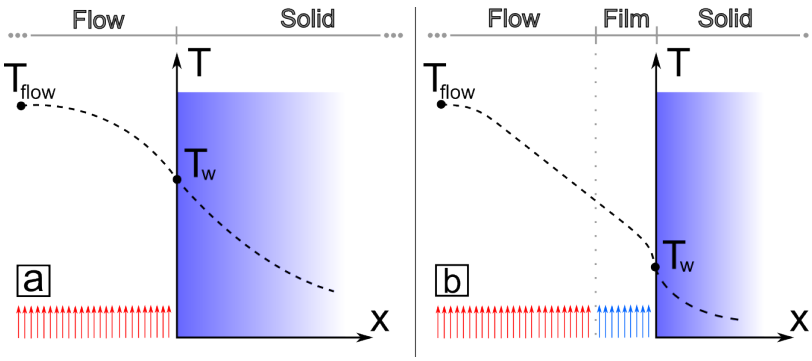

Figure 2.4: Qualitative flow temperature gradient (a) without film-cooling and (b) with film-cooling protection

on aerodynamic losses, structural resistance of the cooled component and easiness in manufacturing and repairing. It is clear that such a process is naturally iterative and fundamentally based on the company experience, built over the years by both experimental and numerical investigations.

2.2 Phenomenology of film-cooling

The long list of components and parameters that are involved in the design of the cooling system is an indicator of the crucial role that this technique is playing in modern engines. At this point, therefore, it is worth to revise the physics of coolant ejection from both the points of view, the aerodynamic and the thermal one, with the intent of introducing and describing the parameters on which the cooling performance is normally assessed.

2.2.1 Convective heat flux in film-cooling

One of the basic targets of film-cooling is the reduction of the heat flux "transmitted" to the blade. Discarding the effect of radiation, then the energy exchange in a typical turbomachinery component can be modelled by means of the Newton's law of convection (Eq. 2.1):

$$\dot{q} = h\Delta T = h(T_{source} - T_{sink}) \tag{2.1}$$

The previous equation states that the transmitted convective heat flux depends upon two parameters: the convective heat transfer coefficient "h" and a driving temperature differential. The first parameter describes the tendency of the flow to release the heat while the second defines the direction of the energy transfer (from flow to wall or vice-versa) and the potential amount of energy that can be released.
Basing on these considerations, one can assume therefore that the convective heat transfer coefficient carries both the information, about the type of fluid involved and of the flow field itself. More in detail, this assumption holds true if viscosity is constant (or, more in general, if it is not a strong function of temperature) and if the effect of buoyancy can be neglected from the problem. Since it can be assumed that a typical turbine stage operates for the majority of the time at constant temperature and constant pressure and in a forced convection condition, the latter approximation can be therefore profitably taken.

As mentioned previously in Sec. 2.1, a film-cooling protection implies the existence of a layer of "cold" air flowing over a surface. The full description of the problem must take into account therefore the different temperatures of the flows ($T_{0\infty}$ and T_{0c}) as well as the temperature of the surface T_w. Moreover, since we have an interface between two different flows, also the effect of the mixing in the shear layer must play a role. This condition leads to a certain degree of indetermination of the driving temperature potential: if, on one hand, T_{sink} in Eq. 2.1 is necessarily equal to T_w, it is also true that taking $T_{source} = T_{0\infty}$ omits completely the effect of mixing while $T_{source} = T_{0c}$ can not be clearly defined because of the temperature gradient acting through the height of the film (function of the mixing process and of the different temperatures).

Because of the reasons explained right above, in film-cooling the effective thermal driving potential for the phenomenon is identified in the temperature at which the flow is set by the mixing process: the so called

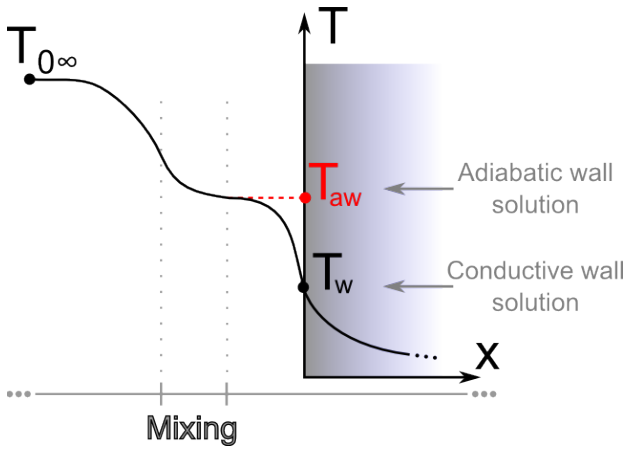

Figure 2.5: Comparison of the temperature gradient generated in the flow with an adiabatic wall condition (red line) and with a conductive wall condition (black line)

"adiabatic wall temperature" (T_{aw}). The latter is in fact the temperature that the cooling film would assume if the wall would have been adiabatic, as pictured in Fig. 2.5. Imposing T_{aw} as the source of the heat transfer is anyway an assumption that is valid only if the thermal boundary layer is thin compared to height of the film layer. By comparing adiabatic wall and conducting wall simulations, Harrison [37] (Cited by Bogard in [12]) demonstrated how the wall heat transfer can be locally wrong while the overall value is well described.

$$\dot{q} = h(T_{aw} - T_w) \tag{2.2}$$

By inserting therefore the adiabatic wall temperature in Eq. 2.1, one obtains the formulation reported in Eq. 2.2 that actually allows to derive some more conclusions. From the latter it is in fact clear that when T_w equals T_{aw}, the heat transferred to the blade surface nulls while, at the same time, the wall temperature increases (see Fig. 2.5). In order therefore to qualify the goodness of a film-cooling protection, one should take

into account two performance parameters, the first being the wall temperature (that should be lower than the maximum allowable temperature of the metal) and a second one that must express the heat load the blade is suffering. The latter, presented in Eq. 2.3 is the so called "adiabatic effectiveness" η_{aw}.

$$\eta_{aw} = \frac{T_{0\infty} - T_{aw}}{T_{0\infty} - T_w} \tag{2.3}$$

From the definition above it is straight forward to understand that the achievable wall temperature is set by T_{aw} that, in turns, is mainly a function of the mixing process: the geometry of the ejection system, the thermodynamic conditions of the main-stream and of the coolant flow (density, viscosity and temperature) and the flow field parameters (velocity and turbulence level) are all playing a crucial role.

2.2.2 Film-cooling scaling parameters

Since film-cooling, as pointed out in the previous section, is extremely dependent upon the geometry and the aerodynamic and thermal fields, a proper selection of parameters is necessarily required to perform a meaningful comparison and parametrization. As suggested by Simon [12], coolant ejection typically lies in between two limit cases: a tangential film layer and a normal-wall injection, respectively Fig. 2.6 (a) and (b).

The first condition was characterized by the early study of Librizzi and Cresci [13] who produced an empirical correlation for the adiabatic wall effectiveness (Eq. 2.4): they found out that, in the case of a tangential film, η_{aw} could be expressed in function of the enthalpy ratio of the two flows participating to the mixing ($C_{p,\infty}/C_{p,c}$), multiplied by a sort of "mixing efficiency" ζ whose expression is reported in Eq. 2.5. The small exponent defines a weak dependency on the coolant Reynolds number and on the ratio of viscosities, while it is strongly affected by the main-stream to coolant mass-flow ratio ($x\rho_\infty u_\infty / s\rho_c u_c$).

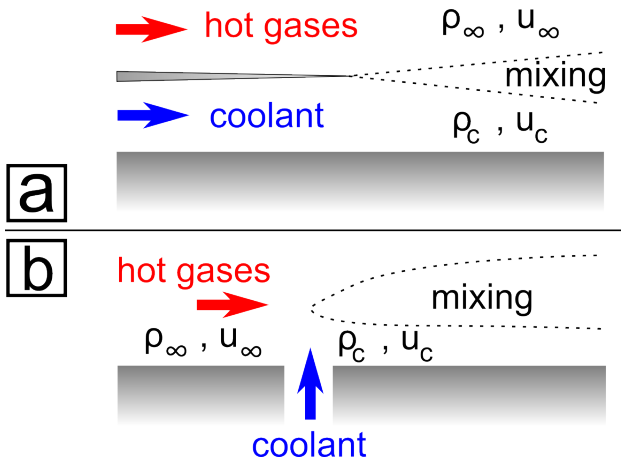

Figure 2.6: Tangential film injection (a) and normal wall injection (b)

$$\eta_{aw} = \frac{1}{1 + \frac{C_{p,\infty}}{C_{p,c}}(0.329(4.01 + \zeta)^{0.8} - 1)} \tag{2.4}$$

$$\zeta = \frac{x}{s}\frac{\rho_\infty u_\infty}{\rho_c u_c}\left(\frac{\mu_c}{\mu_\infty}\frac{\rho_c u_c s}{\mu_c}\right)^{-\frac{1}{4}} \tag{2.5}$$

In the field of film-cooling, the latter parameter is normally written in the form of Eq. 2.6 and goes under the name of "mass-flux ratio" (M) or "blowing ratio" (BR) (to better distinguish it from the mass-flow ratio (MFR), a global parameter computed as the ratio of the coolant mass-flow versus the main-stream one). It describes the effect on the mixing phenomenon due mainly to the component of the coolant momentum parallel to the wall and it is linked to the adiabatic efficiency by means of a proportional relation: the higher is the mass-flow of coolant injected over the surface, the better will necessarily be the protection.

$$BR = \frac{\rho_c u_c}{\rho_\infty u_\infty} \tag{2.6}$$

When the coolant is injected through a channel normal to the surface, as depicted in Fig. 2.6-b, two scenarios are possible: either the main-stream forces the coolant jet to turn towards the wall either the jet penetrates through the main-stream, completely detaching from the surface. Different authors investigated the phenomenon (Forth et. al. [25] and Fitt et al. [24]) and they all concluded that, up to the condition of separation, the best scaling parameter is the "momentum flux ratio" (I) as expressed by Eq. 2.7. Since it compares the momentum of the cooling jet with the one of the local main-stream, it measures the ability of the film to stay attached to the surface to be cooled, implying therefore that the adiabatic efficiency generally diminishes for high values of I.

$$I = \frac{\rho_c u_c^2}{\rho_\infty u_\infty^2} \tag{2.7}$$

The same momentum or mass flux ratios can be obtained for really different values of velocity and of the density ratios (DR). In engine-like conditions, the density ratio (DR) is typically equal to 2, which implies that the main-stream temperature should be twice the coolant one. Some studies have been performed with an engine-representative DR obtained by injecting a more dense gas (Osnaghi et al. [53]) but, normally, laboratory researches are performed at a lower DR. Given the large differences in magnitude, it is worth to summarize the effect that the density ratio has on the film-cooling performance.For the same value of I or BR, a lower DR implies necessarily a higher value of the velocity ratio. Since the latter quantity measures the intensity of the interactions taking place in the shear layer between coolant and free-stream, it is also an indication of the related turbulence production: at constant injection conditions, the mixing at low DR is enhanced with respect to the one at a higher value.
Several studies [57][8][73], focused on the effect of DR on the effectiveness when operating at constant blowing ratios. They demonstrated that η_{aw} for different DR was providing very similar results especially at very low BR which is explained by the fact that all the jets were attached to the surface. At higher injection rates, anyway, some difference could be appreciated which were mainly due the tendency of low DR jets to detach.

Cutbirth and Bogard [15] showed instead the potentiality of matching the momentum-flux ratio. They found in fact that, close to the holes (about 2 diameters downstream), no difference could be appreciated in terms of film effectiveness for different DR when injecting at the same I, also at different main-stream turbulence intensities. Differences as high as 20% were present, anyway, further downstream the hole and only for low Tu%.
When testing at a non-engine-representative DR, the momentum-flux ratio seems to perform better as a scaling parameter and therefore it makes sense to define a jet separation criterion based on I. Thole et al. [76] identified in fact three different flow conditions corresponding to just as many ranges of variation of the momentum-flux ratio: for $0.4 < I < 0.8$ the jet detaches at the exit of the hole to reattach farther downstream. Under the lower bound, a fully attached condition exists while for values higher than 0.8 a fully detached jet is present.

2.2.3 Main-stream and coolant interactions on blade surfaces

Because of the great variability of the conditions of the main-stream along the blade passage, film-cooling must be investigated with a local approach. Already at the inlet section, in fact, the flow field is normally far from being a homogeneous: the vane disk of the first high pressure stage has to deal, for example, with the radial temperature gradient introduced by the burner while, further downstream, the three-dimensional design of blades introduces pressure, velocities and enthalpy gradients along the blade height.
Inside the blade passage, the evolution of the pressure field imposes then a continuous variation of the local thermodynamic properties according to the evolution of velocity which, in turns, affects the status of the boundary layers, the location of possible shocks, the intensity of turbulence and therefore the level of mixing. This vast scatter of conditions forced the research to specialize over the years and to develop different film-cooling solutions for the different zones of the blade.

Leading edge cooling

The leading edge area is normally subjected to the highest heat load: the main-stream, by approaching the stagnation line perpendicularly, produces a flow-wall interaction which closely recalls the case of impingement characterized therefore by extremely high heat transfer coefficients. Moreover, since the blade tangential component of the main flow momentum is still weak in this zone, jets from cooling holes normally detach from the surface, already at small injection rates. These extreme conditions imply the adoption of a cooling system composed by several shortly spaced rows of staggered radial holes (named "showerhead" cooling), with the intent of creating a lower enthalpy layer as thick and as wide as possible over the surface. Several studies [14][3][61] demonstrated that in the leading edge area, the film-cooling effectiveness normally grows monotonously with the blowing ratio, in opposition to the behaviour found in other locations along the blade surface.

Curved walls cooling

Since suction and pressure sides are curved surfaces, stream line normal pressure gradients arise, which strongly affect ejection. If the coolant momentum keeps smaller than the main-stream one, the pressure gradient generated by a convex surface produces the beneficial effect of bending the jets over the wall. On concave surfaces, if the momentum of the cooling flow is too low, the adverse pressure gradient cannot be counter balanced, resulting in a detachment especially at low blowing ratios. As a consequence of these effects, the injection rate that maximizes the effectiveness on the suction (convex) side is normally smaller than the corresponding one for the pressure (concave) side (Ito et al. [40]).
Another main-stream characteristic that is of primary importance for the quality of protection on curved surfaces, is the turbulence intensity (Tu%) of the main-stream. A high Tu% level necessarily increases the mixing with the film, leading to a higher dispersion of coolant as well as to a higher en-

trainment of hot gases towards the wall. Consequently, η_{aw} will be lower than for a low Tu% case. Anyway, it has to be mentioned that several investigations (Schmidt and Bogard [67] [68]) demonstrated a beneficial effect of a high turbulence intensity for high momentum-separated jets: the high agitation of the stream enhances the dispersion of the jet, leading to the return of a portion of the coolant onto the surface.
Turbulence, moreover, has a drastic effect on the boundary layer developing around the blade since a high Tu% can cause an early laminar-to-turbulent transition. The latter phenomenon leads normally to a deterioration of the performance in the proximity of the hole while, further downstream, levels are practically unchanged (Drost et al. [20]).
Several authors (Kadotani and Goldstein [43], Liess et al. [46]) characterized then the effect of the boundary layer thickness on injection. They concluded that, when injecting in a thicker boundary layer, the region next to the hole generally shows a reduced effectiveness while the lateral coverage as well as the areas further downstream seem to be unaffected. It has to be remarked that injection itself normally thickens the boundary layer. If multiple cooling rows are present, then those placed further downstream on the blade surface eject therefore coolant in a thicker surface flow, which shows an enhanced ability to sustain higher injection rates.
In the tip region of rotor blades, curved surfaces cooling systems normally differ from those that can be found at mid height. This area, in fact, is characterized by much higher heat transfer coefficients, related mostly to the complex three-dimensional flow field generated by the interactions of the tip with the casing boundary layer. For this reason, protection is guaranteed by means of a combination of impingement and film-cooling geometries, placed in correspondence of the pressure side: the transport of cooling flow towards the suction side is committed to the strong tip vortex flow.

Endwall cooling

More recently, film-cooling technology has been massively applied also to blade endwalls, as a consequence of flatter temperature profile that modern burners are able to provide. The flow field in this area is dominated by secondary flows (Sieverding [71]) which necessarily interact and condition the coolant ejection from the surface. Early studies, such as the one of Blair [9], characterized the effect of an upstream slot ejection: results demonstrated that cooling flow injected upstream the separation lines of the horseshoe vortex is partially entrained by the latter and partially driven directly to the rear part of the suction side, without penetrating further in the blade channel. Successively Friedrichs et al. [26] investigated different cooling configurations having several cooling rows placed along the blade passage endwall. They reported a strong interaction between the wall cross-flow and cooling jets which drifted from the geometrical direction imposed by the holes geometry. In a later publication [27], Friedrisch documented instead the effect of the blowing ratio over secondary flows: he concluded that the endwall-induced loss component is generally small compared to the over all value. Moreover, he demonstrated that if injection is performed upstream the lift-off lines of the incoming boundary layer, secondary flows effects can be actually weakened. The author measured a reduction of the magnitude of loss cores as well as smaller span-wise extent. In the end, it has to be remarked that a great agreement exists in literature in defining the pressure side-endwall junction as the most difficult zone to protect, requiring therefore the positioning of discrete film-cooling holes as close as possible to the protruded blade body (Friedrisch et al. [28]).

2.3 Typical film-cooling geometries: brief overview

Up to this point, the present manuscript always omitted to precisely set any geometric characteristic of a typical "cooling system". This was done on purpose, since the geometry of the cooling devices is a crucial parameter for effectiveness and given the multitude of configurations in which film-cooling can be found. Generalizing, it can be stated that film-cooling

on blade surfaces is normally provided by a compound of holes. The latter are normally inclined with an angle smaller than 30 - 35 [°] with respect to the local surface curvature and organized in multiple staggered rows to enhance the coverage of the protected area. Typical values of the distance between rows are in the range from 5d up to 30d while the holes pitch can be taken equal to 3d, where "d" is the hole diameter.
It is clear that a small injection angle guarantees a stronger resistance to separation, also at high values of the momentum flux ratio, while shorter distances between holes rows and smaller pitches highly enhance the covered area. It has to mentioned, moreover, that holes often present a compound angle with respect to the local direction of the flow. This configuration is applied in those cases where the pressure field is strongly distorting the jet until the point of reducing the protected area (an example is the shower-head shape of the holes pattern in the leading edge zone), but also to reduce the component of the coolant momentum in the flow-wise direction and lowering therefore the separation risk.

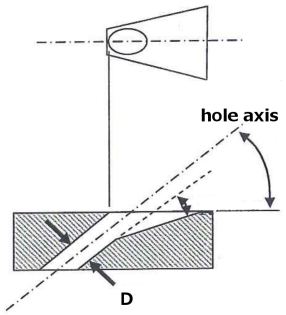

Figure 2.7: Typical geometry of a shaped film-cooling hole

In the end, even though only film-cooling from cylindrical holes is of interest for the present work, different hole's exit geometries are introduced for a sake of completeness. The reference study in this field was performed by Goldstein [30] that, for first, quantified the improvement on the effectiveness due to the shaping of the outlet section of holes. A shaped film-cooling

hole is presented in Fig. 2.7: the lateral expansion improves the coverage of the protection by widening the jet that, consequentially, is characterized by a lower momentum. Shaped holes demonstrated to be much less sensitive to separation than cylindrical holes and to be able to provide an enhanced effectiveness thanks to the higher momentum flux ratios at which they can be operated.

2.4 Loss mechanism in film-cooling

From the previous section it is clear that film-cooling implies an aerodynamic and an enthalpy loss. The mixing process produces an irreversible conversion of main-stream momentum to entropy while the temperature difference between the main-stream and the coolant generates a heat flux that degrades the enthalpy of the hot main-stream to the level of the colder film flow. Denton, in his famous publication on the loss mechanism in turbomachines [18], defined each loss component by means of the energy balance reported in Eq. 2.8:

$$\begin{aligned} W &= W_s - Q - S = \\ &= W_s - \int (T - T_{0g}) dQ - \; T_{0g}\, c_p\, (\gamma - 1) M^2 (1 - \frac{V_c}{V_g}\, cos\alpha)\, \dot{m}_c \end{aligned} \tag{2.8}$$

The heat subtracted from the main-stream is represented by "Q": it sums every heat loss of every cooled component along the expansion line of the working flow and it depends on T, the temperature at which the heat is exchanged (i.e. T_{aw}). The last term "S" defines instead the increase in entropy production due to the mixing process. This formulation, taken from Shapiro, strongly depends on the angle of injection (for $\alpha = \pi/2$ the effect of the velocity ratio nulls) while the temperatures of the two media do not play a role. It is interesting to mention that a high coolant velocity could be actually beneficial as it could energize the main-stream.

In practice, a much more useful parameter to assess the performance of a stage is the kinetic energy loss coefficient ζ (Eq. 2.9) which compares the actual exit kinetic energy with the ideal energy budget of the flow (i.e. the isentropic velocity V_{2s}). This formulation is anyway not taking into account the different energy levels of the coolant and of the main-stream, that is why several authors (Osnaghi et al. [53], Ligrani [47], Drost [21]) suggested to compute the losses of a cooled turbine stage by means of a thermodynamic loss coefficient ζ_{th}. The latter is reported in Eq. 2.10 and is comparing the power of the exit flow (assuming it to be fully *"mixed out"*) with respect to the ideally available power: the sum of the isentropic specific energy of the main-stream and coolant respectively. In the following, the efficiency of a cooled cascade will be always evaluated by means of Eq. 2.10 and, when possible, a comparison with the primary loss coefficient (Eq. 2.9) will be also given.

$$\zeta = 1 - \frac{V_2^2}{V_{2s}^2} = 1 - \frac{1 - \left(\frac{\widehat{P_2}}{P_{02}}\right)^{\frac{\gamma-1}{\gamma}}}{1 - \left(\frac{\widehat{P_2}}{P_{01}}\right)^{\frac{\gamma-1}{\gamma}}} \tag{2.9}$$

$$\zeta_{th} = 1 - \frac{\left(1 + \frac{\dot{m}_c}{\dot{m}_g}\right) h_{02mix} \left[1 - \left(\frac{P_2}{P_{02}}\right)^{\left(\frac{\gamma-1}{\gamma}\right)_{mix}}\right]}{h_{01}\left[1 - \left(\frac{P_2}{P_{01}}\right)^{\left(\frac{\gamma-1}{\gamma}\right)_g}\right] + \frac{\dot{m}_c}{\dot{m}_g} h_{0c}\left[1 - \left(\frac{P_2}{P_{0c}}\right)^{\left(\frac{\gamma-1}{\gamma}\right)_c}\right]} =$$

$$= 1 - \frac{\left[1 - \left(\frac{P_2}{P_{02}}\right)^{(\frac{\gamma-1}{\gamma})_{mix}}\right] [\dot{m}_g T_{01} + \dot{m}_c T_{0c}]}{\dot{m}_g T_{01}\left[1 - \left(\frac{P_2}{P_{01}}\right)^{(\frac{\gamma-1}{\gamma})_g}\right] + \dot{m}_c T_{0c}\left[1 - \left(\frac{P_2}{P_{0c}}\right)^{(\frac{\gamma-1}{\gamma})_c}\right]} \tag{2.10}$$

Chapter 3

Experimental methodology

3.1 Pneumatic pressure probe for downstream wakes measurement

Pressure probes are the most common and widely used tools for the characterization of flow-fields. They normally consist of a stem which carries a thinner measuring head. The latter can be aligned with the stem or L-shaped (see Fig. 3.1), to separate the measuring point from the stem and reduce therefore its influence. Depending on the application, probes can be pneumatic (the transducer is connected by means of tubing to the measuring point) or fast-response, with a miniaturized transducer mounted directly in the measuring head. Historically, pneumatic probes have been developed to measure the total and static pressure of a flow field. Successively, by equipping the measuring head with multiple holes, also the flow angle could be retrieved by applying a proper calibration procedure (Sec. 3.1.1).

In the frame of the present work, two different types of pneumatic pressure probes have been used, a 3-hole and a 5-hole probe. Both have been applied for the characterization of the total pressure loss in the downstream section of the cascade as well as to measure the downstream flow angle dis-

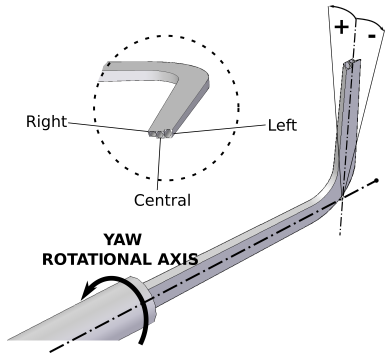

Figure 3.1: Used conventions for 3-hole probe angle measurements

tribution. In the present chapter, for the sake of simplicity, the topic will be addressed only with respect to a typical 3-hole probe even though the validity of the taken assumptions and of the derived conclusions, holds in principle also for 5-hole pneumatic probes.

3.1.1 Total pressure and angle measurements: angular calibration

The angular calibration of a multi-hole probe was performed in a proper facility which allows to rotate the probe inside the core of a controlled jet. The probe was calibrated between Ma=0.5 and Ma=0.9 with a yaw-angle ranging between ±30 [°]. Fig. 3.1 reports the conventions adopted in the frame of reference of the probe. Data have been then converted in terms of dimensionless coefficients in order to loose the dependency on the absolute value of the pressure measurements: in Fig. 3.2, the resulting calibration maps for C_{Pt} and C_{yaw} are reported while their expressions are presented in equations 3.1, 3.2 and 3.3.

$$C_{Pt} = \frac{P_{central} - P_{ref}}{P_{ref} - P_{av}} \tag{3.1}$$

$$C_{yaw} = \frac{P_{left} - P_{right}}{P_{central} - P_{av}} \tag{3.2}$$

$$P_{av} = \frac{P_{left} + P_{right}}{2} \tag{3.3}$$

P_{ref} is the reference pressure that, during experiments, coincided with the total pressure P_{02} in the downstream section of the cascade. Fig. 3.1 reports the conventions adopted in the frame of reference of the probe as well as those for $P_{central}$, P_{left} and P_{right}. During measurements, C_{pt} and C_{yaw} were computed on the acquired data and by means of an iterative procedure, local total pressure P_{02} and flow angle β_2 were retrieved from the calibration maps. The probe was traversed in the pitch-wise direction downstream of a cascade. In correspondence of the traversing plane, the test section (see Sec. 5.3.3) was also equipped with a rack of static pressure taps. By assuming that no pressure gradient is taking place in the span-wise direction, the local static pressure P_2 was taken to be equal to the one measured by the wall pressure taps. In order to provide a value of the static pressure for each position of the probe during the traversing, a linear interpolation of P_2 values within every pair of pressure taps was implemented.

3.1.2 Angular calibration for a 5-hole probe

As the name suggests, a 5-hole probe is equipped with two more holes, namely the up and down holes. The latter constitute a new measurement plane (perpendicular to the yaw plane defined by the left and the right hole) that actually allows to resolve one more angle, the so called "pitch angle" of the flow. Based on the conclusions previously taken for a 3-hole probe, it is clear that in this case, the calibration procedure implies one more rotation: for each yaw angle, the full range of pitch angles is swept. The computation of the pitch angle introduces moreover a new unknown, increasing the number of coefficients to be computed from two to three: C_{pt}, C_{yaw} and C_{pitch} (Eq. 3.4).

$$C_{pitch} = \frac{P_{up} - P_{down}}{P_{central} - P_{av}} \tag{3.4}$$

$$with \quad P_{av} = \frac{P_{left} + P_{right} + P_{up} + P_{down}}{4}$$

In the case of a 5-hole probe, since a more complex system of equations is solved, it makes sense to introduce one more coefficient, which carries the information about the local static pressure: C_{ps} (Eq. 3.5). By means of a fourth coefficient, the local static pressure at the measuring point can also be retrieved, and this allows to relax the assumption of "zero transversal pressure gradient" that has to be taken in the case of a simpler probe.

$$C_{ps} = \frac{P_s - P_{av}}{P_{central} - P_{av}} \tag{3.5}$$

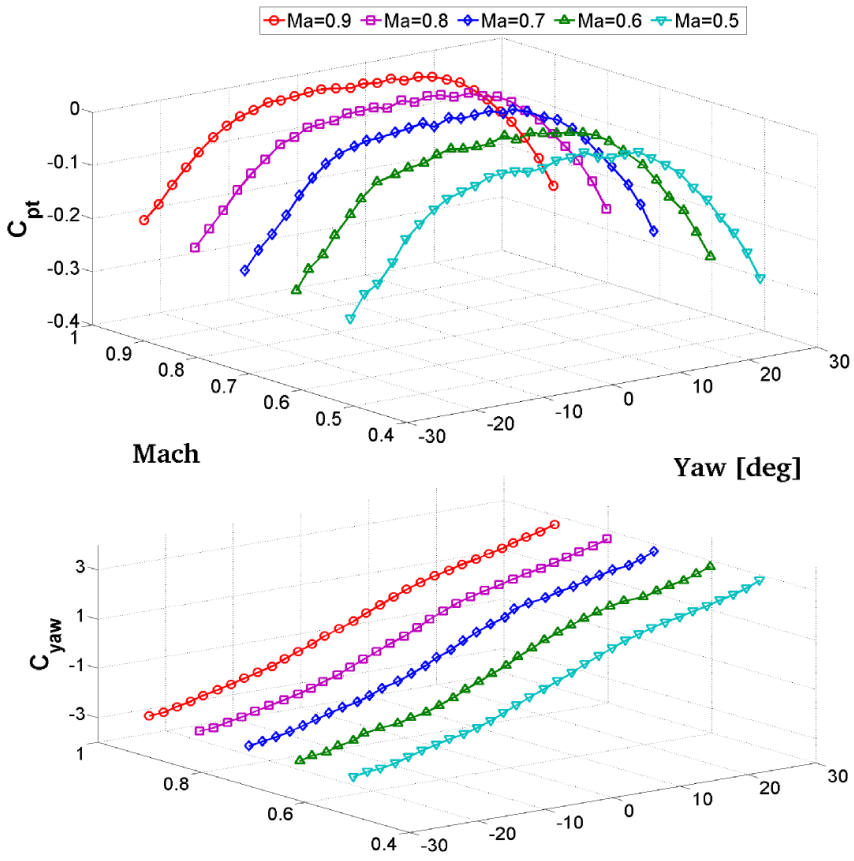

Figure 3.2: C_{Pt} and C_{yaw} calibration maps

3.1.3 Dynamic behaviour of the probe: dynamic calibration

The need for a compensation: the simple organ pipe resonance theory

Figure 3.3 presents the most simplified configuration of a pneumatic pressure system, where the pressure tap "A" is connected by a pipe of length "L" to the pressure transducer "B", placed on the other side of the tubing.

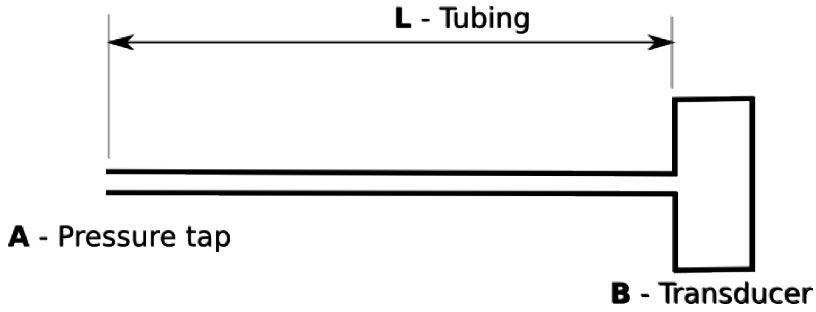

Figure 3.3: Pneumatic line scheme

By neglecting the effect of viscosity and heat conductivity, this pneumatic system can be easily modelled by means of the *simple organ pipe resonance theory*, if one takes also the assumption (not far from reality indeed) that in the tubing the flow velocity is smaller than the one of sound. Under these hypothesis, the most simplified and idealistic ones, if a periodic variation of the pressure is applied in correspondence of "A", the *simple organ pipe resonance theory* predicts the system to respond with a great magnification in correspondence of the resonant frequencies while the phase distribution jumps instantaneously of π [rad] every time a resonant peak is present (Fig. 3.4).

This purely theoretical result, derived from a too crude approximation of the problem, allows anyway to draw an important conclusion: except for the very first frequencies, all the other spectral components of a pressure signal acting in "A" will be distorted by the piping system, at least in terms of phase, making therefore the transducer "B" to measure a different signal

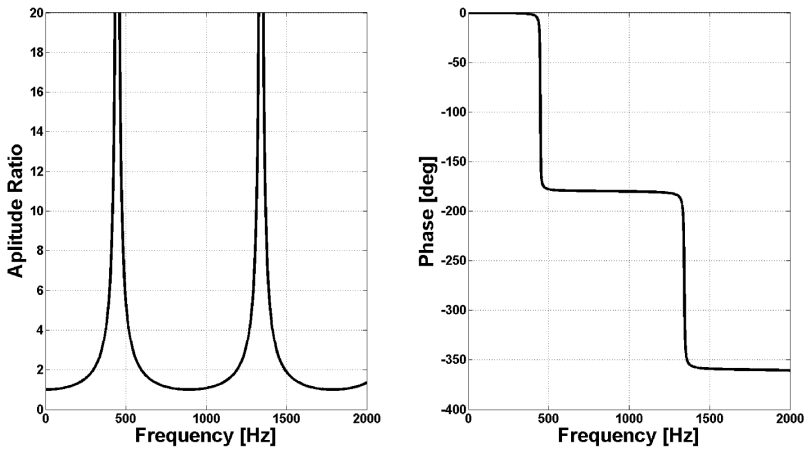

Figure 3.4: Simple organ pipe theory prediction

with respect to the input.

Compensation of a signal: the system transfer function

With the name *transfer function*, one refers to the relation linking the input and the output of a system. It can be evaluated in both, the time and the frequency domain by exploiting the property of convolution of spectra and, in the latter case, it can be directly computed by performing a ratio between the spectral content of the system output with respect to the input one.

$$TF(f) = \frac{OUT(f)}{IN(f)} \tag{3.6}$$

In this form, it is clearly a complex function that takes into account the information in terms of both, amplification factor and delay between input and output. In fact, by expanding the terms and expressing them in polar coordinates, it is clarified that its modulus equals the ratio of the two modulus while the phase coincides with the difference between the two phases at each frequency component.

$$TF(f) = \frac{|OUT(f)|e^{-i\phi_{OUT(f)}}}{|IN(f)|e^{-i\phi_{IN(f)}}} = \\ = \frac{|OUT(f)|}{|IN(f)|}e^{-i(\phi_{OUT(f)}-\phi_{IN(f)})} = |TF(f)|e^{-1\phi_{TF(f)}} \tag{3.7}$$

This formulation is particularly helpful to understand the mechanism of compensation: let us suppose that the transfer function $\overline{TF(f)}$ of a pneumatic system is known a priori and let us consider a set of data *d(t)* measured by means of the same (IDENTICAL) pneumatic system. Because of what was previously stated, we know that *d(t)* is not representing the real phenomenon we were aiming to measure, but it is contaminated by distortions introduced by the system itself. If one accepts the assumption that the known transfer function $\overline{TF(f)}$ is representative of the most general behaviour of the system, then it can be used to correct *d(t)* in order to retrieve the true excitation signal:

$$D_{comp}(f) = \frac{D(f)}{\overline{TF}} \longrightarrow d_{comp}(t) = IFT\{D_{comp}(f)\} \tag{3.8}$$

The latter concept is the most critical step of the whole procedure: the quality of the compensation strongly depends on the quality of the computed transfer function. If, for any reason, TF does not represent the real, complete and most generic behaviour of the system, the compensated signal will not correspond to the real input to the system.

Evaluation of the system transfer function: the dynamic calibration

Several methods have been developed to compute the transfer function of a piping line. Bergh and Tijdeman [34] computed it analytically, by coupling the Navier-Stokes equations with the equations of state, energy and continuity but, successively, Ommen et al. [41] demonstrated that this approach

tends to over estimate the magnitude of the modulus ratio.
Paniagua and Dénos [55] retrieved the transfer function of a pneumatic probe by means of a time-domain fitting on experimental data. The methodology implies the simultaneous acquisition of the response of the probe and of a fast response reference transducer: by imposing an order for the pneumatic system, the fitting coefficients of the probe signal are computed in the time domain which are then correlated with a transformation matrix to the ones of the fitted reference signal. The main assumption behind this procedure is that the reference transducer and the pneumatic probe are systems of the same order, a condition that generally can not be verified.
Irwin et al. [39] computed the TF experimentally in the frequency domain. They used a white-noise signal to excite at the same time a reference probe and a pneumatic one. The recorded time series were then transformed in the frequency domain and the transfer function computed exactly as described in Sec. 3.1.3. Given the solid theoretical background on which the latter method is based, it was selected to be applied to the present usage.
6 Retrieving experimentally a transfer function, nominally corresponds to a dynamic calibration procedure and it is therefore of crucial importance to select the correct and most generic input to obtain a robust and reliable result. Even though different excitation signals could be selected for this purpose, in the present application a pressure step was used: an ideal step function is able in fact to excite at the same time all the frequencies up to $+\infty$, providing a fast calibration process. On the contrary, the main draw back is the fact that all the frequencies are excited with an equal amount of energy, producing a particularly noisy spectrum.
In the frame of the present work, the pressure step was produced by means of the setup shown in Fig. 3.5. The groove placed on the lateral surface of the cylindrical support allowed to block the neck of a balloon in such a way that a 3-hole probe and a fast reference transducer could be completely enclosed inside the internal volume of the balloon. The latter was then pressurized at 100 [mbar] above the atmospheric pressure and burst. Assuming the signal measured by the fast reference transducer to be representative of the true not-damped-not-delayed pressure input, the transfer function of each hole of the probe could then be computed by means of

the procedure outlined in the previous paragraph. The latter calibration methodology, the so called *"balloon test"*, was developed by Paniagua et al. [55] in the frame of the previously cited time-fitting dynamic calibration.

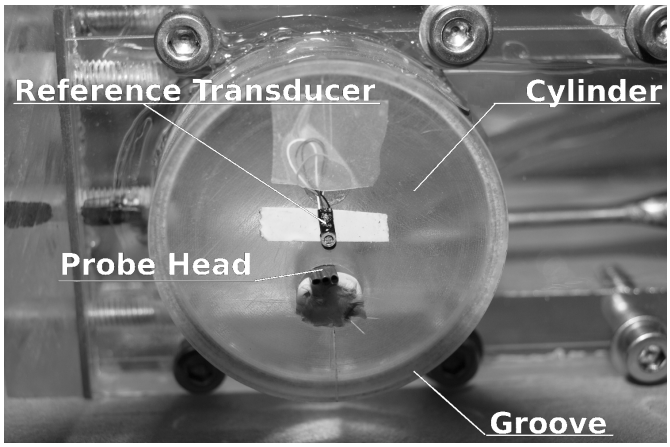

Figure 3.5: Support for the dynamic calibration (balloon test)

The so computed transfer function is reported in Fig. 3.6 for the central hole of the pressure probe. It describes a typical damped second order behaviour: the magnitude remains equal to 1 up to about 20 [Hz]; then it starts to decrease and, at 300 [Hz], the amplitude of the signal recorded by the probe is only the 10% of the reference one. The phase plot keeps equal to 0 up to 20 [Hz] and then drastically decreases, supporting the conclusion that the system probe-transducers belongs to the second order group. The interested reader can refer to Appendix B for a detailed description of the applied data processing procedure.

3.1.4 Shock correction

Any time the head of the probe is facing a supersonic flow-field, a detached bow-shock is created in front of the probe nose, at a distance proportional to the local Mach number of the flow. As such, the pressure input acting

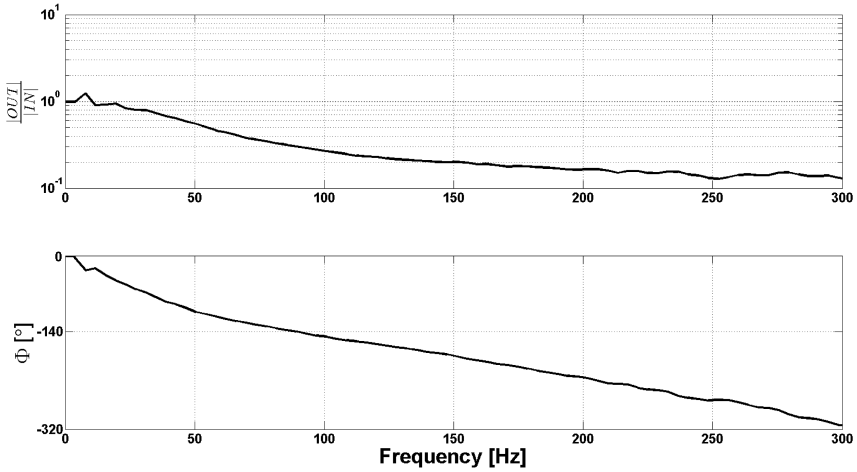

Figure 3.6: Computed transfer function for the central hole of the probe

on the head is describing a subsonic flow field rather than a supersonic one, leading therefore to corrupted measurements.
By taking the assumption that the shock is normal to the entrance of the measuring holes, a correction can be applied to retrieve the real total pressure. As shown in equations 3.9 and 3.10, by knowing the static pressure upstream of the shock P_{up}, the true total pressure P_{0up} can be computed from the total pressure P_{0down}, measured downstream of the shock. The solution is obtained by iterating on the upstream Mach number Ma_{up}.

$$P_{0up} = \frac{P_{0down}}{\left[\frac{(\gamma+1)Ma_{up}^2}{(\gamma-1)Ma_{up}^2+2}\right]^{\frac{\gamma}{\gamma-1}} \left[\frac{(\gamma+1)Ma_{up}^2}{2\gamma Ma_{up}^2-\gamma+1}\right]^{\frac{1}{\gamma-1}}} \tag{3.9}$$

$$Ma_{up} = \left\{ \left[\frac{2}{\gamma-1} \left(\frac{P_{0up}}{P_{up}} \right)^{\frac{\gamma-1}{\gamma}} - 1 \right] \right\}^{0.5} \tag{3.10}$$

3.2 Thermochromic liquid crystals

3.2.1 Liquid crystals: a state of matter

Liquid crystals are complex organic substances that normally organize in an intermediate state of matter between the liquid and the solid phase. They possess in fact a certain molecular order that, anyway, is less than the one of a crystalline solid and more than the one of an isotropic fluid. These peculiarities guarantee the mechanical properties of liquids (fluidity) but the optical ones of crystals (anisotropy to light).
In the "family" of liquid crystals, the class that shows useful characteristics to heat transfer measurements goes under the name of *thermotropic* type. They are thermal activated mesophases that can be further subdivided into three classes, depending on the molecular arrangement: smectic, nematic and cholesteric/chiral-nematic. The latter group, in particular, tends to organize in distinct layers, each one of them presenting a well defined direction for the molecular alignment (see. Fig.3.7-a). By crossing the layers perpendicularly, one recognizes that they are organized in a continuous twisted structure (Fig. 3.7-b). The helix arrangement is the responsible for the different optical properties of the thermotropic liquid crystals such as *birefringence*, *optical activity*, *circular dichronism* and *selective reflection*, each of them being a function of composition and temperature. When a chiral-nematic compound is hit by white light, it selectively reflects one particular wavelength (the other ones are transmitted) according to its temperature and it is because of this characteristic that they are commonly named "thermochromic liquid crystals" (TLCs) (Abdullah et al. [2]).
Depending on the compound, the reflected wavelengths fall in the visible spectrum of light for a certain range of temperatures. The mixtures that present a temperature bandwidth from 0.5 to 4 [°] are named "narrowband" TLCs while the "broadband" liquid crystals normally exhibit a colour-play from 5 to 30 [°]. The temperature range, according to the Hallcrest standard (Parsley [48]), is defined as the difference between the blue-start temperature (higher temperature or clearing point) and the red-start point (lower temperature or activation temperature). Pure TLCs are highly suscepti-

ble to ultraviolet radiation, dust and solvents which cause an alteration of the colour-play. In order to enhance their chemical stability, nowadays commercially available TLCs are enclosed in spherical polymer capsules of 10-15 [μm] in diameter. TLCs are normally sold as adhesive sheets or in the form of a sprayable coating that allows for an easier deposition on complex surfaces, as in the present application.
The response time of a TLCs mixture is defined as the time needed to reach a new molecular configuration as a consequence of a small temperature variation. Ireland et al. [62] tested a typical chiral-nematic-microencapsulated compound, deposed on a surface as a 10 [μm] layer and measured a time constant of 3 [ms], while Sillekens [72] and Wagner [77] computed a time response of 100 and 150 [ms] respectively. The obvious conclusion is that the dynamic performance of a certain compound is a strong function of its composition and that it cannot be stated a priori to its deposition. In any case, the upper limit will be always in the order of magnitude of some hundreds Hertz.

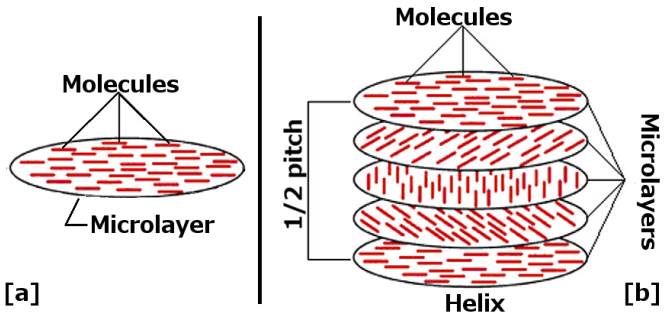

Figure 3.7: (a) Ordered molecules in a chiral-nematic liquid crystal microlayer; (b) Helical arrangement of microlayers of chiral-nematic compounds - taken from [2]

3.2.2 The HSI system and the need for an in-situ calibration

As we have seen in the previous section, the colour assumed by a certain TLCs compound is directly linked to its temperature. In order to provide a unique definition of the colour-temperature relation, a standard codification of colours must be taken.
The discipline that aims to measure colours is called colorimetry and it was firstly standardized in 1931 by the *Commission Internationale de l'Eclairage* [79]. According to the CEI standard, colours are described by means of a three components additive model (the CIE XYZ standard) that defines them in terms of a linear combination of three artificially defined primaries and that do not correspond to any physical characteristic of light (i.e. wavelengths): X, Y and Z. Several three-components models have been developed on the basis of the CIE XYZ standard in order, for example, to mimic the human eye perception of colours (the RBG model) but, in the field of TLCs thermometry the Hue-Saturation-Intensity (HSI) colour space is commonly used.

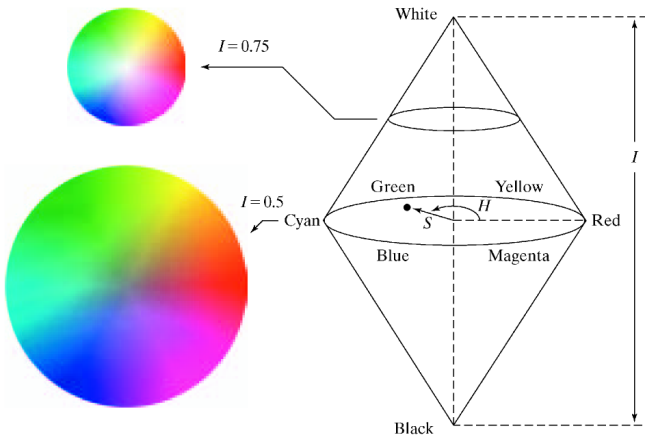

Figure 3.8: Hue-saturation-intensity colour space [54]

In the HSI model (Fig. 3.8), hue (H) represents the *shade* of a colour (red, blue, yellow, green, etc.), saturation describes the dilution of a colour

with white while intensity defines instead its relative brightness. As shown by Abdullah et al. [2], the three parameters are all computed from the RGB spaces and, in particular hue is defined as an angle ranging from 0 to 360 [°], with 0 coinciding with red. It is clear that, in this codification, hue is ideally independent on the illumination intensity, making of it the first choice parameter to be linked to temperature: in the frame of the present work, a typical temperature-hue relation will be in fact applied.
In reality, it must be highlighted that H is independent on the intensity of the illumination source only if the spectrum of light is fixed, a condition extremely difficult to obtain since illumination sources normally vary the spectrum with ageing and since the latter is also a function of the surface characteristics. Moreover, it has been demonstrated [16] that H is also device dependent as the interpretation of the RGB colour space is a property of the tool that records the image. In the end, it has to be mentioned that the light reflected by a surface depends of the incoming light incidence angle while the light that reaches the imaging sensor is a function of the angle at which the optic is placed with respect to the scattering object (view angle). In other words, the RGB values of the recorded image are strongly conditioned by the geometric arrangement.
The latter considerations lead to the conclusion that, since hue values are so strongly related to the setup, the same configuration must be kept in both calibration and measurement phase. In TLCs thermometry, if the test section is easily accessible, calibrations are normally performed in-situ, by means of a calibration target aligned accordingly to the final angle of view of the camera and with the light sources fixed in their final positions. When an in-situ calibration cannot be performed, then the calibration is performed outside of the test section (ex-situ) but providing to respect exactly the same alignments and conditions (i.e. light source) of the measurement configuration.

3.2.3 Calibration procedure

In the frame of the present work, the hue-temperature relation (nominally a calibration of the TLCs compound) was always obtained by means of an *ad hoc* calibration surface also used for in-situ measurements. It consisted of an aluminium plate equipped, on one extremity, with an electrical resistance while, on the opposite side, cold water was made flowing through a hole drilled directly in the plate. The temperature gradient generated between the heat source (the resistance) and the heat sink (the flowing water), was registered by means of a rack of thermocouples (TC) glued less than one millimeter underneath the surface (Fig. 3.9). A thin layer of black backing paint was deposed on the surface prior to TLCs, to enhance the intensity of the colour play.
Once the temperature gradient was stabilized, the TC temperatures have been acquired simultaneously to the image of the surface. The latter was then transformed from RGB to HSI colour space and a temperature was assigned to each pixel by linearly interpolating between thermocouples. As mentioned previously, the link between R, G and B components and H is strongly non linear even though a monotonically calibration curve is normally obtained, as shown in Fig. 3.10.

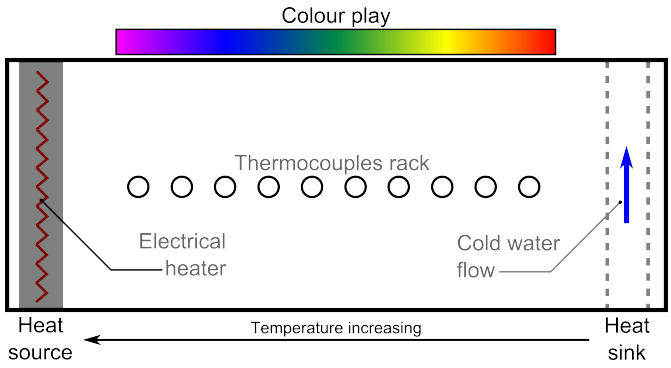

Figure 3.9: Sketch of the TLCs calibration setup typically used in the frame of the present project

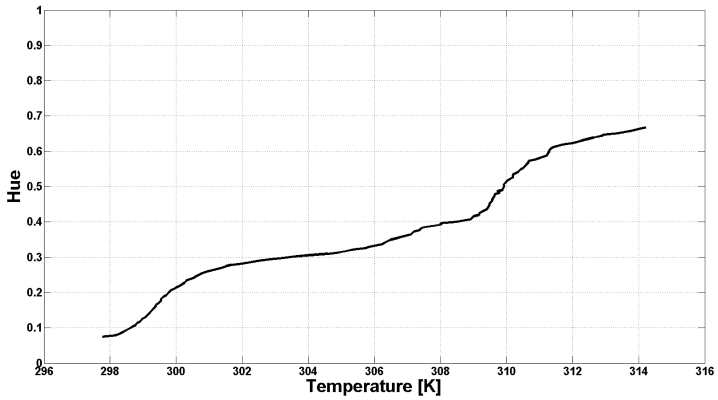

Figure 3.10: Typical hue-temperature calibration curve: measured data versus cubic spline fitting

3.3 Thin-Films Thermometry for Heat Transfer Measurements

Thin-films thermometry is a well known technique for time dependent surface temperature measurements. The probe consists of a sensing element made of a resistive material that is a leg of a constant current (CC) Whetstone bridge (figure in tab. 3.1). When the sensing element changes its own temperature, then according to Eq. 3.11 it also changes its resistance. The latter variation unbalances the CC Wheatstone bridge that produces in turns an output voltage proportional to the variation in temperature (equation in tab. 3.1).

$$R = R_{ref} \left[1 + \alpha \left(T - T_{ref}\right)\right] \tag{3.11}$$

A thin-film sensor is therefore a thermometer that, thanks to the CC circuitry but also as a result of the small dimensions to which these devices normally can be built (about 0.5 [μm]), is definitely providing a better frequency response than a standard thermocouple. It is by exploiting this last characteristic that thin-films can be used in a transient measurement

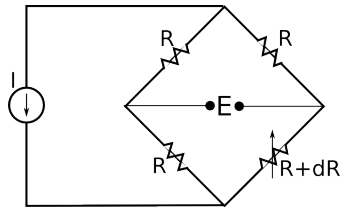

$$E \propto \frac{I*R}{4}\left[\frac{dR}{R+dR/4}\right]$$

Table 3.1: Constant current Wheatstone bridge and the proportionality relation between the voltage E and the variation of resistance

technique to retrieve the convective heat transfer rate on a surface.

3.3.1 Transient measurement technique: the semi-infinite substrate assumption

Let us consider a body in isothermal conditions that suddenly, at time t_0, is invested by a stream at a temperature T different from the body's initial one. The external surface will be then submitted to the convective action of the flow and the temperature of the body will definitely start drifting from the initial one. When in fact heat flux is established at the surface, conduction necessarily takes place inside the solid to receive/release energy from/towards the convective medium. In other words, from the most general point of view, by quantifying the heat transmitted inside the solid by conduction, the convective heat transfer rate at the surface can be also retrieved.

If no lateral effects are taking place, the evolution in time of the temperature profile in a solid can be computed by solving the one dimensional unsteady heat conduction equation (Eq. 3.12) without heat generation. The solution of such a differential problem necessarily requires an initial condition ($T(x, t = 0) = T_{initial}$) and two spatial boundary conditions that have to be taken according to the typology of the phenomenon.

$$\frac{\partial^2 T}{\partial x^2} = \frac{1}{\alpha}\frac{\partial T}{\partial t} \tag{3.12}$$

The first boundary condition can be imposed by considering that, in the present case, the outer surface is submitted to convection. Only in that very point the energy transmitted by convection corresponds to the one exchanged by conduction. According to the frame of reference set by Fig. 3.11, this coincides with imposing that the Fourier's law at the surface equals the convective heat transfer rate $\dot{q}_w$ (Eq. 3.13).

$$-k\frac{\partial T}{\partial x}\bigg|_{x=0} = \dot{q}_w \tag{3.13}$$

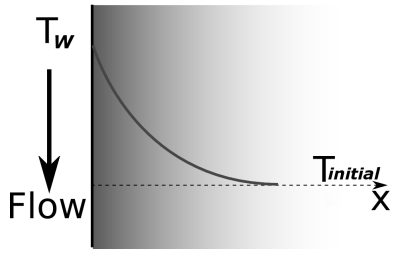

Figure 3.11: Frame of reference for the heat conduction problem with convection boundary condition

The second spatial boundary condition must be imposed instead at a distance L from the outer surface as a typical Dirichlet condition: the temperature variation in time must be measured in correspondence of L ($T(L,t)$). One way to overcome the difficulties that the homogeneous condition necessarily introduces (application of a temperature probe in the substrate exactly along the heat conduction direction), is to make sure that the inner temperature of the substrate is not drifting from the initial one as heat is only provided to the outer region. This assumption, that can be considered valid only in some circumstances (see Sec. 3.3.2), naturally treats the substrate as a semi-infinite solid and actually guarantees the existence of an analytical solution to the problem.

$$\dot{q}_w = \sqrt{\frac{\rho c k}{\pi}} \left[\frac{T_w(t)}{\sqrt{t}} + \int_0^t \frac{T_w(t) + T_w(\tau)}{(t-\tau)^{1.5}} dt \right] \tag{3.14}$$

Equation 3.14 reports the analytical solution of the semi-infinite problem in the form developed by Schultz and Jones [69] that directly computes the convective heat transfer rate $\dot{q}_w$. It is a function of the substrate characteristics (ρ being the density, c the specific heat and k the thermal conductivity of the material) and of the surface temperature evolution in time $T_w(t)$ that is actually what a thin-film is able to measure.

3.3.2 Penetration depth

In order to correctly solve Eq. 3.14, the semi-infinite assumption must be respected during the tests. The parameter that is quantifying the degree of accordance between the reality of experiments and the latter modelization is the penetration depth d_{heat} (Eq. 3.15). It measures in fact the thickness of the energy flow propagating inside the material and it is a function of the thermal diffusivity of the material α and of the duration t^* of the heat transfer phenomenon.

$$d_{heat} = 4\sqrt{\alpha t^*} \quad \alpha = \frac{K}{\rho C} \tag{3.15}$$

The semi-infinite assumption is respected if d_{heat} keeps small if compared to the thickness of the model on whose surface convective heat transfer is applied. This is guaranteed by applying heat for a short time (small t^*) and if the substrate is weakly diffusive. α is in fact an indication of the thermal inertia of a material and the lower it is, the smaller is also the tendency of the volume to vary its internal temperature.
In the present study, a blade was machined out of Macor ® (machinable glass-ceramic), a really low conductive material whose characteristics are reported in table 3.2 as provided by the supplier. On the surface of the blade, a thin ($\simeq 0.5[\mu m]$) platinum layer was painted at 42 positions along both the suction and the pressure side, at the mid height of the blade and for a span-wise length of 20 [mm] (Fig. 3.12). Each layer corresponds to

the sensing element of a thin-film gauge that is connected to the rest of the circuitry (constant current bridge) by means of golden contacts and low resistance wires (also shown in fig. 3.12).

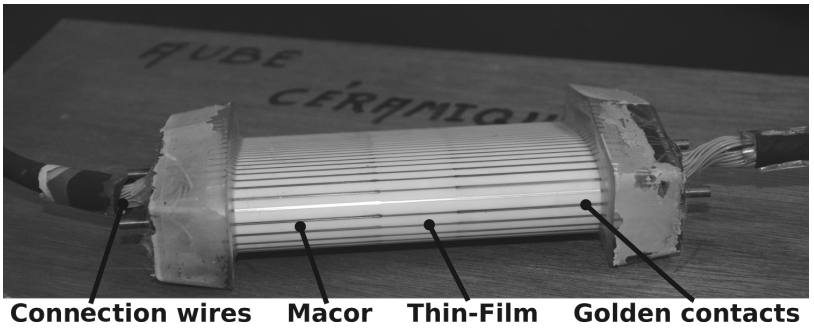

Figure 3.12: Thin-films instrumented blade

Macor			
Description	**Symbol**	**Unit**	**Value**
Density	ρ	Kg/m^3	2520
Specific heat	c	J/KgK	752
Thermal conductivity	K	W/mK	1.672
Thermal diffusivity	α	m^2/s	$8.8 * 10^{-7}$

Table 3.2: Properties of Macor ®

3.3.3 Computation of the convective heat transfer coefficient h

The methodology presented in the following was developed for a short duration facility, described in details in Sec. 5.2. In such a setup, a hot stream air is impulsively flowing over the blade surface by a fast opening valve (shutter) and for a total time of about 0.5 [s]. When the shutter

opens, the main-stream is subjected to a step temperature variation. $\dot{q}_w$ can be then computed by means of equation 3.14 which produces, anyway, a negative slope linear dependency (Fig. 3.13), as the difference $T_{ref} - T_w$ tends asymptomatically to zero. Making an average of the computed heat transfer rate is absolutely meaningless.

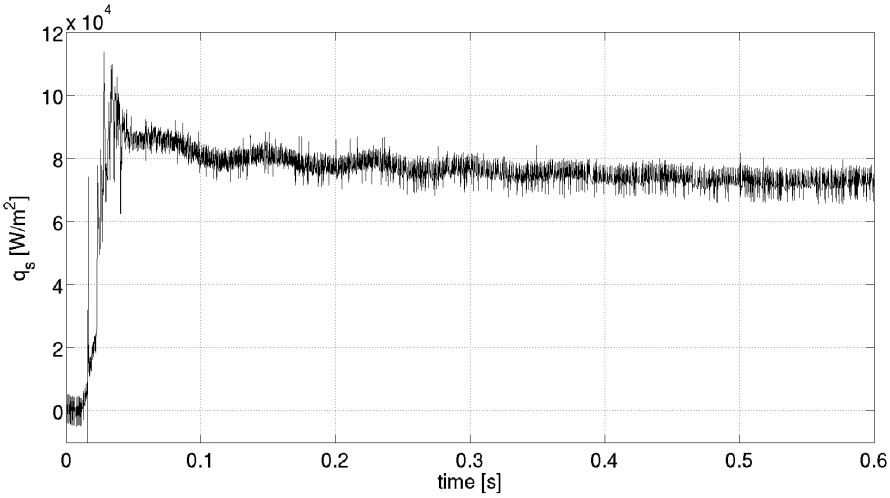

Figure 3.13: Evolution of the heat transfer rate with time

Given this constraint, the value of $\dot{q}_w$ that makes the most sense to consider is the first point after the shutter opens, since the semi-infinite assumption is directly respected as no conduction is taking place yet. Anyway, because of the finite time response of the measuring devices, the heat transfer rate increase cannot absolutely be consider a step function and taking the first point of the time series will inevitably lead to wrong evaluations.

To avoid any source of erroneous results, in the present work $\dot{q}_w$ is evaluated with respect to the relative increase in wall temperature (grey line in Fig. 3.14-a). A 0.15 [s] long sub-record of the heat transfer rate evolution is then extracted (red line in Fig. 3.14-b), starting from 0.05 [s] after the shutter opens, guaranteeing therefore the main-stream to be fully established as well as the semi-infinite condition to be respected everywhere. A linear regression is then performed on the extracted record and the heat transfer rate for a surface temperature equal to the initial one (at the shutter opening, Fig. 3.14-a) is extrapolated. Finally, the convective heat transfer coefficient h is retrieved using $h = \dot{q}_w/(T_{ref} - T_{w-initial})$.
It has to be remarked that, up to this point, T_{ref} was left undefined. This was done intentionally, as it is not fundamental for the description of the method and since it will be given a deeper attention later in the text, when heat transfer measurements in short duration facilities will be presented and discussed (Sec. 5.6.3).

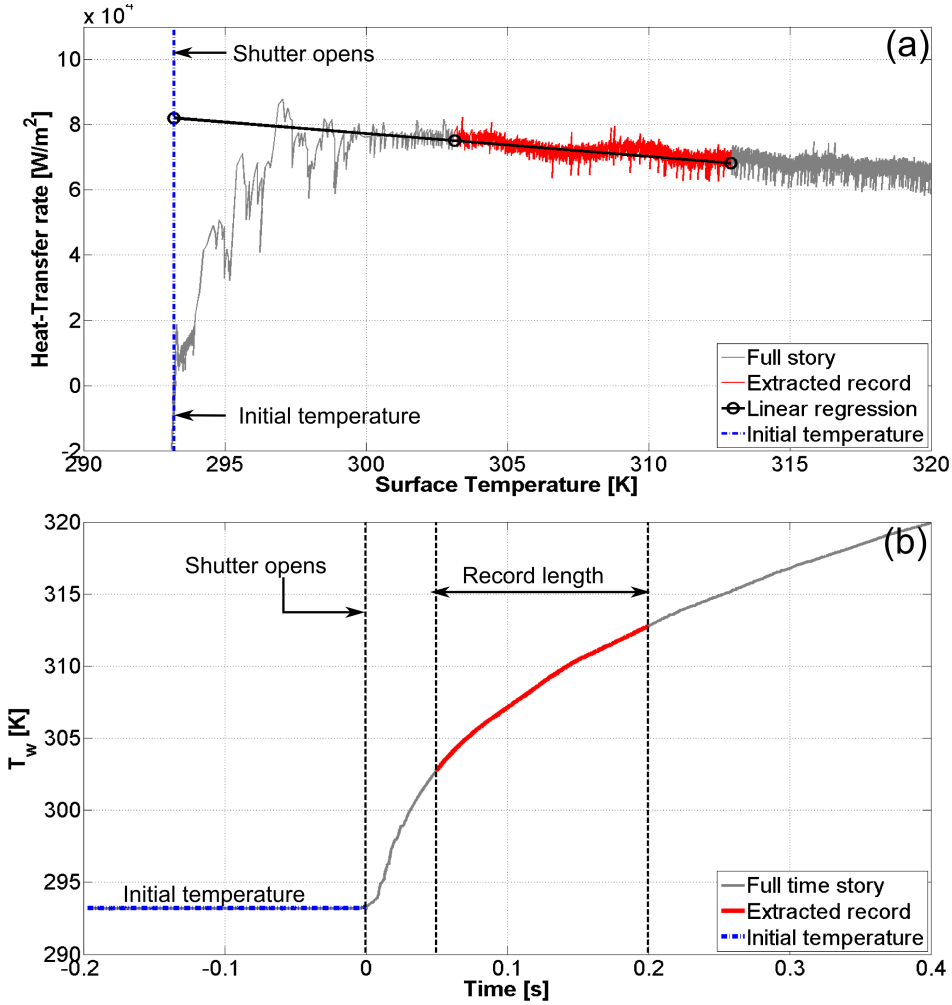

Figure 3.14: (a) $\dot{q}_w$ against T_w variation - (b) T_w variation in time

3.4 Constant temperature hot-wire anemometry

Hot-wire anemometry (HWA) is a well known and robust high bandwidth anemometry technique. With the name "hot-wire" (HW) is generally indicated the full probe and the circuitry of which the HW itself is a part: the sensing element, the two prongs that are holding it and the support (Fig. 3.15) are in fact a leg of the measuring circuit, typically a Wheatstone bridge.

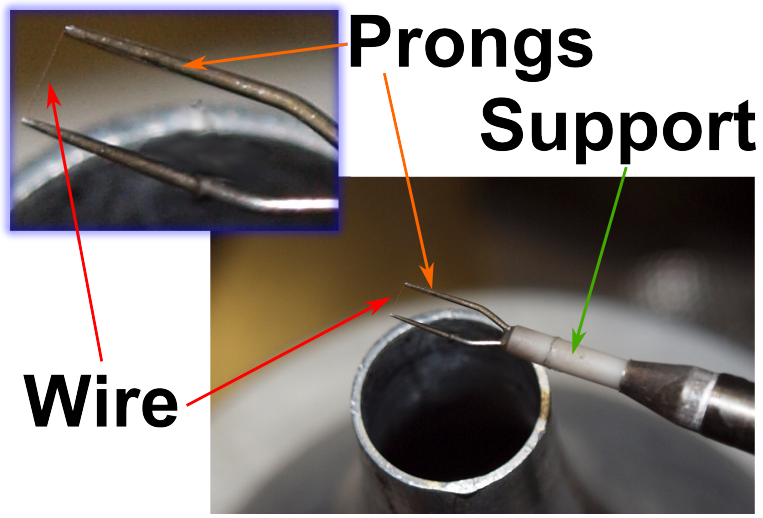

Figure 3.15: Typical straight HW probe

In the majority of the applications, the resistive bridge is operated at constant temperature (CTA). When the probe is inserted in a flow field, it will tend to vary its own temperature because of the convective action of the flow flowing across: by equipping the resistive bridge with a fast response feedback amplifier ("G" in Fig. 3.16), the current circulating through it can be adjusted in order to keep its own temperature (i.e. its resistance) constant. In turn, the bridge top voltage will vary, allowing therefore to set up a direct link between E_b and the velocity of the flow.

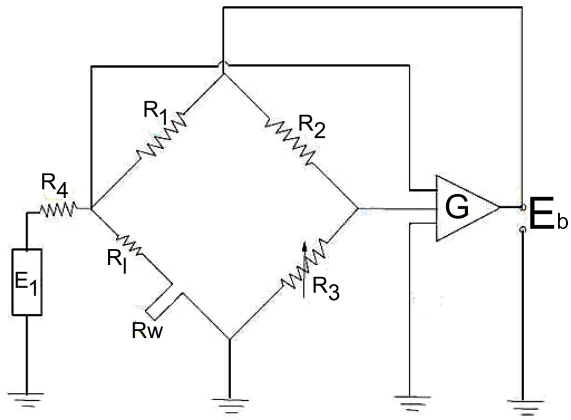

Figure 3.16: Constant temperature anemometry (CTA) Wheatstone bridge - Bruun [11]

The sensing element is normally a platinum-coated tungsten wire which is typically 5 - 9 [μm] in diameter. Its small dimensions joined with the reduced thermal inertia of the CTA operational mode, guarantees a high frequency response (up to 100 [kHz] in some cases) that makes of HWA a powerful tool for time resolved measurements.

3.4.1 Hot-wire anemometry principles

The physical principle on which hot-wire anemometry is based on is the convective heat transfer (Eq. 3.16) that takes place between the wire and the flow moving across it: the higher is the velocity of the flow, the stronger is the generated heat flux as well as the tendency of the wire to vary its temperature (and its own resistance). By measuring therefore the magnitude of this variation, a direct link can be set between the velocity of the flow and the voltage of the measuring circuitry. Keeping constant the surface exposed to the flow, the heat flux phenomenon results to be mainly driven by T_{ref} that, as it will be discussed afterwards, is directly linked to the

total temperature of the flow. In equation 3.16, if $T_{wire} - T_{ref} = 0$ then the heat transfer rate cancels: in order to perform a measurement by means of a HW anemometer, the wire must be heated above the flow temperature.

$$q = h \cdot A \cdot (T_{wire} - T_{ref}) \tag{3.16}$$

If one defines the Nusselt number (Nu_{wire}) based on the diameter of the wire (d_{wire}), Eq. 3.16 can be re-written in the form of Eq. 3.17, where k is the thermal conductivity of the fluid.

$$q = \pi \, d_{wire} \, l \, h \, (T_{wire} - T_{ref}) = \pi \, l \, k \, (T_{wire} - T_{ref}) \, Nu_{wire} \tag{3.17}$$

Assuming now a steady state heat transfer from the wire towards the flow, it can be stated that q equals the power supplied from the circuitry to the wire: $q = R_{wire} \, I_{wire}^2$, R_{wire} and I_{wire} being respectively the resistance and the current across the sensing element. As mentioned previously in the introduction to the present section, the HW probe coincides with the leg of a Wheatstone bridge whose top voltage E_b can be expressed as in Eq. 3.18, where R_t and R_l are the bridge top resistance and the resistance of leads respectively.

$$E_b = I_{wire} \, (R_t + R_l + R_{wire}) \tag{3.18}$$

Introducing therefore Eq. 3.18 into Eq. 3.17 by means of the relation described just above ($q = R_{wire} \, I_{wire}^2$), the formulation of the heat transfer from the hot-wire to the flow can be expressed in function of E_b (Eq. 3.19).

$$E_b = (R_t + R_l + R_{wire}) \sqrt{\frac{\pi \, l \, k \, (T_{wire} - T_{ref}) \, Nu_{wire}}{R_{wire}}} \tag{3.19}$$

As mentioned previously, T_{ref} is related to the total temperature of the flow T_0. As observed by Morkovin [50], if the wire would have not be heated, this temperature would have been only a function of the boundary layer development around its lateral surface. The latter consideration closely recalls what was stated in Sec. 2.2 about the adiabatic wall

temperature and it can be modelled by means of a recovery coefficient η_{wire} as follows: $T_{ref} = \eta_{wire} \cdot T_0$. In compressible flows, Bruun [11] demonstrated that the recovery factor is a function of the Reynolds number and of the Mach number. The dimensional-functional analysis takes therefore into account the density (ρ), velocity (u) and total temperature: $\eta_{wire} = f(Re, Ma) = f(\rho, u, T_0)$.

The thermal conductivity can be thought to be a function of the recovery factor since the transfer of heat is driven by the boundary layer temperature gradient. The latter is closer to the recovery temperature rather than to the total temperature and therefore it writes $k = f(\eta_{wire}) = f(\rho, u, T_0)$.

Considering forced convection and assuming the Prandtl number to be constant, the Nusselt number for a compressible flow depends again on the Reynolds number, the Mach number and on a non-dimensional temperature ϑ that can be thought as the ratio between T_{wire} and $\eta_{wire} \cdot T_0$. The functional expression for Nu_{wire} writes therefore $Nu_{wire} = f(Re, Ma, \vartheta) = f(\rho, u, T_0)$.

Assuming a typical CTA application (T_{wire}, R_{wire}, R_t and R_l are kept constant), the functional analysis on the terms of Eq. 3.19 leads to an important conclusion: the reading of a hot-wire anemometer in compressible flows is affected by density, temperature and velocity (Eq. 3.20).

$$E_b = f(\rho, u, T_0) \tag{3.20}$$

For the sake of of completeness, it has to be remarked that a more general expression of Eq. 3.20 should also take into account the effect of the flow angle. Keeping constant the modulus of the absolute flow velocity, it can be stated that the convective heat transfer coefficient that characterizes the flux of energy, has a maximum when the incoming flow is fully normal to the surface of the wire while its magnitude reduces as soon as the tangential component grows. In the first case, the bridge will provide a higher voltage output as higher is the tendency of the sensor to vary its temperature. Due

to this effect, an angular calibration is necessarily required as well as the use of a slanted probe to provide a good angular sensitivity. Since in the present work HWA was applied to characterize turbulence in the middle of a straight duct (Sec. 5.5), no marked variations of the flow angle were expected, which allowed in fact to adopt a straight sensor probe and to avoid its angular calibration.

3.4.2 Standard hot-wire applications

One of the first attempts to model the wire heat transfer and which actually was able to stand the test of time, is the so called King's law [44]. The coefficients of the relation (Eq. 3.21) are normally retrieved from a calibration procedure: by means of an atmospheric jet, velocity-voltage data can be simultaneously acquired and then curve-fitted as a typical power-law. It has to be remarked that, even though this relation is only a function of velocity, temperature and density still affect the measurements whose effects are hidden in the values of "B" and "n". As visible from Fig. 3.17 in fact, variations in terms of flow temperature produce different fittings, forcing the user to perform the calibration at the same density and temperature values (same Reynolds number) of those expected in the experiments.

$$E_b^2 - E_{b,0}^2 = B\,u^n \tag{3.21}$$

A consequence of what has been stated previously is that the use of the King's law is normally restricted to isothermal incompressible flow-fields. In the frame of the present work, hot-wire anemometry has been used in a compression-tube wind tunnel (Sec. 5.2) to characterize turbulent quantities behind a turbulence generator at different Reynolds numbers (see Sec. 5.3.5). The different density values at which tests were performed, together with the fluctuations of temperature induced by the presence of the grid (heat transfer) and by the intrinsic unsteadiness the flow in such a short-duration facility, make the use of a power-law calibration of no utility: a more complex methodology has to be applied which decouples the effect of each flow quantity on hot-wire readings.

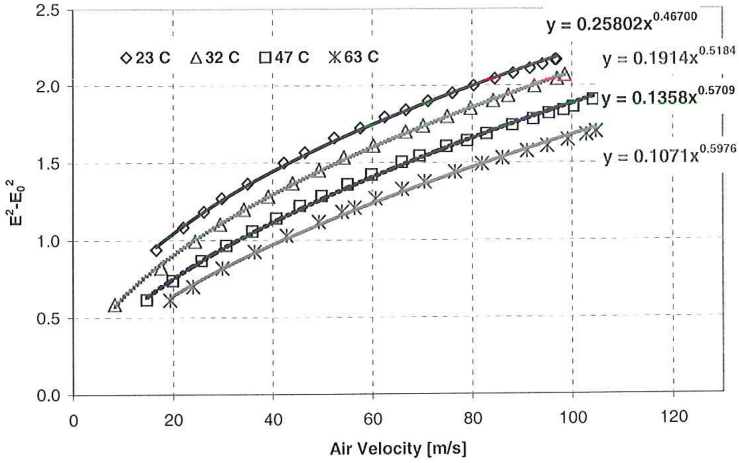

Figure 3.17: The effect of flow temperature on HW King's law calibration - From [80]

3.4.3 True HW velocity measurements in compressible-non-isothermal flows

Taking the total derivative of Eq. 3.20 one obtains Eq. 3.22 that can be re-written by means of the logarithmic derivative as in Eq. 3.23.

$$dE_b = \left(\frac{\partial E_b}{\partial u}\right)\bigg|_{\rho,T_0=cost} du + \left(\frac{\partial E_b}{\partial \rho}\right)\bigg|_{u,T_0=cost} d\rho + \left(\frac{\partial E_b}{\partial T_0}\right)\bigg|_{\rho,u=cost} dT_0 \tag{3.22}$$

$$\frac{e_b'}{\overline{E_b}} = S_u \frac{u'}{\overline{u}} + S_\rho \frac{\rho'}{\overline{\rho}} + S_{T_0} \frac{T_0'}{\overline{T_0}} \tag{3.23}$$

The latter formulation states that the three sensitivities of the wire (S_u, S_ρ and S_{T_0}) must be known in order to measure u. Moreover, it is an equation with three unknowns that naturally requires two more relations to close the system. A closure to the problem was given by Stainback et al. [1] that

used a three-wires probe whose sensitivities (in total nine coefficients) were computed by both, a methodical wind tunnel calibration (i.e. variation of one single flow parameter at time) and a multiple regression technique. In the first case, the calibration procedure results in an extremely time consuming process that necessarily requires ad-hoc facilities while the second approach demonstrated to be highly sensitive to errors propagation.

In the frame of the present work, to overcome these evident difficulties, the technique developed by Cukurel et al. [7] was implemented. He suggests to perform a typical HW calibration (flow velocity versus E_b) in a simple open-jet facility where the temperature and the velocity of the flow are randomly changed. By rearranging Eq. 3.19 into the form of Eq. 3.24 (Nagabushana and Stainback [52]), the bridge top voltage can be made non-dimensional as Nu_{wire} while the velocity could be expressed in terms of a Reynolds number Re_{wire} computed on the diameter of the wire (d_{wire}).

$$Nu_{wire} = \frac{E_b^2}{k(T_{wire} - \eta_{wire} T_0)} \left(\frac{R_{wire}}{\pi\, l\, (R_t + R_l + R_{wire})^2} \right) \tag{3.24}$$

In this formulation, the data cloud obtained by the temperature varying calibration (Fig. 3.18-a) should collapse into a single Re_{wire}-Nu_{wire} curve if the temperature of the wire T_{wire} is known. The latter can not be efficiently modelled or measured and that is why Cukurel computes it iteratively, by maximizing the R^2 value of a fourth order polynomial fitting of the non-dimensional population (Fig. 3.18-b and 3.18-c).

In "measurement" configuration, the HW bridge voltage is firstly transformed in terms of Nusselt number, requiring the flow total temperature to be measured by an independent probe. Once the non-dimensional calibration polynomial is applied, the flow density and viscosity must be computed to retrieve the velocity value from the calibrated Reynolds number. This can be done by acquiring also the flow total and static pressures that, together with the total temperature, allow to compute the flow static temperature with isentropic flow relations.

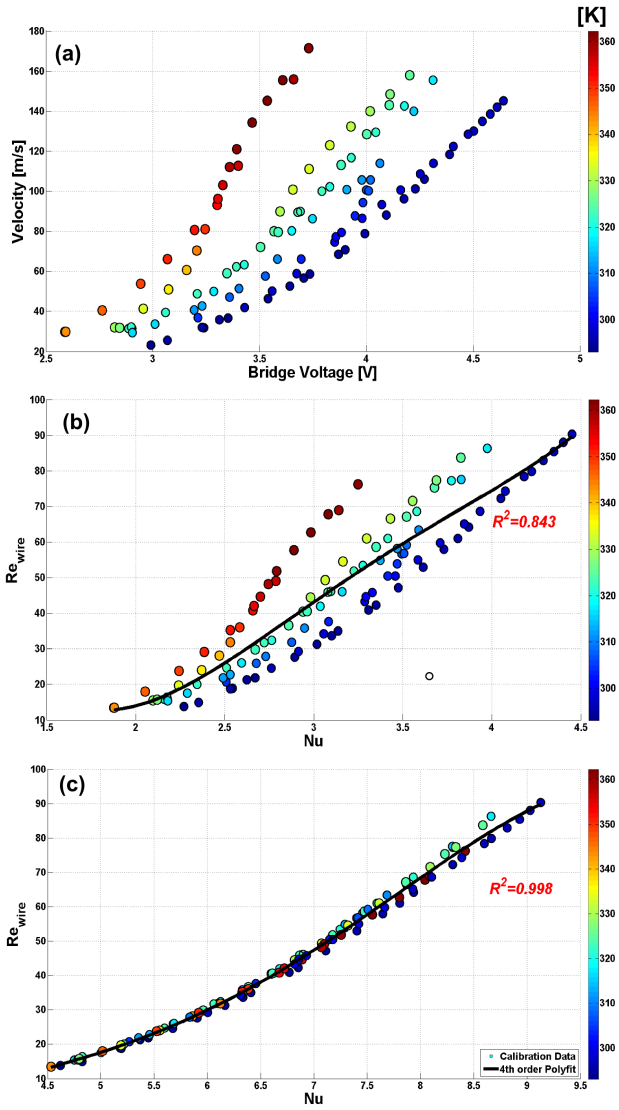

Figure 3.18: (a) The effect of flow temperature on HW calibration data; (b) Early stage of the non-dimensional iterative data reduction process ; (c) The result of the non-dimensional iterative data reduction

It has to be highlighted in the end that the procedure described up to now intrinsically assumes a negligible effect of the Mach number. Cukurel extended it to high compressible flows and he also implemented the dependency of E_b on the flow angle by introducing a second slanted wire.

Chapter 4

Characterization of the endwall cooling effect on the aero-thermal performance of a high pressure turbine rotor blade

4.1 Introduction

The present chapter reports on the experimental activity carried out at the *Energy Systems and Turbomachinery Laboratory* of the University of Bergamo (Italy) in the frame of a project commissioned by "Ansaldo Energia". The research focused on the description of the effect that the endwall film-cooling system (ten holes on the endwall next to the pressure side) had on both, the thermal protection and the aerodynamic efficiency of the cascade, with particular attention devoted to the study of the interactions between injection and endwall secondary flows. In the following, the test section and the wind tunnel will be firstly introduced, describing in detail the testing conditions and on instrumentation of the facility. Aerodynamic

and thermal results will be presented for both the cases, with and without injection. The scaling of the measurements the real engine conditions will be performed and the uncertainty analysis carried out.

4.2 Model and wind tunnel design

The rotor blade under investigation presented a strong three-dimensional design: besides the typical twisted shape, sweep and leaning of the profile were also adopted. The endwall of the blade was slightly opening while an extended fillet was present at the junction between the endwall and the blade itself. The geometry made a massive use of the film-cooling technology: both suction side (SS) and pressure side (PS) presented several rows of shaped-staggered cooling holes while a typical "shower-head" configuration was well visible in leading edge (LE) area. The trailing edge (TE) was cooled by means of cutback slots on the pressure side and, in the end, the rack of holes under investigation was placed at the hub.
In order to be tested in a linear cascade configuration, a cylindrical model had to be obtained out the highly 3D original geometry. Since, as mentioned before, the research activity was concentrated on the effect of ejection from the endwall holes, the blade profile at the upper limit of the fillet was selected. This choice was supported by considering that, given the target of the study, it was of crucial importance to preserve the pressure field of the blade close to the endwall area rather than in other position along the height. According to the previous consideration, the model was also equipped with a fillet between and the hub and the blade itself. Since in the original geometry this features developed over an inclined endwall which was not preserved in this case, some modifications had to be taken: it was chosen to implement a circular fillet, having the LE and TE radii equal to the original geometry. The fillet was then developed along the blade surfaces by imposing the tangency constraint on both the blade and the endwall and by preserving the distance between its extent on the hub and the exit of each hole, as in the original airfoil. Since the facility had to be completely redesigned, a full scale model was adopted.

Like in real engines, every blade was designed with a support slot to allow for a correct mounting in the wind tunnel. Slots have been designed adopting a modular criterion so that it was possible to check the effect of positioning on the periodicity. Labyrinths have been adopted for both the slot-to slot and the slot-to-tunnel joints in order avoid any possible source of leaking. A seven blades linear cascade was in the end assembled whose main characteristics are reported in Tab. 4.1. with respect to frame of reference of Fig. 4.1. Since thermal measurements had to be performed, a low conductivity material was selected: the cascade was entirely made up of Plexiglass® whose characteristics are summarized in Tab. 4.2.

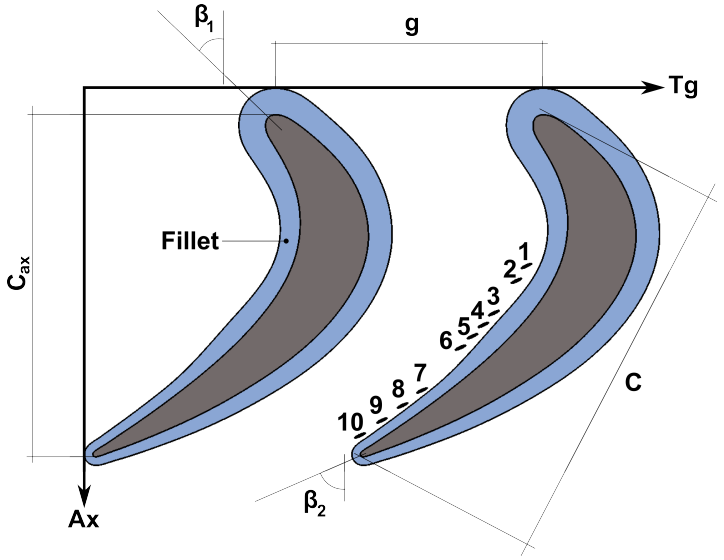

Figure 4.1: Frame of reference for the cascade geometrical parameters reported in Tab. 4.1

The original geometry of the cooling holes was kept in the model. In particular, attention was paid in preserving the length over diameter ratio as it is of crucial importance for the ejection performance of the holes (discharge coefficient). As visible in Fig. 4.2, a feeding plenum was foreseen

Description	**Symbol**	**Value**
# of blades		7
Height $[mm]$	H	147
Pitch $[mm]$	g	80
Chord $[mm]$	C	116.7
Axial chord $[mm]$	C_{ax}	102.54
Inlet angle $[°]$	β_1	44.26
Outlet angle $[°]$	β_2	-64.19

Table 4.1: Cascade geometry

Plexiglass®	
Tensile modulus $[MPa]$	300
Tensile strength $[MPa]$	7-8
Thermal conductivity $[W/mK]$	0.19

Table 4.2: Plexiglass® characteristics

at the base of the blade which fed all the ten holes: besides the 3D design of the blade, this peculiarity corresponds to the main difference between the model and the real geometry where, in fact, a dedicated plenum with different total conditions was foreseen for the first two holes. In the end, it must be remarked that the inclination from the surface (angle "F" in Tab. 4.3) had a much lower value than those normally found in literature (between 20 and 35 $[°]$): a strong resistance to separation could be expected for the present configuration. The geometric characteristics of each hole are instead reported in Tab. 4.3 with respect to the frame of reference placed aside.

Hole	X/C_{ax}	E	F	D	l/D
		[°]	[°]	[mm]	
1	0.44	41.09	11.5	0.7	18.743
2	0.484	41.09	11.5	0.7	19.743
3	0.578	41.09	11.5	0.7	24.043
4	0.612	41.09	11.5	0.7	25.071
5	0.646	41.09	11.5	0.7	25.943
6	0.679	41.09	11.5	0.7	27.057
7	0.804	41.09	11.5	0.7	36.086
8	0.848	41.09	11.5	0.7	39.329
9	0.892	41.09	11.5	0.7	43.2
10	0.935	41.09	11.5	0.7	48.143

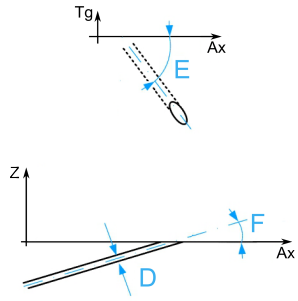

Table 4.3: Holes geometric characteristics with respect to the frame of reference aside

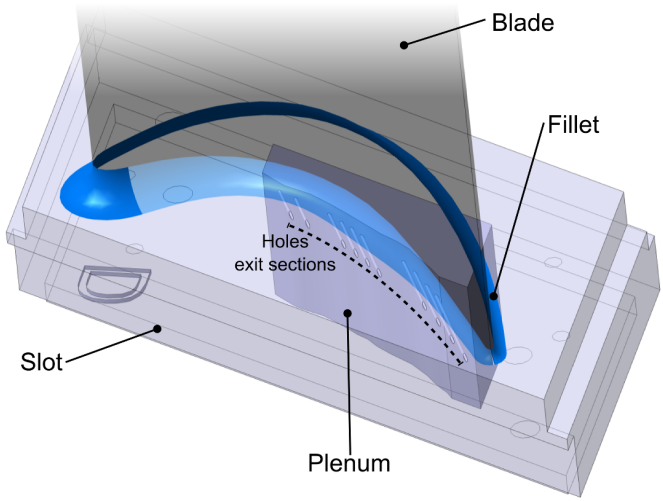

Figure 4.2: Position of the feeding plenum with respect to the blade and the exit sections of the holes

The model was tested in an open-loop suction type facility designed specifically for the present investigation. A sketch of the wind tunnel is reported in Fig. 4.3: an industrial fan (7) draws the ambient air through the fabric filter (0) placed at the beginning of the inlet duct (1). The test section (2) is mounted at the end of the latter, in such a way that the discharge metallic direction is aligned with the horizontal of the laboratory. In the end, the outlet channel (3) is connected to the fan by means of an adjustable squared diffuser (4). The facility is fully transparent to allow for optical measurement everywhere in the test section. Compressed air was used to feed the cooling system. It consisted of a settling chamber which is connected to an orifice plate (designed according to ISO 5167 norm) to precisely measure the coolant mass-flow. Downstream the orifice plate, an electrical heater was foreseen to warm the flow up to the desired temperature before entering the feeding plenum.

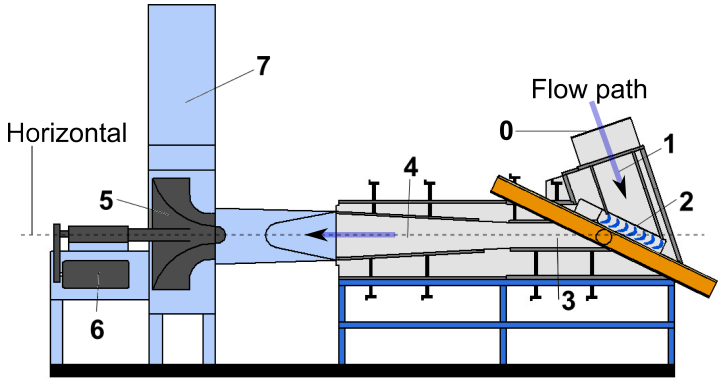

Figure 4.3: Simplified sketch of the facility: (0) Fabric filter; (1) Inlet duct; (2) Cascade; (3) Outlet duct; (4) Diffuser; (5) Fan; (6) Fan motor; (7) Fan discharge channel

4.3 Instrumentation of the facility

Upstream the LE plane, the total inlet pressure P_{01} was measured in three different positions along the channel width to control the homogeneity of the flow. The static inlet pressure P_1 was measured as well by means of a wall static pressure tap. When needed, the total pressure probe have been substituted by a hot-wire probe. A rack of 34 wall static pressure taps was foreseen at 30% of the axial chord downstream the TE plane in the axial direction, covering more than 4 pitches of the cascade. In the downstream section a traversing system was also present: it allowed to traverse a pressure probe along the tangential direction as well as to span almost the whole height of the blade. By adjusting the probe support, the position of the measuring plane was varied in a range spanning from 8% to 108% of C_{ax}. The coolant total pressure P_{0c} and total temperature T_{0c} were measured in the plenum placed at the base of the cooled blade while, as indicated previously, the global injected mass-flow is measured by the orifice plate located further upstream. A solid blade (no cooling holes) was equipped with several static pressure taps placed on the endwall in correspondence of the exit sections of the cooling holes to retrieve the local static pressure $P_{\infty,hole}$.

4.4 Test conditions and matrix of experiments

Since the wind tunnel was freshly designed for the present investigation, a characterization of the incoming flow was performed. Inlet flow homogeneity and boundary layer have been measured for two downstream isentropic Mach numbers, 0.2 and 0.3 respectively, while the inlet turbulence intensity ($Tu\%$) was assessed only for the latter case. The test section was also characterized: blade loading at midspan and downstream periodicity have been investigated for the highest flow regime. Regarding the injection conditions, it was decided to define the investigation range by setting a variability interval for the inlet loss-free blowing ratio M_{inlet}. The latter parameter was introduced by Friedrichs et al. [27] and describes the mass-flux ratio that

an ideal hole would present when blowing at inlet conditions. As clearly visible from its definition in Eq. 4.1, it is a convenient parameter as it depends on pressure values directly measured at every test showing, moreover, a much smaller uncertainty than the one related to the measurement of the coolant mass-flow (see Sec. 4.9). Tests with injection have been performed for M_{inlet} spanning from 1.61 up to 4. A full set of aerodynamic and thermal measurements was performed at $Ma_{2s} = 0.3$. In particular, pressure probe measurements have been performed in two different planes, respectively at the 8% and 30% of the axial chord downstream the TE plane. The measurements performed in the frame of the characterization of the wind tunnel are presented in Tab. 4.4 while the full matrix of aerodynamic and thermal experiments are summarized in Tab. 4.5.

$$M_{inlet} = \sqrt{\frac{P_{0c} - P_1}{P_{01} - P_1}} \tag{4.1}$$

Ma_{2s}	0.2	0.3
Homogeneity	X	X
Boundary Layer	X	X
Turbulence intensity $Tu\%$		X
Blade loading		X
Cascade periodicity		X

Table 4.4: Wind tunnel characterization

$Ma_{2s} = 0.3$					
M_{inlet}	0	1.61	2.41	3.22	4
Aerodynamic tests	$8\%C_{ax}$ $30\%C_{ax}$	$8\%C_{ax}$ $30\%C_{ax}$	$8\%C_{ax}$ $30\%C_{ax}$	$8\%C_{ax}$ $30\%C_{ax}$	$8\%C_{ax}$ $30\%C_{ax}$
Thermal tests	X	X	X	X	X

Table 4.5: Matrix of experiments

4.5 Wind tunnel characterization

The homogeneity of the incoming flow was checked by means of a 3-hole probe positioned in three different locations along the inlet duct width: one in the center of the channel and two symmetrically shifted of 70 [mm] with respect to it. By means of the calibration procedure outlined previously in Sec. 3.1.1, the local total and static pressures as well as the flow angle could be retrieved. Fig. 4.4-a and Fig. 4.4-b report in fact the distribution of the upstream Mach number Ma_1 and of the upstream flow angle β_1, for two different values of Ma_{2s}, nominally 0.2 and 0.3. As visible, the velocity of the main-stream kept homogeneous over the three position investigated, with a maximum relative difference equal to 3.7% at $Ma_{2s} = 0.2$. The flow angle tended instead to slightly grow towards the right hand side of the inlet duct even though the maximum variation was smaller than 0.05 [°] that is completely within the uncertainty of such a measurement (Sec. 4.9). The inlet boundary layer was characterized by traversing a flattened Pitot probe. The measurement location was placed in the middle of the channel and at the $95\%C_{ax}$ upstream the leading edges plane. The velocity profiles for two isentropic downstream Mach numbers ($Ma_{2s} = 0.2 \div 0.3$) are reported in Fig. 4.5 while Tab. 4.6 presents the computation of the integral parameters for the highest Ma_{2s}. It has to be highlighted that, by computing the shape factor $H_{1,2} = \delta^*/\theta$, a typical value for a turbulent boundary layer is obtained, being in fact $H_{1,2}$ equal to 1.3.

δ	[mm]	26.4
δ^*	[mm]	2.1
Θ	[mm]	1.6

Table 4.6: Inlet boundary layer integral parameters

The inlet free stream turbulence intensity Tu% has been measured by means of a constant temperature hot-wire probe. The anemometer, a 0.5 [μm] straight DANTEC hot-wire, was operated by a DANTEC StreamLine bridge. No calibration has been performed in this case since Tu% could be computed directly from the mean and the RMS of the voltage itself, provid-

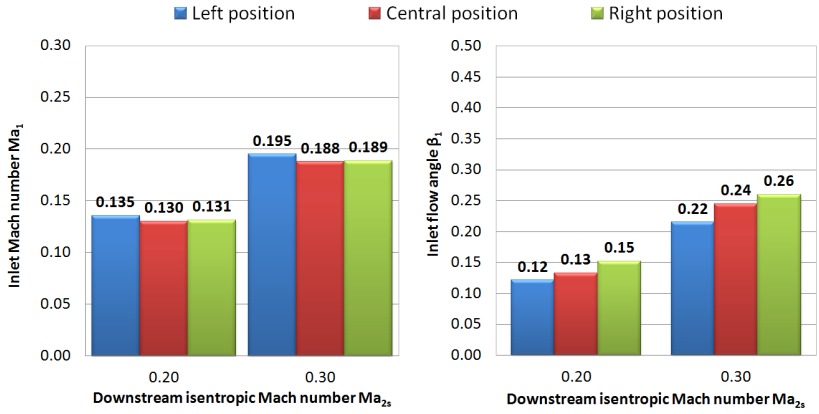

Figure 4.4: Homogeneity of the inlet flow field: (a)-Mach number and (b)-Flow angle

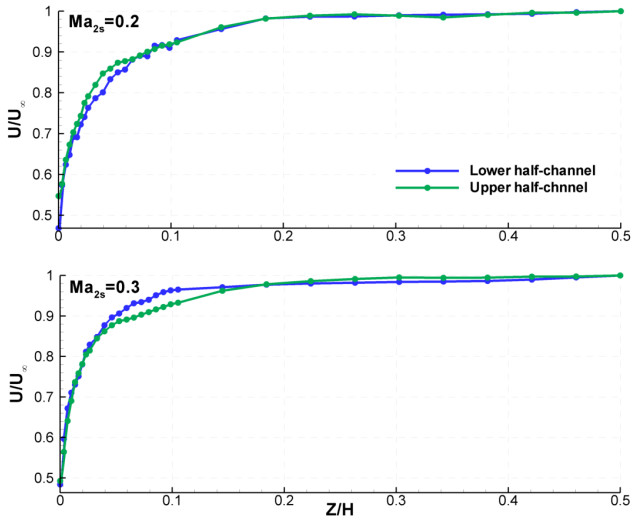

Figure 4.5: Inlet duct boundary layer profiles for two isentropic downstream Mach numbers, 0.2 and 0.3 respectively

ing anyway to use a proper over-heat ratio. For $Ma_{2s} = 0.3$, a turbulence intensity of about 1% was measured in the middle of the channel.

The blade loading has been measured by means of a DANTEC Fiber-Flow two components laser doppler velocimetry system (LDV). The light source was provided by a 300 [mW] Ar+ laser whose beams were focused to obtain a measuring volume of 0.11 [mm] in diameter and 2.38 [mm] long. The seeding of the flow was provided by a sawdust burner. Measurements were performed at 3 [mm] from the blade surface at midspan, acquiring 20000 bursts per measuring point. Results are presented in Fig. 4.6 in terms of local isentropic Mach number and show a typical mid-loaded distribution with a velocity plateau between $X/C_{ax} = 0.5$ and $X/C_{ax} = 0.8$. At this point, a moderate diffusion takes place until the trailing edge. On the pressure side, at $X/C_{ax} = 0.05$, the velocity distribution drops because of the creation of a small laminar separation bubble. The existence of the latter is confirmed by the oil visualization in Fig. 4.7, where a conspicuous deposition of material is evident right downstream the LE. A continuous acceleration begins then at $X/C_{ax} = 0.2$ that becomes steeper at $X/C_{ax} = 0.5$, accelerating the flow until the TE.

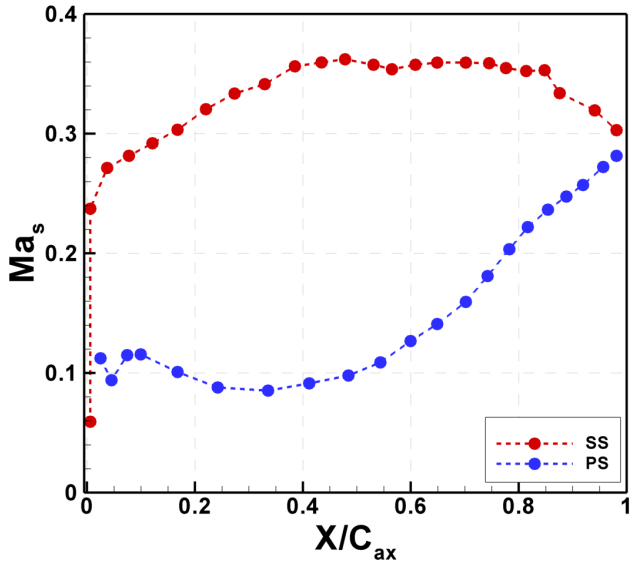

Figure 4.6: Measured blade loading at midspan

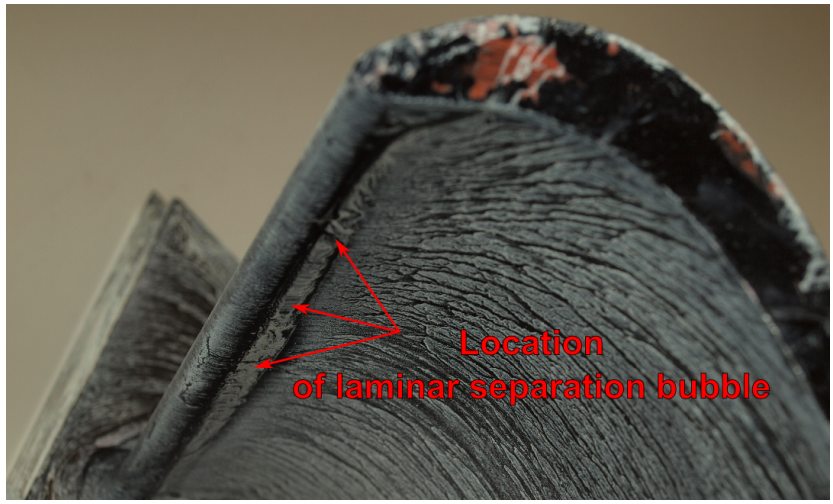

Figure 4.7: Oil visualization of the pressure side leading edge region

The periodicity of the cascade was checked by means of the rack of 34 static pressure taps at 30%C_{ax} downstream the TE plane. By acting on the downstream adjustable tailboards, the static wall pressure distribution was iteratively tested until the most homogeneous conditions was found. Fig. 4.8 reports the distribution of the isentropic downstream Mach number which, in general, presents a quite flat evolution with a pronounced periodicity especially in correspondence of the investigated channels (red vertical lines).

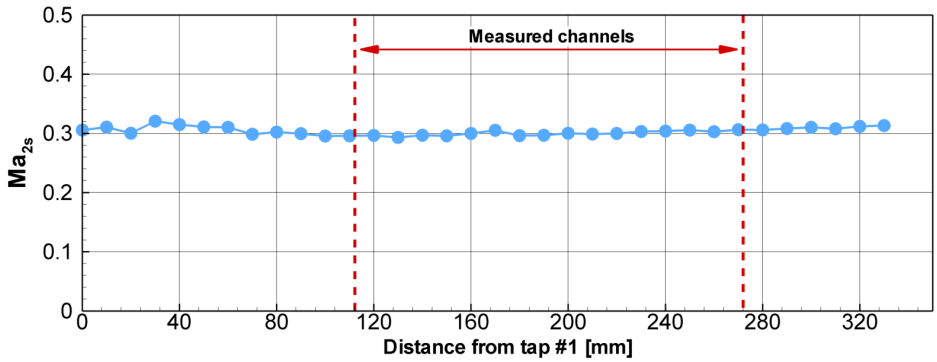

Figure 4.8: Downstream Ma_{2s} distribution for periodicity check

4.6 Aerodynamic measurements

In this section, the results of the aerodynamic investigation are presented in terms of kinetic energy loss coefficient, vorticity and secondary velocity distributions. Oil visualizations were also performed to enhance the understanding of the flow-field. The non-cooled case (no injection from cooling holes) will be firstly considered in order to highlight the differences with the cooled ones presented afterward. In the following, also the cooling system will be characterised.

4.6.1 Non-cooled cascade

A miniaturized 5-hole pneumatic pressure probe (Fig. 4.9) was used to investigate the downstream flow field. It consists in a 1.6 [mm] in diameter and 50 [mm] long head connected to a stem in a typical L-shaped configuration. The probe was previously angular calibrated in an *ad hoc* calibration facility for a yaw angle and pitch angle ranges equal to ±28 [°] and ±18 [°] respectively and for a Mach number spanning from 0.05 up to 0.6.
The probe has been traversed along two different measurement planes placed respectively at $8\%C_{ax}$ and at $30\%C_{ax}$ downstream the TE. The wind tunnel traversing system allowed to investigate two cascade pitches in the tangential direction while, along the blade height, only 98% of the span was covered because of geometrical constraints. To enhance the resolution of the results next to the wall, a finer measurement grid was adopted in the region: a total of 59 points along the blade span were acquired while, in the pitch-wise direction, 30 points per channel have been investigated.

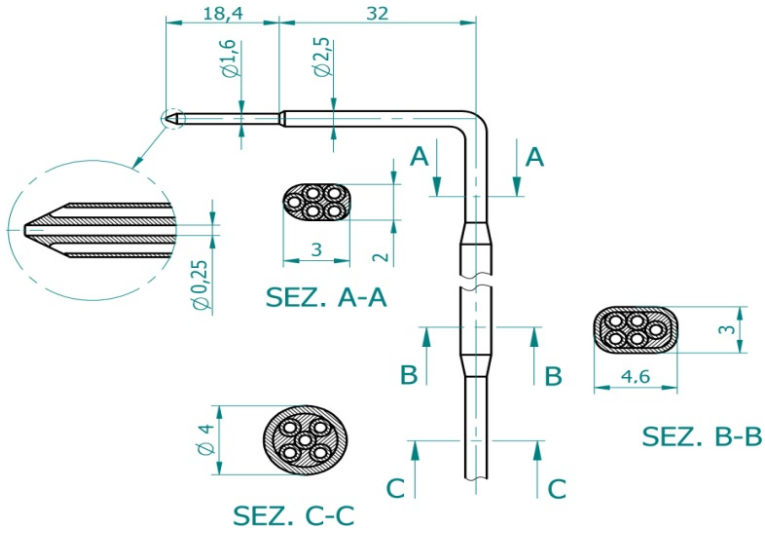

Figure 4.9: Technical drawing of the used 5-hole pressure probe

Results will be presented in terms of kinetic energy loss coefficient ζ (Eq. 2.9) as well as secondary velocity and stream-wise vorticity (Ω_s) distributions. The latter parameter is a fundamental quantity for the definition of the secondary structures affecting the flow-field. Considering a bi-dimensional stream-line, the stream-wise vorticity corresponds to the component of the 3D vorticity vector which is locally tangent to the stream-line itself (Fig. 4.10-a). The normal and the bi-normal components define instead the so called secondary velocity plane (Fig. 4.10-b) to which Ω_s is normal.

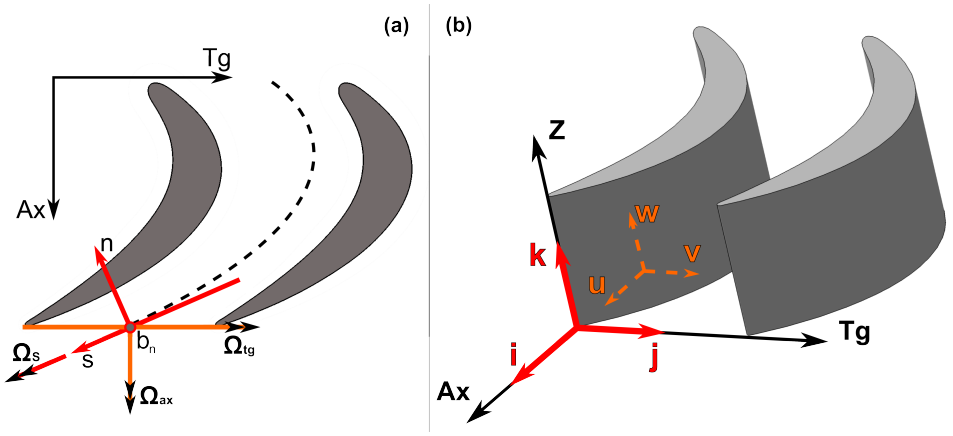

Figure 4.10: (a)Tangential-axial-span-wise frame of reference - (b)Components of the stream-wise vorticity vector

Following the study of Gregory-Smith et al. [32], the secondary plane can be defined by the average flow direction at midspan since the absence of secondary structures guarantees in that location the existence of a genuine two-dimensional flow field. The latter definition coincides in fact with an assumption that, as demonstrated by Persico et al. [59], can be efficiently taken in the case of linear cascades. According to the vectorial composition in Fig. 4.10-a, Ω_s can be retrieved by means of Ω_{ax} and Ω_{tg}, the vorticity vectors in the axial and tangential directions respectively. Anyway, only

Ω_{ax} can be directly computed from a probe traversing along the Tg-Ax plane (see its definition in Eq. 4.2), therefore the tangential component has to be estimated. In the present work, the procedure defined in [32] was applied which computes Ω_{tg} starting from the axial component and the span-wise pressure gradient, as shown in Eq. 4.3.

$$\Omega_{ax} = \frac{\partial v}{\partial k} - \frac{\partial w}{\partial j} \tag{4.2}$$

$$\Omega_{tg} = \frac{\partial u}{\partial k} - \frac{\partial w}{\partial i} = \frac{1}{u}\left(\Omega_{ax}\nu + \frac{a^2}{\gamma}\frac{\partial lnP_0}{\partial k}\right) \tag{4.3}$$

The loss coefficient distributions are presented in Fig. 4.11 for the two investigated downstream planes ($8\%C_{ax}$ and $30\%C_{ax}$). They describe a typical flow field, dominated by the presence of two evident pairs of loss cores in both the upper and lower regions. Each pair is composed by a bigger core which extends deeper towards the centre of the blade channel while a smaller but more dissipative core keeps attached to the trailing edge (located at Y/g=0.7 - 1.7) and closer to the midspan. The loss cores are well detached from the endwalls, characteristic that should be addressed to the high turning of the cascade (108.45 [°]), while a slight asymmetry can also be observed as an effect of the presence of fillet at Z/H=0. In Fig. 4.11-up a very thin wake is visible at midspan that widens further downstream (4.11-down) because of the effect of the mixing process.
Fig. 4.12 shows the stream-wise vorticity and secondary velocities distributions for the two measurement planes. Near the filleted endwall, a single high-vorticity zone is located exactly in correspondence of the loss core identified in Fig. 4.11 in the suction side region (Y/g=0.45 - 1.45). The latter, further downstream (Fig. 4.11-down), strongly interacts with the counter rotating trailing vorticity, inducing a marked deformation of it at Z/H=0.2. The endwall region is characterized by an evident cross-flow (from pressure side to suction side) that tends to lift at Y/g=0.5 when approaching the SS, even though it is impossible to recognize any secondary feature related to the presence of the corner vortex.
The upper half of the blade channel shows instead a completely different

vorticity patter. Besides the trailing vorticity, four distinct cores can be recognized: two positive vortices "A" and "C" are spaced by two counter rotating zones, "B" and "D" respectively. This particular distribution is preserved also at $30\%C_{ax}$ where a strong deformation of the trailing edge shed vorticity can be appreciated. The endwall region presents again a strong cross-flow from pressure to suction side, with a marked tendency to lift already at Y/g=0.4. A corner vortex is now present in this zone which could not tackled by the measurements since they are not covering the full span.
Oil flow visualizations have been performed in order to identify the origin of such a vorticity pattern. The rear part of suction side is pictured in Fig. 4.13 where it can be immediately appreciated how secondary structures differ in tip and hub sections. The latter is dominated by the presence of the passage vortex (PV_{hub}) which, according to both visualisations and vorticity maps, has its separation line at about $20\%H_{blade}$. Closer to midspan and further upstream along the surface, the trace of the suction side leg of the horseshoe vortex can be recognized (HSs_{hub}), counter-rotating with respect to PV_{hub} and vanishing when approaching the trailing edge, as suggested by the streaklines pattern. Absolutely no corner vortex can be recognized: the fillet region is most probably so extended (5.4% of the blade height at LE) that the hub cross-flow (Fig. 4.12 at Z/H=0) is directly rolled-up by PV_{hub} without creating any separation line next to the blade (Sharma et al. [70]). A closer view of the SS at the hub is presented in Fig. 4.14 where also the LE zone is visible: the visualisation shows how HSs_{hub} (identified by the two separation lines $(S_1 - S_2)_{ss}$) is "pushed" towards the midspan by the fillet immediately downstream the LE of the blade. The traces of the separation lines coming from the PS of the adjacent blade ($(S_1 - S_2)_{ps}$) are also visible on the endwall: they reach the SS in a point where the passage vortex is already well developed which causes the pressure side branch of the horsehoe vortex (HSp_{hub}) to be enrolled directly in the co-rotating PV_{hub}, as shown also by different authors (Doerffer et al. [19] and Gregory-Smith [31]).

On the opposite side of the blade height, in the so called tip region of Fig. 4.13, three different zones can be recognized. An evident reattachment

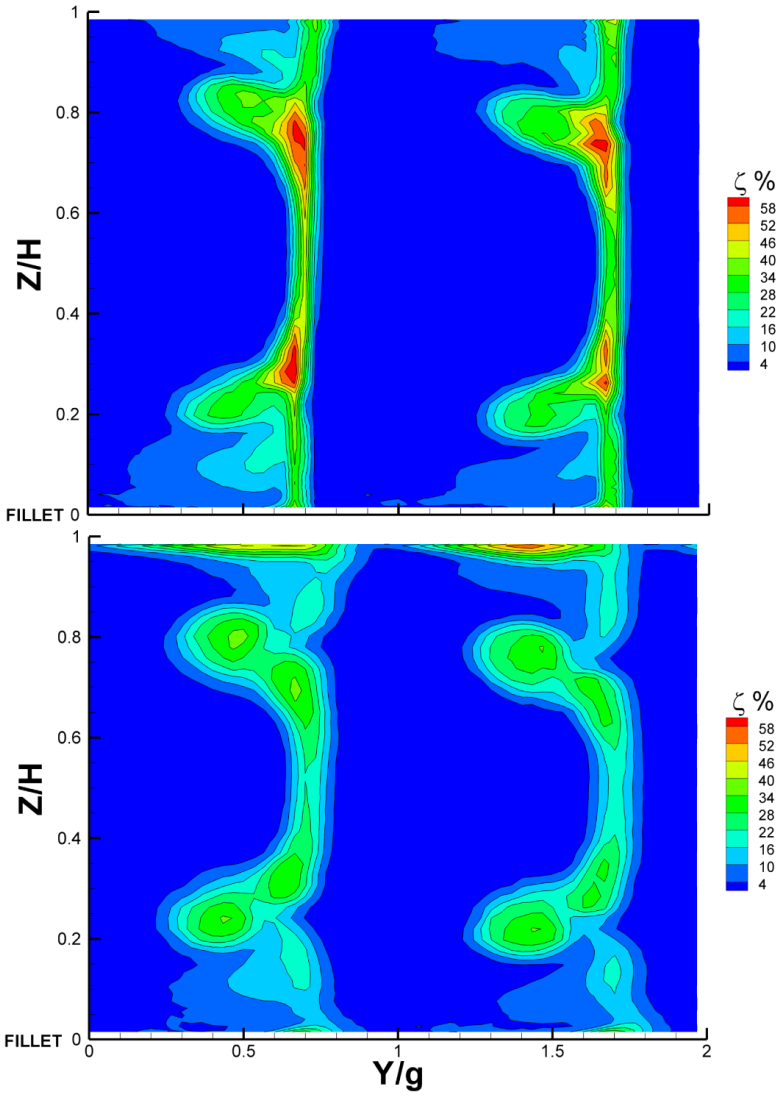

Figure 4.11: Kinetic energy loss coefficient distribution at 8%C_{ax} (upper) and 30%C_{ax} (lower)

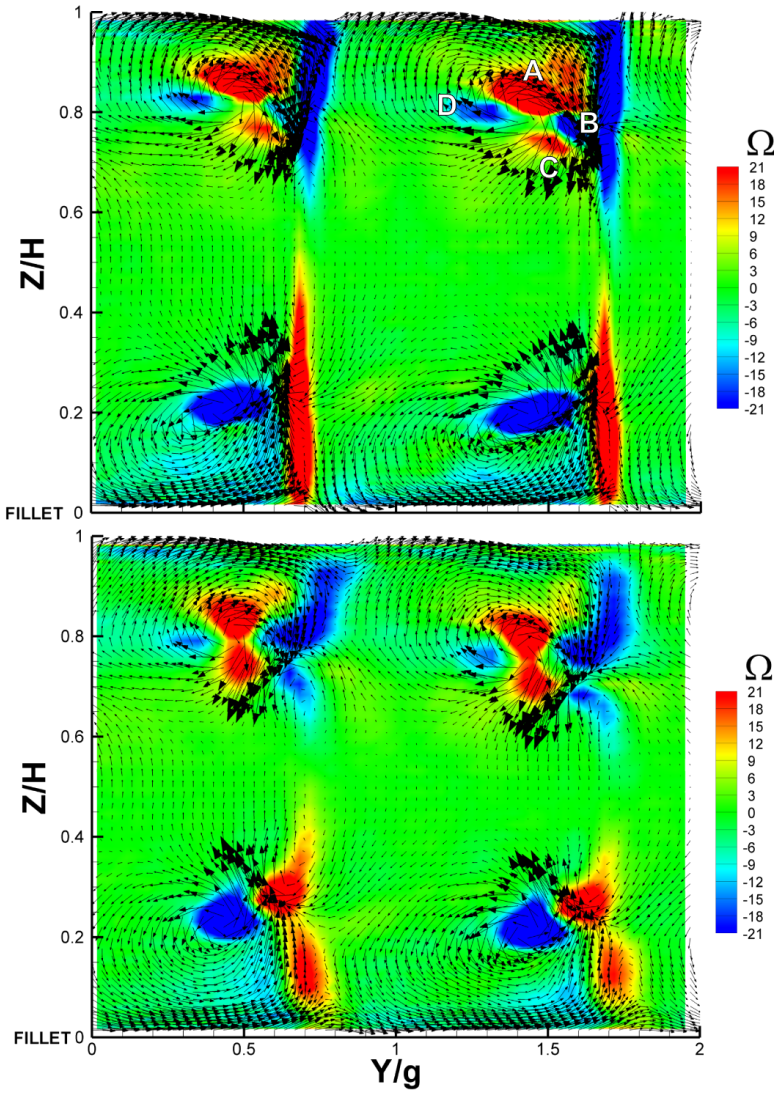

Figure 4.12: Non-dimensional stream-wise vorticity $\Omega_s C/U_1$ and secondary velocity vectors at $8\%C_{ax}$ (upper) and $30\%C_{ax}$ (lower)

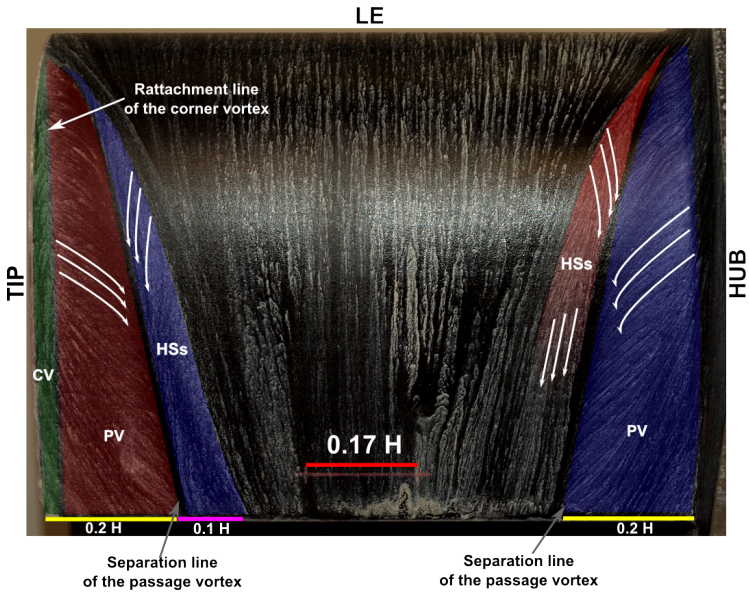

Figure 4.13: Suction side oil flow visualisation

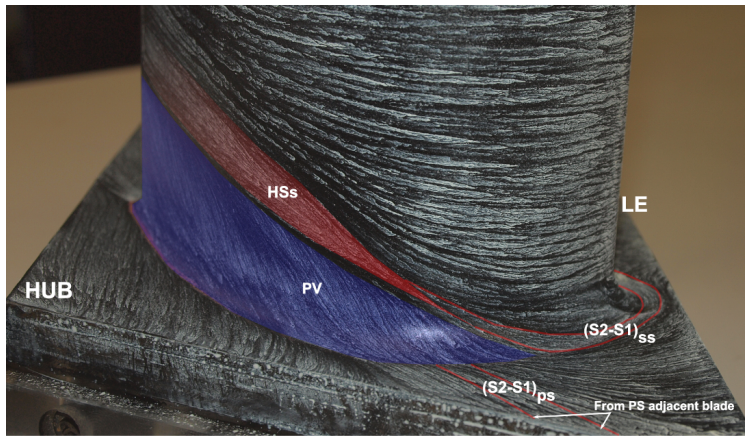

Figure 4.14: Detail of the oil flow visualisation of the suction side next the endwall

line is well visible close to the tip, identifying the corner vortex CV that in the loss and vorticity distributions could not be seen. A counter-rotating PV trace is also visible whose extension, equal to $20\%H_{blade}$, is in agreement with the results found previously (the loss core in Fig. 4.11-up at Z/H=0.8 and the negative vorticity area in Fig. 4.12-down at Z/H=0.8-0.9 , Y/g=0.5). The wall trace oh the tip suction side horseshoe vortex HSs_{tip} can be recognized closer to the mid section: this counter-rotating vortex (with respect to the neighbouring PV), which was in fact well visible also in Fig. 4.12-up at (Y/g=1.6 ; Z/H=0.75), can be found also at the tip endwall (Fig. 4.15) where two wide $(S_1 - S_2)_{ss}$ separation lines start from the LE to close afterwards on the suction side. Further downstream, the reattachment line for the corner vortex CV widens while approaching the TE, providing a further demonstration of the existence of this secondary structure.

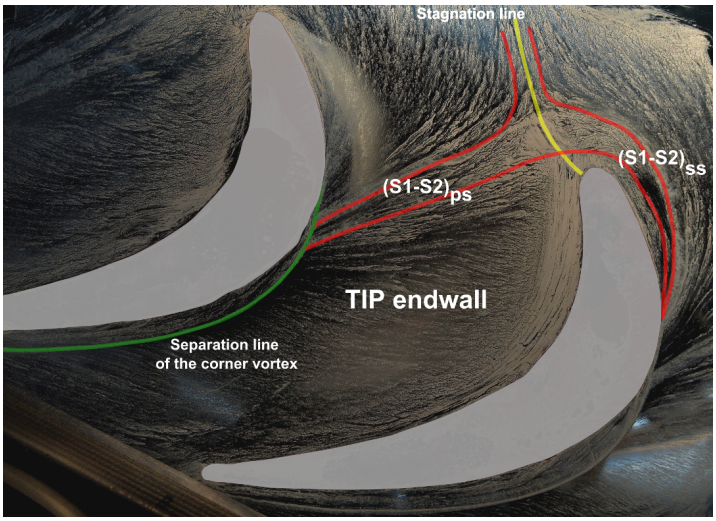

Figure 4.15: Flow visualisation of the tip region endwall

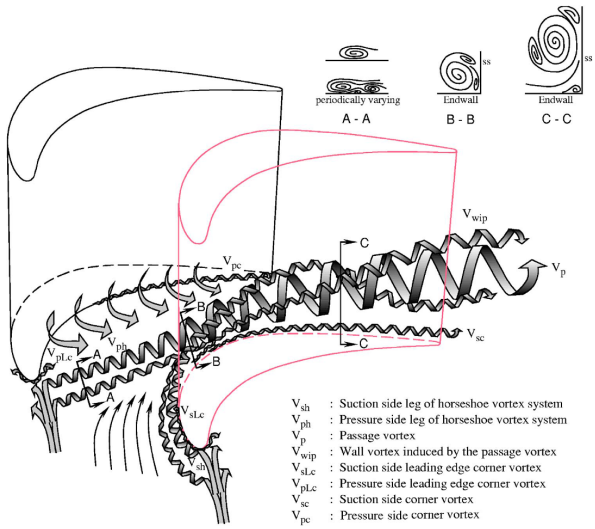

Figure 4.16: Secondary flows model after Wang [78]

The counter-rotating vorticity areas "C" and "D" in Fig. 4.12-up cannot be justified at this point since no evidence of their generation was found in the visualizations, anyway some hypothesis can be drawn of the base of the different secondary flows models developed so far. In particular, it can be thought that the strong transversal gradient at the endwall energizes the HSp_{tip} that reaches the SS in an zone where PV is already well developed ($(S_1 - S_2)_{ps}$ in Fig. 4.15). Here it is lifted towards midspan by the high turning of the profile, wrapped around the passage vortex and pushed closer to the midsection (position C in Fig. 4.12-up). Regarding the negative vorticity core D, the model of Wang et al. [78] can be used to explain its origin: the author, by means of smoke-visualizations, identified in fact the birth of a PV induced wall vortex, V_{wip}, rotating around the passage vortex core in pair with HSp_{tip}. In section C-C of Fig. 4.16, the author suggested in fact a secondary flow structure that recalls closely the one presented previously in Fig. 4.12-up in the tip region.

By mass-averaging along the tangential direction, one obtains the span-wise evolution of the loss coefficient and flow angle which is presented in Fig. 4.17-a and Fig. 4.17-b with respect to the values measured at midspan. The two plots show an evolution typical of a high turning blade, with just one marked loss peak in every semi-channel, which corresponds to the previously identified passage vortex locations. In particular, closer to the TE (red line in the two plots), the tip passage vortex peak (Z/H=0.8) is higher than the one of the filleted hub, in agreement with the results of Sauer et al. [66] and Han and Goldestein [36]. Close to the walls, the tip region shows again a slightly higher loss coefficient than the one at the hub, which is related to the presence of the corner vortex (Fig. 4.13). This evidence was found also by Zess and Thole [81] who, anyway, investigated the secondary flow plane only next to the LE, without providing any description of the flow field farther downstream. Han and Goldestein, on the contrary, described an enhancement of the corner vortex even though for a geometry definitely different from the one adopted in the present: in their case, a straight and constant fillet was developed around the blade starting from an elliptical, asymmetric and sharp-slope LE bulb. As visible from their results, in this particular configuration the SS and PS corner vortexes are generated earlier in the flow field, at the junction between the bulb and the endwall.

From the loss coefficient distribution at the $30\%C_{ax}$ downstream the TE plane (blue line in Fig. 4.17-a), the effect of mixing can be deduced: the evolution homogenises in the central area, forcing the PV peaks to assume the same magnitude, while the tip corner-vortex related loss drastically increases.

In the trailing edge zone, the secondary flow deviation angle (Fig. 4.17-b) is characterized by an almost symmetrical distribution with underturning peaks of similar magnitudes (about -7 [°]). The tip overturning peak tends to reduce very close to the wall as an effect of the presence of the counter-rotating corner vortex. The overturning reduction becomes drastic in this zone when going farther downstream: the stronger corner vortex diminishes the deviation angle of about 50%.

In the end, losses can be expressed by means of a pitch-wise-span-wise

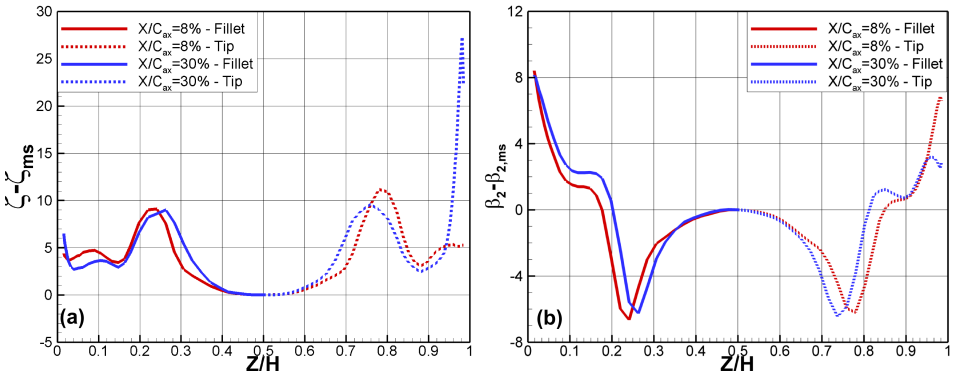

Figure 4.17: Pitch-wise mass-averaged loss coefficient (a) and flow angle deviation (b)

mass-averaged coefficient. Its loss components are reported in Tab. 4.7 only for the 30%C_{ax} case because of deeper meaning for the evaluation of the performance of the cascade. The pitch-wise mass-averaged loss coefficient measured at midspan coincides with the profile loss component. Then, by performing two different integrations (from midspan to tip and from midspan to hub), the secondary loss coefficients of the two half channels are retrieved by subtracting the profile and inlet boundary layers loss (1.45%). The full-span secondary loss coefficient was computed as the average of those of the two semi-channels and, by adding the profile loss, the overall loss coefficient can be retrieved. Results demonstrate a beneficial effect of the presence of the fillet that accounts for a 30% reduction on secondary losses with respect to the tip side. At midspan, the thin TE joined together the marked two dimensional behaviour of the flow-field guarantees a quite limited contribution (2.31%).

Loss component	ζ [%]
Profile	2.31
Secondary - fillet side	2.42
Secondary - tip side	3.46
Secondary - full span	2.94
Overall secondary	5.25

Table 4.7: Solid blade cascade loss components

4.6.2 Cooling system characterization

As mentioned previously (Sec. 4.2), the coolant mass-flow was measured by means of an orifice plate. Further downstream, the cooling flow passed through an electrical heater to enter, immediately after, the feeding volume at the base of the cooled blade. In this location, the coolant total pressure P_{0c} and total temperature T_{0c} were measured by a series of wall pressure taps and thermocouples.
A model equipped with a rack of static pressure taps in correspondence of the holes exit sections was used to retrieve the local static exit pressure $P_{\infty,hole}$. Because of space constraints, anyway, only six locations over ten have been measured. In order to retrieve the complete set of local data, numerical simulations performed by Ravelli [64] have been used: a non-cooled blade case was run on Fluent v12.14 (Realizable k-ϵ turbulence model with advanced wall treatment function and second order accuracy) at similar inlet conditions and the static pressure distribution at the location of the holes exit sections was extracted. The latter was then used to scale the measured $P_{\infty,hole}$ distribution and to obtain the missing data. By means of the coolant total pressure and static exit pressure, a global discharge coefficient Cd of the holes has been computed which is defined in Eq. 4.4 as the ratio between the measured coolant mass-flow divided by the sum of the isentropic mass-flows of the ten holes.

$$Cd = \frac{\dot{m}_c}{\sum \dot{m}_{c,s}} \tag{4.4}$$

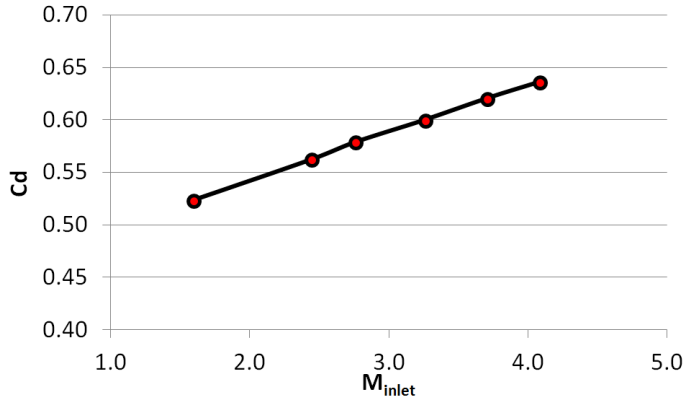

Figure 4.18: Global discharge coefficients (Cd) versus the inlet loss-free blowing ratio (M_{inlet})

The measured discharge coefficients are shown in Fig. 4.18 with respect to the inlet loss-free blowing ratio. As expected, the relation between the two parameters is monotonously growing: at constant main-stream conditions, an increasing in terms of M_{inlet} directly implies a higher pressure in the feeding volume which produces in turns an enhanced ejection from the holes. The distribution will necessarily assume, at some point, a typical asymptotic behaviour towards the value Cd would assume when chocked conditions are reached on every hole.
The computation of local parameters such as the mass-flux (BR) and momentum-flux (I) ratios requires the knowledge of local free-stream conditions (density ρ_∞ and velocity V_∞) and of how the global coolant mass-flow is distributed among the ten holes. While the first quantities can be easily derived from the inlet conditions and from the distribution of $P_{\infty,hole}$, the second one cannot be measured in the actual configuration since experimentally it was only possible to provide a global value for Cd. To overcome this difficulty, the redistribution of the mass-flow over the ten holes was retrieved by Ravelli, by simulating the cooled model. Results are presented for every hole in Tab. 4.8 as the ratio of the ejected mass-flow over the global one.

Hole	$\dot{m}_{c,hole}/\dot{m}_c$ [%]
1	10.482
2	10.54
3	10.702
4	10.564
5	10.428
6	10.203
7	9.901
8	9.502
9	9.059
10	8.62

Table 4.8: Distribution of the coolant mass-flow over the ten holes as computed by Ravelli [64]

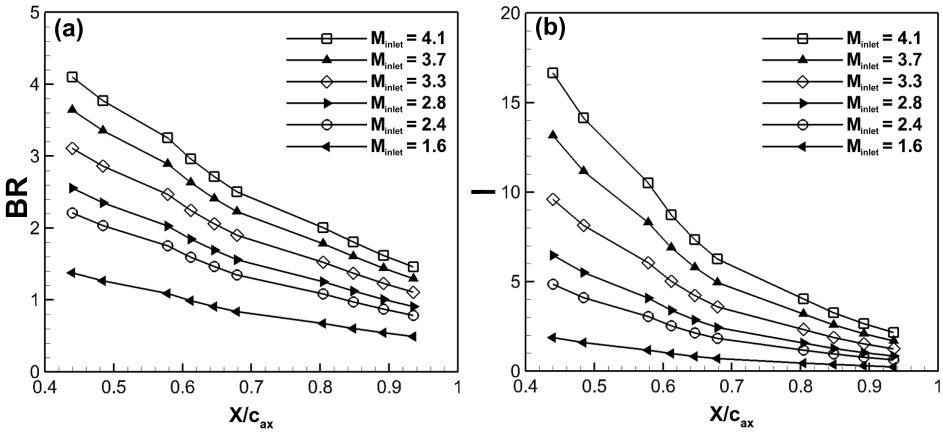

Figure 4.19: Local mass-flux and momentum-flux ratios at different injection conditions (M_{inlet})

The local discharge coefficient and local coolant Mach number were computed as $Ma_{c,hole} = Ma_{cs,hole} \cdot Cd_{hole}$. By means of the coolant total temperature T_{0c}, the local coolant static temperature and velocities were then calculated as well as the coolant density. Finally, the local mass-flux ratio and momentum flux ratio could be computed, according to the definitions given in Eq. 2.6 and Eq. 2.7 respectively. Fig. 4.19 ((a) and (b)) reports the evolution of BR and I over the holes exit locations for several injection conditions (M_{inlet} ranging from 1.6 to 4.1).

4.6.3 Cooled cascade

Aerodynamic measurements have been performed downstream the cascade when coolant ejection was taking place. To better visualize the effect of film-cooling on the aerodynamic field, the measurement plane was set at $8\%C_{ax}$ downstream the trailing edge and only in the semi-channel of the cooled endwall (filleted one). The tunnel was operated at an isentropic downstream Mach number Ma_{2s} equal to 0.3 while the cooling rate was varied between $M_{inlet} = 1.6$ and $M_{inlet} = 4$. Fig. 4.20 reports the downstream loss distribution for four different injection conditions while Fig. 4.21 presents the stream-wise vorticity and secondary velocity distributions along the measurement plane. The filleted half-channel results for the non-cooled case are also provided for comparison.

According to the maps shown in this part, injection seems to play a really marginal role on the configuration of secondary flows. By comparing the non-cooled case with all the cooled ones, no major difference in terms of shape, location and intensity of secondary structures can be appreciated neither in the loss distribution nor in the secondary vorticity plots. This result must be related to the extremely tangential configuration of the cooling holes which allowed to always confine the jets in the boundary layer of the blade platform. A confirmation of this deduction can be found in fact in the reduction of losses right next to the endwall (Fig. 4.20 between Y/g=1 and Y/g=1.5) and in the related enhancement of the cross-flow in the secondary velocities distribution (Fig. 4.21 between Y/g=1 and Y/g=1.5):

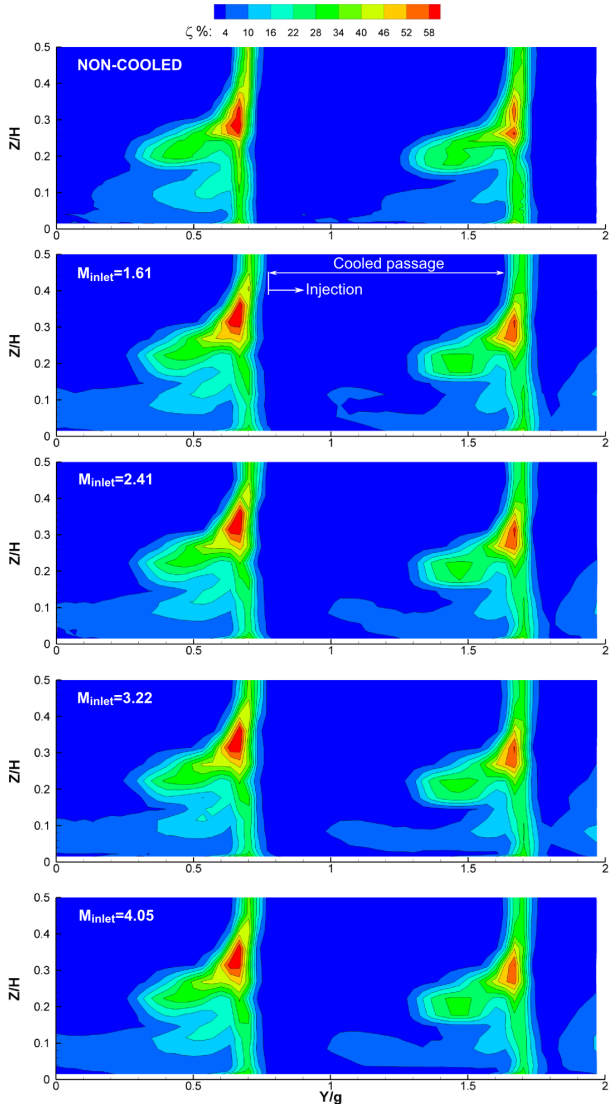

Figure 4.20: Kinetic energy loss coefficient distribution in the filleted semi-channel at $30\%C_{ax}$ for different injection conditions ($M_{inlet} = 0 - 1.61 - 2.41 - 3.22 - 4.05$)

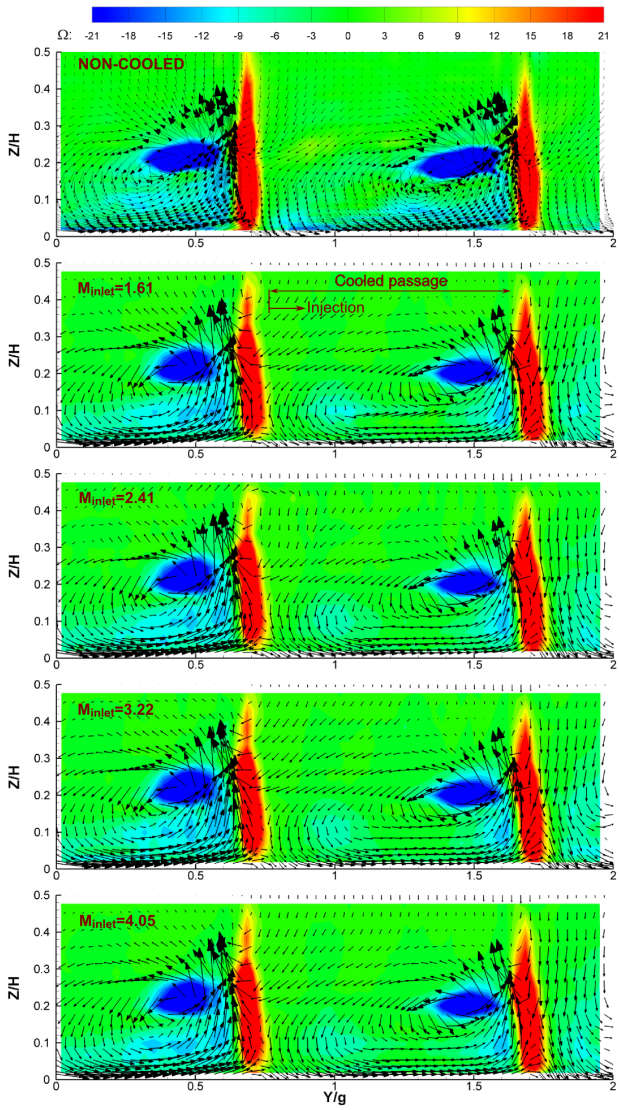

Figure 4.21: Non-dimensional stream-wise vorticity $\Omega_s C/U_1$ and secondary velocity vectors in the filleted semi-channel at $30\%C_{ax}$ for different injection conditions ($M_{inlet} = 0 - 1.61 - 2.41 - 3.22 - 4.05$)

the ejected coolant remains attached to the endwall, energizing the lower momentum boundary layer and therefore reducing the kinetic energy loss in that region.
Anyway, differences keep so small that the pitch-wise mass-averaged loss coefficient (Fig. 4.22-a) and flow angle (Fig. 4.22-b) distributions do not show any evident effect related to injection: the computation of the pitch-wise-span-wise mass-averaged loss coefficient is meaningless since it will provide differences as high as the uncertainty.

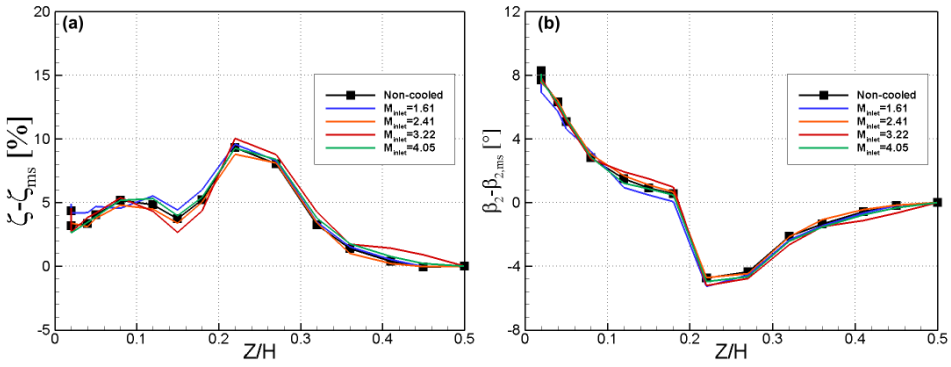

Figure 4.22: Pitch-wise mass-averaged loss coefficient (a) and flow angle deviation (b) for different injection conditions ($M_{inlet} = 0 - 1.61 - 2.41 - 3.22 - 4.05$)

4.7 Thermal measurements

The endwall adiabatic effectiveness η_{aw} has been retrieved by means of TLCs measurements of the endwall surface temperature. The definition used herein for η_{aw} was derived from the one given in Eq. 2.3 to take into account the different temperature levels between main-stream, wall and coolant: since the latter is warmer than the main flow and the surface, a more convenient expression was adopted which is reported in Eq. 4.5. Hallcrest BM/R25C10WC17-10 liquid crystals have been sprayed on the

target surface which has been previously covered with a black backing paint layer to enhance the contrast. Two white-light sources (150 [W]) provide the primary illumination to the test-section by means of fiber-optics while images have been acquired by means of a CCD 767x573 camera. The calibration of the compound has been performed in-situ, applying exactly the procedure outlined in Sec. 3.2.3.

$$\eta_{aw} = \frac{T_w - T_{0\infty}}{T_{aw} - T_{0\infty}} \tag{4.5}$$

Fig. 4.23 reports the adiabatic effectiveness distribution of the target surface for four different injection rates, ranging from $M_{inlet} = 1.61$ up to $M_{inlet} = 4.05$. In the first condition (Fig. 4.23-a), each group of holes produces an isolate, independent trace on the endwall: even though the momentum is high enough to reach almost the centre of the channel, the lateral spreading is still too low to provide a good coverage of the surface. By enhancing the ejection up to $M_{inlet} = 2.41$, the coverage as well as the penetration markedly improve: the traces of the different jets join already next to the pressure side with the tendency to widen in the middle of the blade passage. Jets, in general, seem to follow the direction imposed by the holes which suggests that the coolant momentum is higher than the one of the main-flow in the neighbourhoods, confirming again that injection takes place completely in the endwall boundary layer as concluded in Sec. 4.6.3. In condition (c) it can be appreciated how the trace of the central group of holes, while penetrating more into the channel, tends also to drift from their original direction and to follow the strong cross-flow generated by the blade pressure field. When approaching the adjacent blade, some coolant is turned directly onto the SS, providing therefore the beneficial effect of augmenting the protection of that area. At maximum injection rate (Fig. 4.23-d), the latter phenomenon is weaker than in the previous case since the higher momentum directly drives the jets towards the exit of the channel. In any case, the central zone of the blade passage is characterized by a much higher protection.

In conclusion, it should be noticed that each hole provides a well attached jet, also at the highest injection rate. This remarkable characteristic of

the present design must be addressed to the very small inclination of the holes from the surface (Tab. 4.3), which strongly enhances the resistance to separation as well as the protection performance.
To better visualize which is the effect on the coverage of a certain ejection rate, data have been area averaged. The evolution of the normalized adiabatic effectiveness is shown in Fig. 4.24 with respect to M_{inlet}, from which it can actually be deduced that a limit to the injection increasing exists: the distribution tends in fact to an asymptote that would be reached as soon as all the holes would be chocked.

4.8 Scaling of results to engine conditions

In the present chapter some comments are made and some conclusions are taken on how the experimental results can be extended to the real flow conditions. Engine data have been provided by the company as the results of in-house simulations. The main-stream (at blade mid-height) and coolant global conditions have been given together with the local flow conditions and film-cooling parameters at the discharge section of each hole.
Moreover, it has to be mentioned that a new repartition of the coolant mass-flow was also made available, which was used to compare the one computed by Ravelli [64] and presented in Sec. 4.6.2.
Even though engine data are not reported because of a matter of confidentiality, the best matching wind tunnel operative condition is herein pointed out while a graphical comparison between the different coolant repartitions is in the end presented.

Scaling the measurements at the conditions of the real machine, nominally corresponds to the computation of the global cooling parameters (MFR and M_{inlet}) that the tunnel would exhibit when operated at engine-like pressure and temperature levels as well as at the same local injection conditions (I and/or BR). In the frame of the present work, a procedure was adopted which is iteratively changing the coolant total pressure P_{0c} to obtain the best possible matching in terms of inlet loss-free blowing ratio.

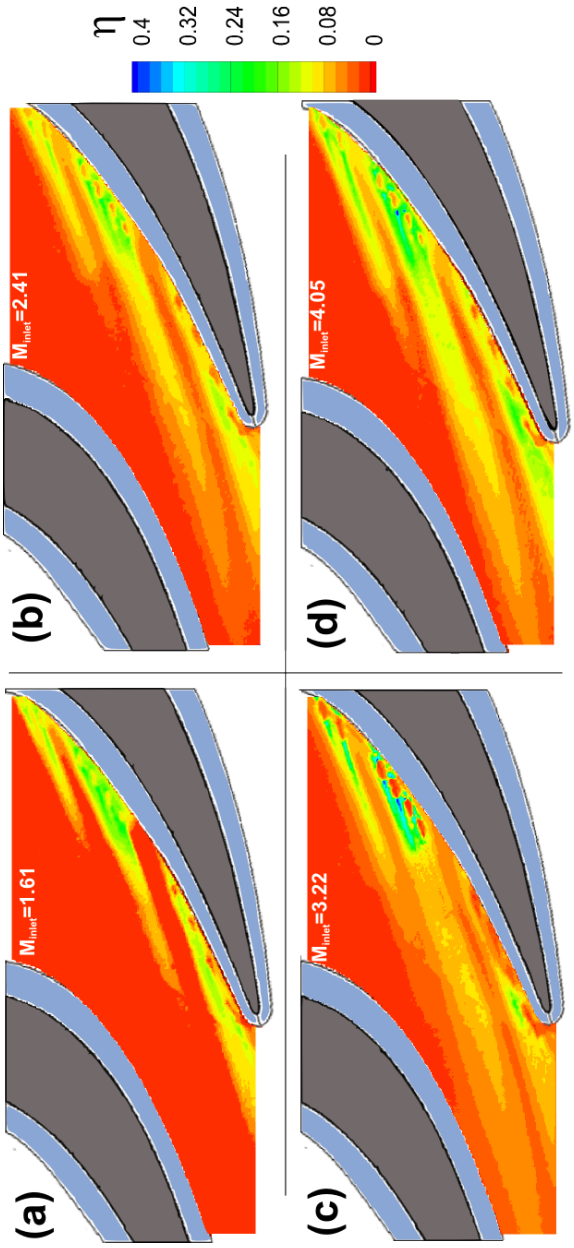

Figure 4.23: Endwall adiabatic effectiveness distribution for different injection conditions ($M_{inlet} = 1.61 - 2.41 - 3.22 - 4.05$)

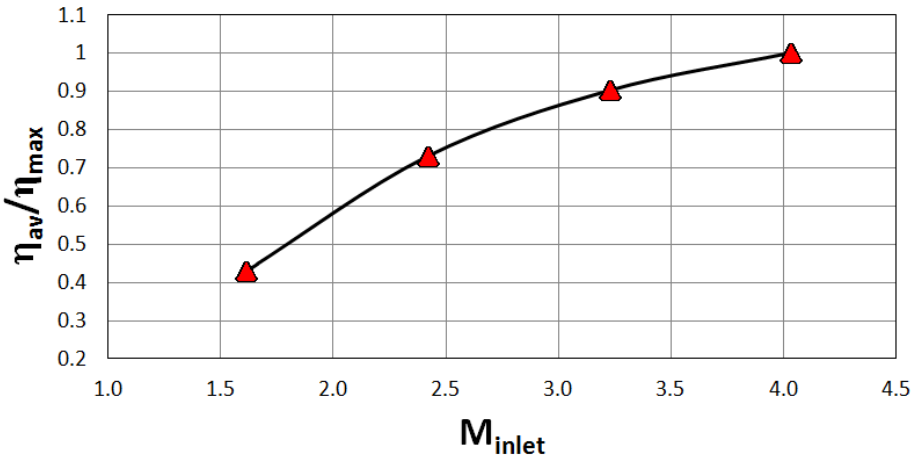

Figure 4.24: Normalized area-averaged adiabatic effectiveness versus the inlet loss free blowing ratio

The steps of the calculations are summarized in the following:

1. Simulations defined the main-stream conditions at the exit sections of the holes.

2. A coolant total pressure P_{0c} value is imposed in the feeding volume: the inlet loss-free blowing ratio M_{inlet} could be immediately retrieved.

3. The measured discharge coefficient evolution with respect to M_{inlet} (Fig. 4.18) allows to determine a global Cd for the actual injection condition.

4. By imposing an isentropic expansion from the coolant total pressure P_{0c} to the local static exit pressure $P_{\infty,hole}$, the local isentropic mass-flow $\dot{m}_{cs,hole}$ for each hole can be computed. The global coolant mass-flow is then retrieved as $\dot{m}_c = Cd \cdot \sum \dot{m}_{cs,hole}$.

5. The global coolant mass-flow is then distributed over the ten holes by using the two available redistribution sets, the one from Ravelli and the one from Ansaldo.

6. Finally the local injection conditions can be computed. P_{0c} is then iteratively varied at step 2 until the best matching for I is found.

The wind-tunnel condition that best represents the real engine behaviour is summarized in Tab. 4.9: it corresponds to a global inlet loss-free blowing ratio $M_{inlet} = 2.14$ and a mass-flow ratio $MFR = 0.05$. The global discharge coefficient is instead equal to $Cd = 0.541$. The local momentum-flux ratio for the two adopted redistributions (Ravelli (red line) and Ansaldo (blu line)) is presented in Fig. 4.25 together with the engine data (black line).

M_{inlet}	2.14
MFR	0.05
Cd	0.541

Table 4.9: Wind tunnel best representative conditions of the real engine behaviour

Among the set of tested configurations, the aerodynamic and thermal results that best represent the real engine behaviour are those obtained for $M_{inlet} = 2.41$, which in fact closely resembles the engine data provided by Ansaldo Energia. In these conditions, a marked matching is found in correspondence of the every hole except for the first two ones which in reality were fed by a dedicated plenum, as mentioned previously in Sec. 4.2.
In the end it has to be mentioned that, at real operating conditions, the secondary structures will present some differences with respect to the present case just because of the effect of a higher Mach number. As demonstrated by Perdichizzi [58], secondary flow regions are expected to move towards the hub and the tip at a higher flow regime while the overturning angle at the wall should reduce as a weaker cross-flow is also expected.

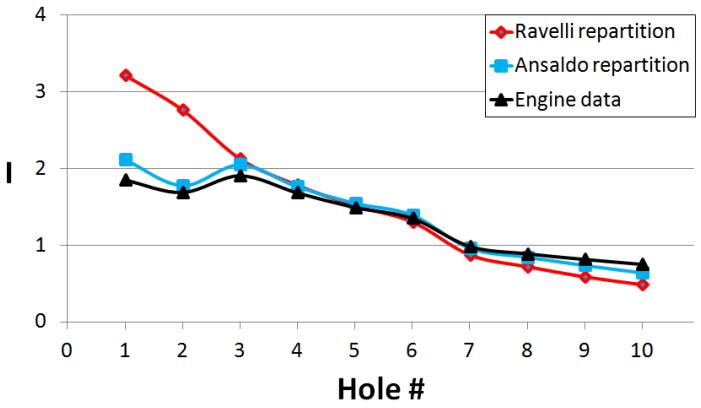

Figure 4.25: Momentum-flux values for each hole of the best matching wind-tunnel condition. The Ravelli and the Ansaldo computed redistributions of the coolant mass-flow are presented against the real engine results

4.9 Uncertainty analysis

The measurements uncertainty analysis presented herein was performed by means of the error propagation theory. The uncertainty related to a derived quantity is necessarily dependent on the one of the independent variables which participate to its computation. Given therefore a certain measured quantity A, function of x, y and z, an estimation of its standard deviation δA can be provided, basing on δx, δy and δz by means of Eq. 4.6.

$$\delta A = \sqrt{\left(\frac{\partial A}{\partial x}dx\right)^2 + \left(\frac{\partial A}{\partial y}dy\right)^2 + \left(\frac{\partial A}{\partial z}dz\right)^2 + \epsilon^2} \tag{4.6}$$

In the latter equation, ϵ expresses any other contribution to the propagation of errors which is not tackled by δx, δy and δz, such as the quality of a curve fitting, if used. The deviation of A retrieved by the latter procedure is referred to a 65% confidence interval. By multiplying δA by a factor 2 (2σ), then the confidence interval is extended up to the 95%, meaning that

95 occurrences over 100 will show a value in the range $A - \delta A \div A + \delta A$. Uncertainty values quoted in the present chapter are all referred to the 95% confidence interval.

Pressure and temperature data from sensors have been all sampled by an HP 3852A D.A.C.U. 12bit acquisition system. A Scanivalve mechanical pressure scanner equipped with a 5 [psi] differential transducer has been used to acquired wall static pressures (upstream and downstream the cascade) and the inlet total pressure whose estimated uncertainties are equal to $\pm$ 5.5 [Pa] and $\pm$ 10 [Pa] respectively. The error on the inlet loss-free blowing ratio M_{inlet} was computed by taking into account the uncertainty of the inlet total and static pressures as well as of the pressure transducers connected to the coolant feeding system. In the worst condition ($M_{inlet} = 4.05$) δM_{inlet} was found to be equal to $\pm$ 0.16. Velocity measurements by LDV technique were performed by acquiring 20000 burst signals per measurement point, which guaranteed an uncertainty of the order of $\pm$0.1% of the mean velocity value. Static and total pressure measurements performed by 5-hole pneumatic pressure probe were both characterized by an uncertainty equal to $\pm$0.15% of the dynamic head, which produces an uncertainty on the computed loss coefficient of $\pm$0.3% for $\zeta = 3\%$ and $\pm$0.2% when ζ is equal to 30 %. The error related to the measured flow angle was found to be equal to $\pm$1 [°]. Film-cooling effectiveness values computed from TLCs wall temperature distributions exhibited an uncertainty which ranges from $\pm$5% at $\eta_{aw} = 0.5$ up to $\pm$15% when η_{aw} is equal to 0.1.

4.10 Summary of the measurement campaign

The experimental campaign described previously dealt with the identification of the effect that the endwall cooling system of a high pressure blade induces on its aerodynamic and thermal performance, with a particular attention paid to the study of the interactions between coolant and secondary flows. The definition of the geometry of the model was discussed in the first section. The closest blade profile to the platform was selected to

build a cylindrical model: the priority has been to produce a pressure field on the endwall that was as most representative as possible of the real condition. For the same reason, the blade-endwall fillet that was equipping the original geometry was also kept. The endwall cooling system was designed preserving both, the l/D ratio of holes as well as their relative position with respect to the fillet. The model was tested in a seven blades linear cascade configuration. An open loop suction-type wind tunnel was designed to host the cascade: it consisted of a long inlet duct which connects the inlet section (equipped with a filtering element) to the leading edges plane of the cascade. Downstream, moving tail-boards have been foreseen to adjust the periodicity of the flow. The test section, entirely made up of Plexiglass to guarantee a full optical access, was then connected to an industrial fan by means of a diffuser.

The wind tunnel inlet flow was firstly characterized. The homogeneity of the flow was checked by measuring the inlet total pressure and flow angle along the tangential direction. The boundary layer was investigated by traversing a Pitot probe in the span-wise direction: the computation of the integral parameters as well as the shape of the velocity gradient suggested the presence of a fully developed turbulent boundary layer. The inlet free-stream turbulence intensity was then measured by means of hot-wire anemometry: for a discharge isentropic Mach number of 0.3, Tu% in the middle of the inlet duct was found to be approximately equal to 1%. The periodicity of the flow-field was verified by means of a rack of 34 wall static pressure taps distributed over 4 pitches and placed at the 30% of the axial chord downstream the trailing edge plane. By acting on the movable tail-boards, the wall static pressure was adjusted until a highdegree of homogeneity was achieved over the investigated channels. In the end, the blade loading at midspan was assessed through LDV measurements.

Aerodynamic measurements have been performed at $Ma_{2s} = 0.3$ firstly without coolant injection (non-cooled cascade). A 5-hole pressure probe was traversed along two traversing planes placed at 8% and 30% of the axial chord downstream the trailing edge. Kinetic energy loss, vorticity and

secondary velocity distributions have been all retrieved. They showed quite a typical secondary flows structure: well visible were in fact the two counter-rotating passage vortexes which dominated the secondary loss generation. The high turning of the cascade moved them towards the mid height of the blade where a thin wake was recognized. Substantial differences between the filleted hub blade and the "straight" tip were found: no corner vortex was developing at the hub where only the loss core and vorticity area related to the passage vortex were visible. The tip region presented instead a more complicated pattern: two well visible co-rotating areas were separated by a pair of counter rotating structures. In order to enhance the interpretation of such a distribution, oil visualizations have been performed. The suction side and endwall streak-lines clearly showed that no corner vortex is generated as the fillet lifted up the boundary layer directly towards the passage vortex. The separation line of the suction side leg of the horseshoe vortex was visible in the first half of the suction surface, to vanish afterward as it was dissipated by the stronger counter rotating passage vortex. In the tip region, the separation and reattachment lines of the corner vortex were instead clearly discernible on both, the blade surface and the endwall. The horseshoe vortex trace was, in this area, well visible: it was located over the passage vortex and it was able to reach the trailing edge. No evidence of the generation of the two vorticity areas (one co-rotating with the passage vortex, one counter-rotating) could be found in the visualizations: a possible explanation was provided on the basis of the model of Wang et al. [78] even though some more experimental efforts should be spent to clarify the phenomenon. Pitch-wise averaged loss coefficient and flow angle confirmed the absence of the corner vortex: a high overturning was present at the filleted hub while a reduced passage-vortex-related peak at about the 20% of the span was found. The beneficial effect of the presence of the fillet is in contrast with what found in literature even though the comparison is weak: none of the published geometries resembled the one adopted in the present project. Further downstream ($30\%C_{ax}$), because of the mechanism of mixing, the distribution along the blade span looks more flat and homogeneous. In the latter case, the span-wise-pitch-wise mass-averaged secondary loss was found to be responsible for the generation of the 56% of

the overall secondary loss.

The cooling system was characterized for an inlet loss-free blowing ratio spanning from $M_{inlet} = 1.61$ up to $M_{inlet} = 4.05$. The wall static pressure at the exit sections of the holes was assessed by means of an instrumented blade and aided by CFD simulations. The overall coolant mass-flow provided to the whole rack of holes was measured with an orifice plate placed in-line in the coolant feeding piping. The latter, together with the coolant total pressure (measured in a settling volume placed right underneath the cooled blade), allowed to compute a global discharge coefficient at every injection conditions. Using the coolant mass-flow repartition computed by CFD simulations run by Ravelli [64] and the measured coolant total temperature, local injection parameters such as mass-flux ratio (or blowing ratio) and momentum-flux ratio have been computed for each hole.

Aerodynamic measurements with injection have been performed only in the filleted semi-channel on whose endwall film-cooling holes were present. Loss and vorticity distributions only showed a really weak interaction of the coolant flow with secondary structures: intensity and locations of cores did not vary, not even at the highest injection rate.

The wall adiabatic effectiveness was assessed by recording the wall temperature distribution by means of thermochromic liquid crystals calibrated in-situ. The coolant temperature was increased over the main-stream one by means of an electrical heater located upstream the feeding volume. At every injection condition the cooling flow did not detach from the endwall surface, providing a wider and more effective protection for every enhancement of the injection rate. Because of the highly tangential geometry of the holes with respect to the surface, the cooling flow remained entrained in the endwall boundary layer, resulting to be weakly or completely not affected by secondary structures. Only in one case, at $M_{inlet} = 3.22$, cooling jets were forced to drift by the pressure field from the direction imposed by the holes geometry. In this case, the cooling flow skimed the rear part of the suction side of the adjacent blade.

In-house simulations performed by Ansaldo Energia on the real machine have been made available for comparisons with experiments. In order to perform a meaningful correlation between engine data and wind tunnel measurements, the latter had to be scaled coherently: the coolant total pressure was iteratively changed until the best matching in terms of momentum-flux ratio over the holes was found between wind-tunnel and real data. The wind tunnel most representative condition of the engine behaviour was found to be equal to $M_{inlet} = 2.14$. Since the company also provided a different distribution of the coolant mass-flow among the ten holes, the Ansaldo repartition was compared with the one computed by Ravelli and a good agreement was found especially for the second and third groups of holes.

Chapter 5

Aero-thermal performance of a film-cooled transonic guide vane

5.1 Motivation and targets

[...] AGARD Work Group 18, headed by Prof. Fottner, led to the conclusion that further cascades test cases should provide more information [...] for comparison with numerous Navier-Stokes numerical codes developed over the last years. - (TN-174 - September, 1990)

The quotation from the VKI Technical Note TN-174, perfectly summarizes what was introduced previously in Chapter 1 and it also justifies the efforts done at the von Karman Institute in the frame of the production of experimental test cases for Turbomachinery codes validation. Among the several activities carried out by the Institute on the topic of codes validation, two projects have been started in 1990 whose the results were published in three main publications: the Technical Note TN-174 [6], the journal paper [5] and the contribution presented during the Lecture Series LS 1994-06 [4]. The two of them were based on the LS-89 geometry and its film-cooled version, the LS-94 (Fig. 5.1): the non-cooled blade was

described mainly in terms of wall pressure and heat transfer distribution, downstream loss and angles profiles while, for the cooled airfoil, only the wall heat transfer distributions were investigated.

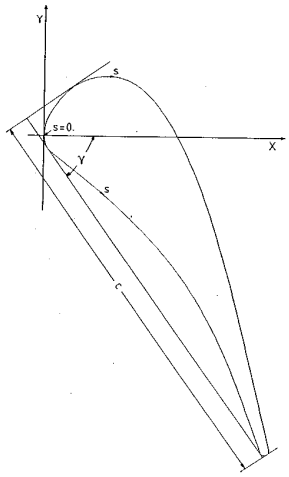

Figure 5.1: LS-89/94 profile

The latter works rapidly became among the most known experimental test cases worldwide and the two last papers dealing with codes validation and based on these geometries were published in 2010 [51] and 2011 [75]. If, on one hand, it means that the quality of those publications was so high that they are still in use after more than twenty years, on the other hand it leads to an another important conclusion: the availability of experimental test cases for Turbomachinery codes validation is still a critical issue.
The present campaign configures itself as a follow up of what was previously done at the von Karman Institute in the frame of experimental test cases for Turbomachinery code validation and its final target is to complement the two previously cited publications in order to provide the Japanese "Central Research Institute of Electric Power Industry" with a robust and complete experimental test case for validation purposes.

Given that the previous works were mainly focused on the characterization of the non-cooled blade, the present activity aims to investigate the film-cooled cascade LS-94 (Fig. 5.5) in terms of inlet free stream turbulence, outlet pressure wakes and flow angle and convective heat transfer distributions.

5.2 Isentropic Compression Tube Tunnel: CT-2

The tests were carried out in the isentropic light weight piston compression tube facility CT-2. It is a short duration wind tunnel that is able to operate in full similarity with real engine conditions in terms of Mach number, Reynolds number and main stream-to-coolant temperature ratio.
As presented in Fig. 5.2, compressed air is injected in the cylinder where the piston is enclosed. The piston, by moving forward under the effect of the pressure of the injected air, compresses the column of air contained in the cylinder. When the requested conditions in terms of pressure and temperature are reached, the fast shutter valve is opened and the heated-pressurised air is made free to flow through the test section. The testing flow is finally discharged in a dump tank.
By acting on the timing of shutter valve and on the pressure that can be set in the dump tank, the Mach and the Reynolds number can be varied independently while steady state free stream conditions are maintained up to 0.5 [s].

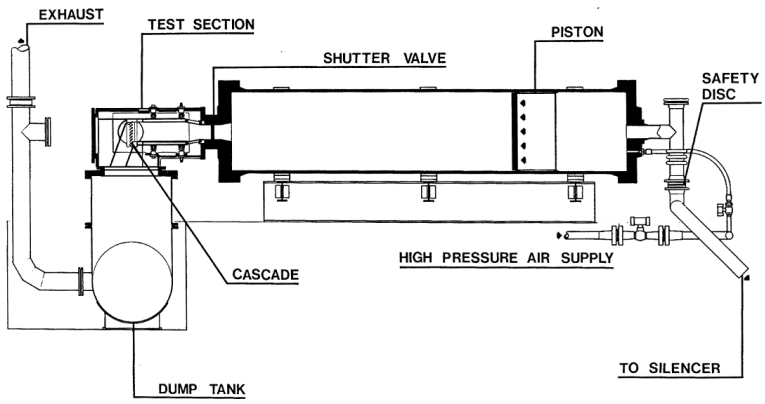

Figure 5.2: CT-2 compression tube facility

5.3 Test Section Geometry

5.3.1 Blade profile and cascade parameters

The LS-94 is a transonic film cooled turbine vane. The base profile, the LS-89 (Fig. 5.1), was designed at VKI for pure research applications. The test model consists of a five blade linear cascade whose geometrical dimensions are listed in Table 5.1. The related nomenclature is reported in Fig. 5.3.

Parameter	**Symbol**	**Value**
Chord [mm]	C	67.65
Axial chord [mm]	C_{ax}	36.985
Stagger angle [deg]	γ	55
Throat [mm]	o	14.93
Pitch [mm]	g	57.5
Blade height [mm]	H	100
Trailing edge radius [mm]	r_{TE}	0.71

Table 5.1: Cascade geometrical parameters: description, symbols and values

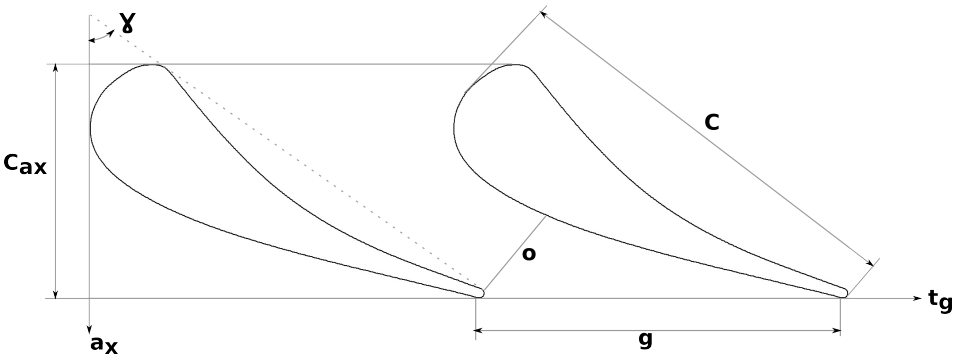

Figure 5.3: Cascade geometrical parameters: nomenclature

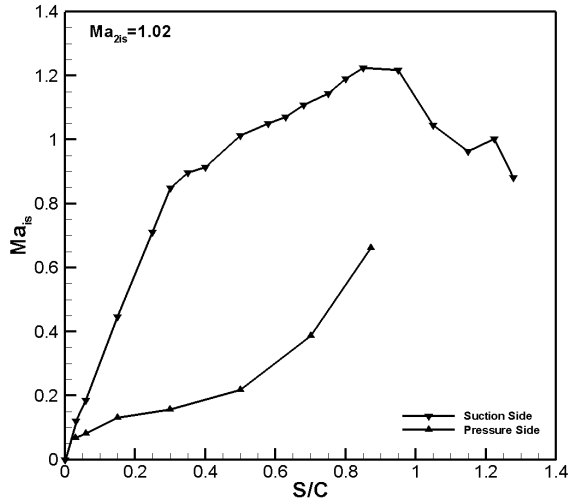

Figure 5.4: Measured isentropic Mach number distribution of the profile at $M_{2is} = 1.02$ - Arts et al. [6]

In this configuration, the wall Mach number distribution for an isentropic discharge Mach number (Ma_{2is}) of 1.02 is presented in Fig. 5.4. In the first part of the suction side the flow is subjected to a rapid and constant acceleration up to S/C=0.3 where a short plateau is present. It is then reaccelerated with a smaller and almost constant rate up to the maximum velocity point around S/C=0.9, followed by an evident diffusion up to the trailing edge. The pressure side distribution provides a smooth and continuous acceleration without any discontinuity in the velocity profile.

5.3.2 Cooling system configuration

Two rows of staggered holes are present on both, the suction and the pressure sides. They are fed separately by means of two different feeding chambers. Table 5.2 reports the geometrical characteristics of the cooling system with respect to the frame of reference of Fig. 5.5, where a cross section of the LS-94 blade is also presented.

	Suction Side		**Pressure Side**	
Diameter [mm]	0.5		0.5	
Pitch [mm]	1.5		1.5	
Coordinates [mm]	row 1 X=2.52 Y=15.7	row 2 X=4.05 Y=19.95	row 1 X=13.96 Y=2.19	row 2 X=16.59 Y=2.9
Angles [°]	row 1 35 from surface	row 2 35 from surface	row 1 35 from surface	row 2 // to row 1
# of holes	row 1 33	row 2 32	row 1 33	row 2 32

Table 5.2: Cooling system characteristics

Coolant was injected at controlled temperature by feeding the suction and the pressure sides at different times. The coolant is provided to the feeding chambers by means of a piping system equipped with a sonic orifice to exactly control the mass-flow: it was designed to be always operated in chocked conditions according to the orifice downstream pressure level. Coolant total pressure is measured right before the inlet section of the feeding chamber. On the opposite end of the blade, a second piping system was foreseen for two main purposes: to check the homogeneity of the pressure along the span of the feeding chamber and to bypass a controlled amount of flow in order to vary the blowing ratio (BR). A principle sketch is presented in Fig. 5.6.
In the following, when

5.3.3 Test section

In order to be mounted in the facility, the cascade was enclosed within two endwalls, assuring an univocal positioning of the model with respect to the frame of reference of CT-2.
The first endwall (see Fig. 5.7 (a)) presents a rack of 41 static pressure taps covering a length of more than three pitches. They will be used in

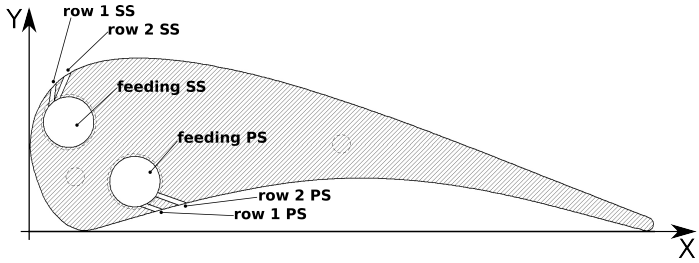

Figure 5.5: Ls-94 cross-sectional view: frame of reference for given coordinates, cooling holes and feeding chambers are all indicated

order to retrieve the wall static pressure distribution along the measuring plane. The latter was set at 43.3%C_{ax} downstream the trailing edge in the axial direction (16 [mm]). On the second endwall (Fig. 5.7 (b)) a slit in the downstream section has been foreseen to traverse a probe with its tip moving along the same measuring plane. Total inlet temperature (T_{01}), total and static inlet pressure (respectively P_{01} and P_1) of the free stream were measured by means of three different access holes as indicated in Fig. 5.7. Both endwalls were designed also with the intent of carrying "on board" the cooling feeding system (5.3.2) and to fix inlet and outlet boards. The latter components are shown in Fig. 5.8 where a three-dimensional view of the complete assembly is presented.

5.3.4 Measurements

As mentioned in the previous chapter (section 5.3.3), endwalls were designed also by taking into account the type of measurements to be performed and the position of the measuring points with respect to the cascade. Inlet free stream turbulence was characterized by hot-wire anemometry (HWA). A HW probe was fixed at 148.7%C_{ax} upstream the leading edges plane in the axial direction. Downstream total pressure wakes were measured by means of a directional pneumatic pressure probe (PP) that was traversed along the outlet measuring plane (43.3%C_{ax} downstream the

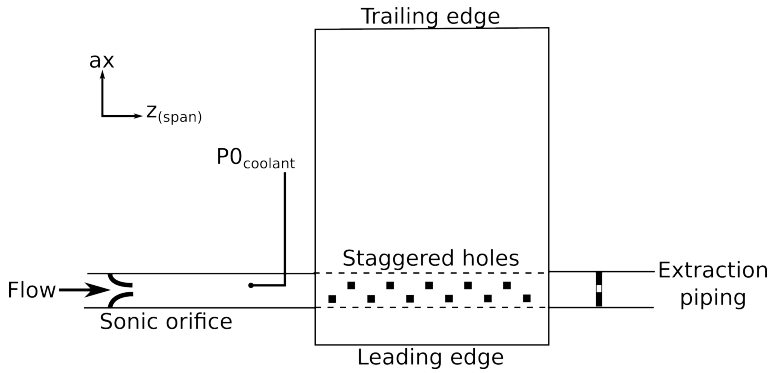

Figure 5.6: Coolant feeding system configuration

trailing edges plane) in order to completely cover the two central blade channels. Measurements were performed at midspan (50 [mm]).
Coolant total pressure P_{0c}, total temperature T_{0c} and mass-flow $\dot{m}_c$ were measured too.
Heat transfer measurement were performed along a ceramic blade surface instrumented with 42 thin-films (TF) whose coordinates are reported in appendix F.

Service measurements were performed at every experiment: inlet total and static quantities (T_{01}, P_{01} and P_1) and the static outlet pressure P_2 were always measured. The latter parameter was assessed by means of the static pressure taps rack: it was also used to evaluate the periodicity in the two central measuring blade passages (section 5.4).
Measured quantities and positions of measuring points with respect to the cascade are summarized in Table 5.3.

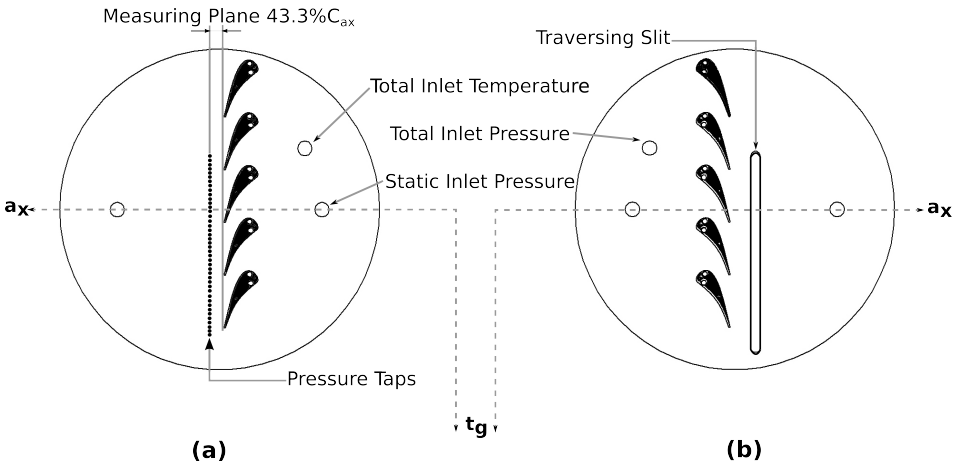

Figure 5.7: Endwalls: list of the features on respectively first (a) and second (b) endwalls

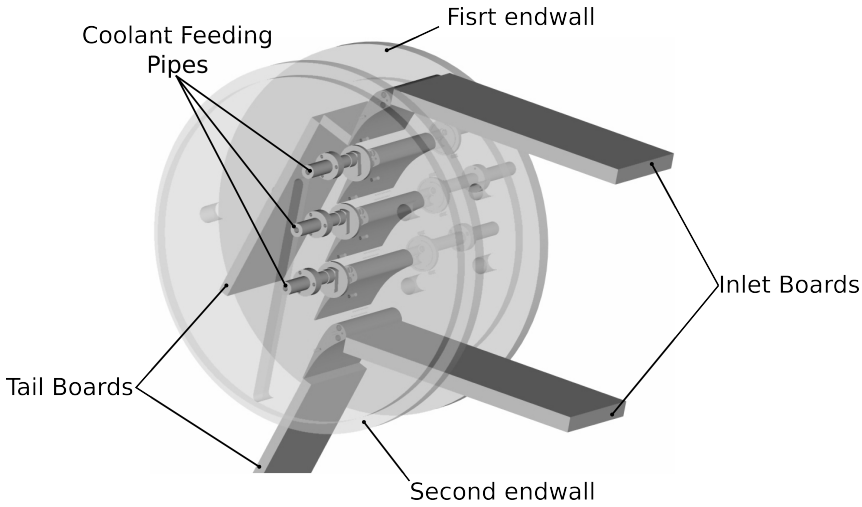

Figure 5.8: Complete assembly of the test section: coolant feeding pipes, inlet and outlet boards are all shown

Section	% C_{ax}	**Quantities**
Inlet	148.7%C_{ax} upstream leading edge	Turbulence (HW) P_{01} P_1 T_{01}
Outlet	43.3%C_{ax} downstream trailing edge	Total pressure wakes (PP) P_2
Coolant	/	P_{0c} T_{0c} $\dot{m}_c$

Table 5.3: Measured quantities and measuring positions with respect to the cascade

5.3.5 Matrix of experiments

Turbulence and aerodynamic tests were performed at a total inlet temperature $T_{01} = 340$ [K].
Hot-wire measurements were performed at $Ma_{2s} = 0.8$ and $Re_{2s} = 10^6$ for 5 different values of turbulence intensity (Tu) ranging from 1% up to 5.3%.
Downstream total pressure wakes for the non-cooled case (PP) were investigated for different isentropic downstream Mach numbers, going from high-subsonic ($Ma_{2s} = 0.7$) up to slight supersonic ($Ma_{2s} = 1.1$) regimes, in a Reynolds number range spanning from $0.5 \cdot 10^6$ up to $1.5 \cdot 10^6$.
The suction side cooling characterization (SSC) was performed at $Re_{2s} = 1.5 \cdot 10^6$ for a Ma_{2s} spanning from 0.7 up to 1.1 and at $Re_{2s} = 0.5 \cdot 10^6$ for $Ma_{2s} = 1$.
On the pressure side, the cooled configuration investigation (PSC) was done at an isentropic downstream Reynolds number ranging between $Re_{2s} = 0.5 \cdot 10^6 - 1.5 \cdot 10^6$, from a high subsonic condition ($Ma_{2s} = 0.7$) up to a supersonic one ($Ma_{2s} = 1.1$).
Heat transfer tests were performed at an inlet total temperature $T_{01} = 420$

[K] and cooling fluid at ambient and "cold "temperature. The effect of the Reynolds number was assessed only for the non-cooled case at $M_{2s} = 0.9$ with Re_{2s} spanning from 0.5 up to 1.5 million. The effect of injection was instead tested for both the suction and the pressure sides at $Re_{2s} = 1.5 \cdot 10^6$ for two different isentropic Mach numbers, $M_{2s} = 0.8$ and $M_{2s} = 1.1$ respectively. The inlet free stream turbulence intensity was set at $Tu = 5.3\%$.

	$RE_{2s} = 0.5 \cdot 10^6$	$RE_{2s} = 1 \cdot 10^6$	$RE_{2s} = 1.5 \cdot 10^6$
$Ma_{2s} = 0.7$		PP	SSC PSC
$Ma_{2s} = 0.8$	HW	HW	TF HW PSC
$Ma_{2s} = 0.85$		PP	
$Ma_{2s} = 0.9$	TF PSC	TF PP PSC	TF SSC PSC
$Ma_{2s} = 0.95$	PP	PP	PP
$Ma_{2s} = 1$	PP SSC	PP	PP SSC
$Ma_{2s} = 1.1$		PP	TF SSC PSC

Table 5.4: Matrix of experiments: (PP)-pneumatic pressure probe for downstream total pressure wakes ; (HW)-hot wire anemometry for inlet free stream turbulence ; (SSC)-suction side cooled configuration ; (PSC) -pressure side cooled configuration ; (TF)- thin-films thermometry for heat transfer measurements

5.4 Periodicity and repeatability of the experiments

The periodicity of the flow field downstream of the cascade was investigated by means of the static pressure taps placed at 43.3%C_{ax} downstream of the trailing edge. The inclination of the upper tailboard was varied from the metal angle exit (75 [°]) to the lower value of 71.5 [°], in order to obtain as periodic as possible conditions in the two central channels.
Figure 5.9 reports the isentropic downstream Mach number distribution in correspondence of the two central blade channels for three different flow regimes. Even though the distribution is slightly ascending when moving towards tap 41, the flow pattern of the two channels are absolutely repeatable, with a maximum difference of less than 3% in the middle of the channels for the three flow conditions.
The repeatability of the experiments was evaluated by performing three different tests at the same fixed conditions. Results are reported in Fig. 5.10: the maximum difference is found for test 2 to be about 1% for every measuring point.

5.5 Turbulence Characterization

Measurements were performed with and without turbulence generator, resulting in five different turbulence intensity levels. The hot-wire probe was kept fixed while the turbulence generator was moved in four different positions along the inlet channel. The grid consisted in an array of horizontal cylinders of 3 [mm] in diameter and 12 [mm] in pitch, covering the complete cross-section of the inlet duct. Hot-wire raw voltages were converted in terms of velocities by means of the procedure outlined in section 3.4 that required as inputs the inlet Mach number, density, total and static temperatures. These quantities were computed by means of data acquired by probes that naturally exhibited a really low frequency response if compared to the hot-wire's one. In order therefore to avoid the noise contamination resulting from the use of a sampling frequency much higher than the cut-off

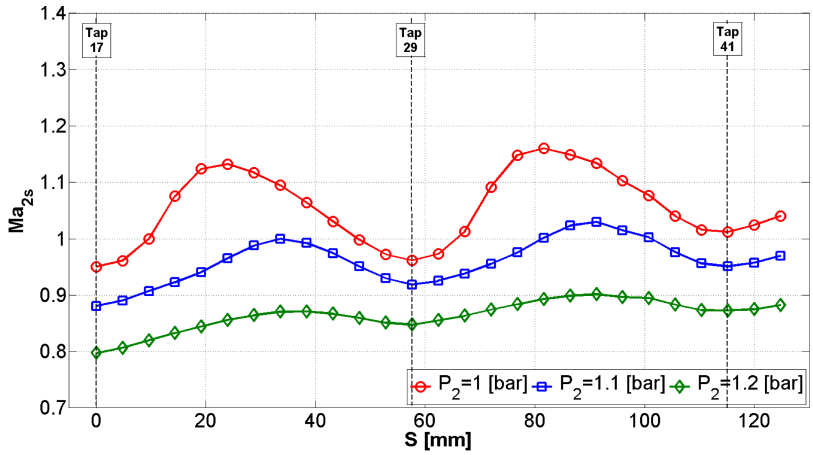

Figure 5.9: Periodicity within the two measuring channels for different downstream isentropic Mach numbers

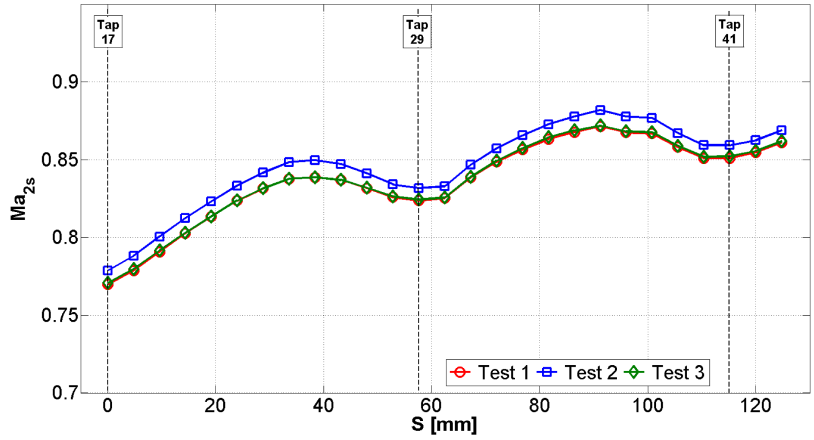

Figure 5.10: Repeatability of the experiments: downstream isentropic Mach number distribution

frequency of the probes, mean flow measurements (i.e. P_{01}, P_1 and T_{01}) underwent a linear regression procedure and the resulting regression line was used in place of the original time series. The effect of this simplification that actually works as a filter is analyzed in Appendix A.
All the tests were performed at a total inlet temperature of 340 [K] at $Ma_{2is} = 0.8$ and $Re_{2is} = 10^6$. The wire temperature was kept constant at 520 [K] (*wire's effective temperature* T_{wire} as explained in 3.4). Data were acquired during an observation time of 0.98 [s] and sampled at 65 [kHz]. Nomenclature, measuring positions and corresponding nominal turbulence intensities are shown in Fig. 5.11.

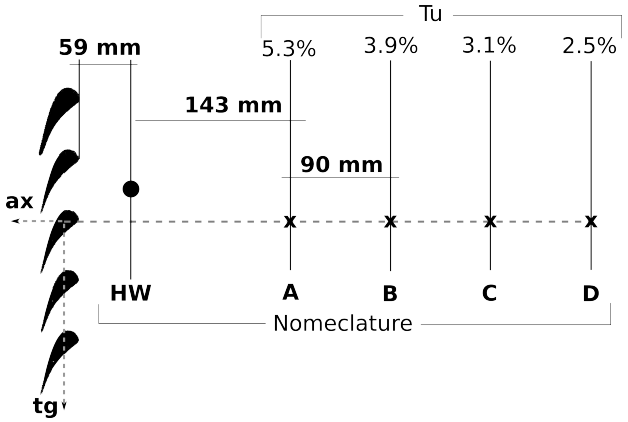

Figure 5.11: Adopted nomenclature, dimensions and nominal turbulence intensities for hot-wire turbulence measurements

5.5.1 Turbulence spectra

Fifty sub-records were extracted from the original time series, providing a random degree of overlapping to avoid any phase-locked artefact. Every sub-record was then windowed by means of an Hanning window and the spectrum computed with an FFT algorithm. Finally an ensemble average in the frequency domain was performed and the Power Spectral Density

(PSD) was computed as the square of the so obtained spectrum [11]. The hot-wire cut-off frequency was found to be approximately equal to 24 [kHz], therefore the PSD was stopped at this value. Fig. 5.12 shows the PSD for the four investigated positions along the channel length. The poor spectral resolution at low frequencies comes directly from the ensemble averaging procedure that, on the other hand, allows to greatly reduce the noise content in the high frequency range and to clearly highlight the presence of deterministic peaks. Three peaks are in fact present in the spectra at 5, 12 and 15 [kHz]: the first two of them have been already identified in [6] (even though at slightly different frequency) to be of pure acoustic nature while the third one corresponds to an harmonic of the first peak. In order to verify this deduction, a free stream turbulence spectrum is plotted against the $Tu = 4\%$ one, in Fig. 5.13: as expected, the previously identified peaks are still visible while a fourth peak at 6.7 [kHz] results to be damped by the presence of the turbulence generator itself. Spectra are decreasing as the grid is shifted further upstream. This typical behavior describes and defines the phenomenon of decay: the more space (or time) is given to the flow in the channel, the higher is the amount of energy dissipated. The latter is promoted by the viscous interactions provided by small dissipative turbulent structures that can be found at a high frequency ranges in the spectrum. The typical slopes ("-1" , "-5/3" , "-3" and "-7") characterizing the energy cascade are in fact recognized.

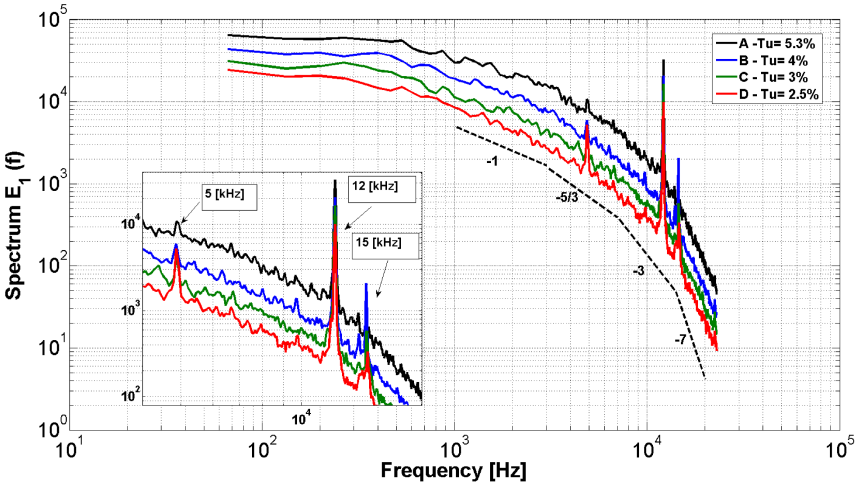

Figure 5.12: Power spectral density (PSD) evolution along the channel

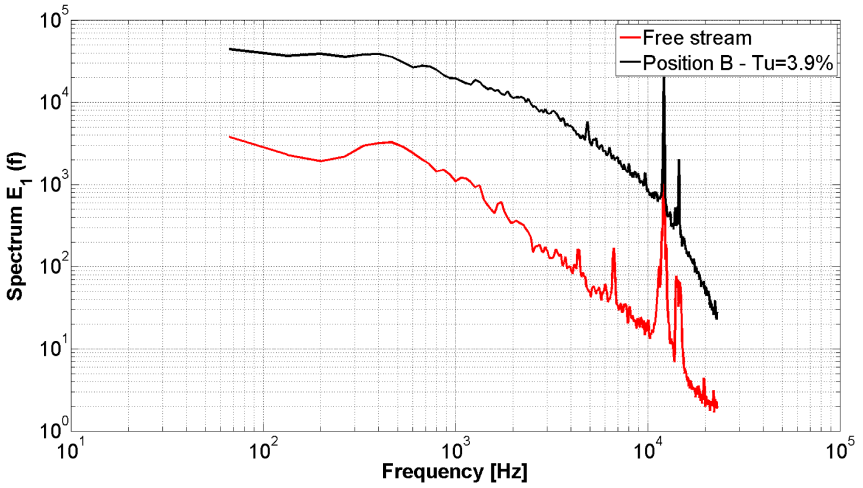

Figure 5.13: Comparison of the free stream spectrum against the grid generated turbulence spectrum for Tu= 3.9%

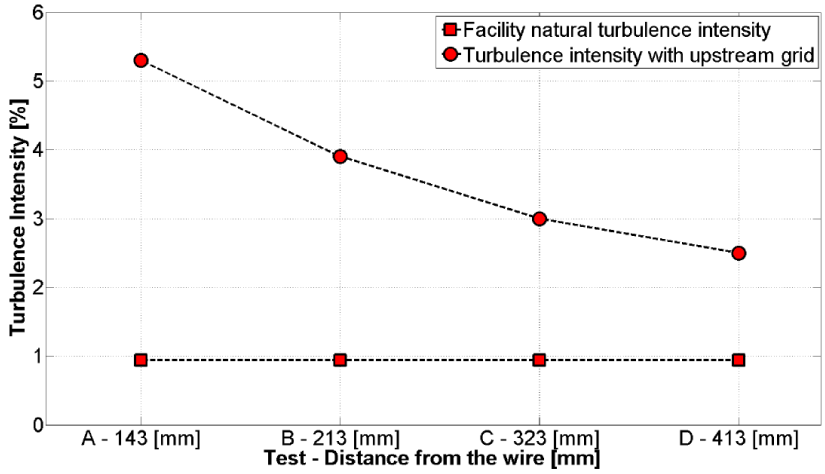

Figure 5.14: Turbulence intensity evolution along the channel for the tested configuration of the grid. Squares represent the facility natural turbulence intensity

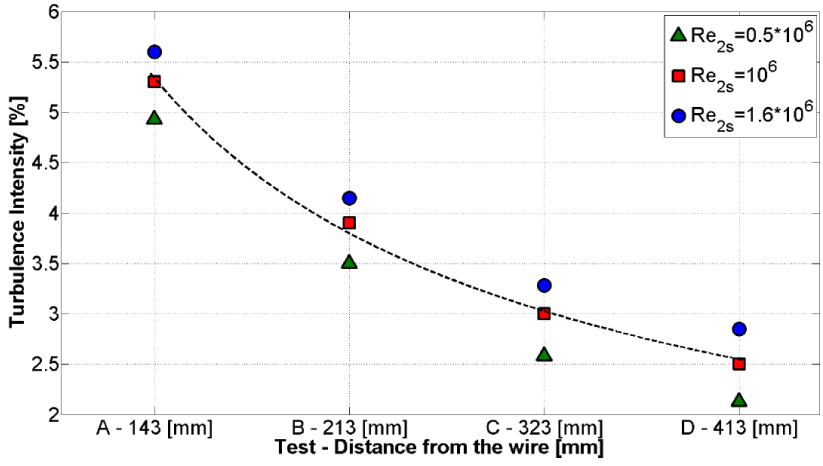

Figure 5.15: Turbulence intensity evolution along the channel for an isentropic downstream Reynolds number ranging from 0.5 10^6 to 1.6 10^6

5.5.2 Turbulence intensity, kinetic energy and decay

The turbulence intensity (Tu%) was computed as the ratio of the root mean square of velocity divided by its mean value. It presents a typical negative-exponent-power-law distribution, ranging from 5.3% for position A to a value of 2.5% for the last tested position. Results are presented in Fig. 5.14 where the natural turbulence intensity of the facility (no grid) is also presented, being slightly below 1%.
The effect of the Reynolds number on Tu was also investigated. The turbulence intensity distribution was measured for isentropic Reynolds numbers of $0.5 \cdot 10^6$ and $1.6 \cdot 10^6$ and the results are reported in Fig. 5.15. Tu% shows a clear dependency on Re: a variation of the Reynolds number implies a shift of the distribution to slightly higher values for an increase of Re_{2s}, to slightly smaller values when it is decreased.
The turbulent kinetic energy (K) was computed assuming turbulence to be homogeneous. The latter hypothesis is supported by several contributions in literature ([29] [74] [17]) where it is also suggested to define the two transversal RMS of velocity as 75% of the longitudinal one. By introducing the latter formulation, the turbulent kinetic energy was computed as:

$$K = \frac{1}{2}(\overline{(u')^2} + \overline{(v')^2} + \overline{(w')^2}) = \frac{1}{2}(\overline{(u')^2} + 2 * 0.75\overline{(u')^2}) \qquad (5.1)$$

According to literature [35], K should also present a power law distribution along the channel. Fig. 5.16 presents the computed value of K in the different positions along the inlet duct (dots) superimposed to a power-law fitting of the data (dashed line). As clearly visible, K reduces when moving the grid further upstream, in total accordance with the Tu% evolution. Moreover, by comparing the exponent n of the fitted power law with those presented by Valente et al. [56] a high degree of accordance can be found for grid-generated-turbulence. They reported a value of n equal to 1.25 while in the present case it is equal to $n = 1.29$.
The turbulence decay (ϵ) evolution along the channel was computed by differentiating the turbulent kinetic energy distribution with respect to space. The first term of equation 5.2 was transformed by means of first order ac-

curate finite differences into the last term on the right hand side.
It has to be remarked that the validity of the latter equation holds only for grid-generated homogeneous turbulence. Moreover, the application of a finite difference approach necessarily introduces another degree of uncertainty. Even though numerical values are not completely reliable, the trend along the channel is in absolute accordance with K and Tu distributions, as shown in Fig. 5.17. The decay rate decreases faster when the grid is placed close to the probe (position A), to became more less steep when moving it further upstream, with an asymptotic tendency towards zero.

$$\overline{u}\frac{\partial K}{\partial x} = -\epsilon = \overline{u(x)}\frac{K(x+1) - K(x)}{\Delta x} \tag{5.2}$$

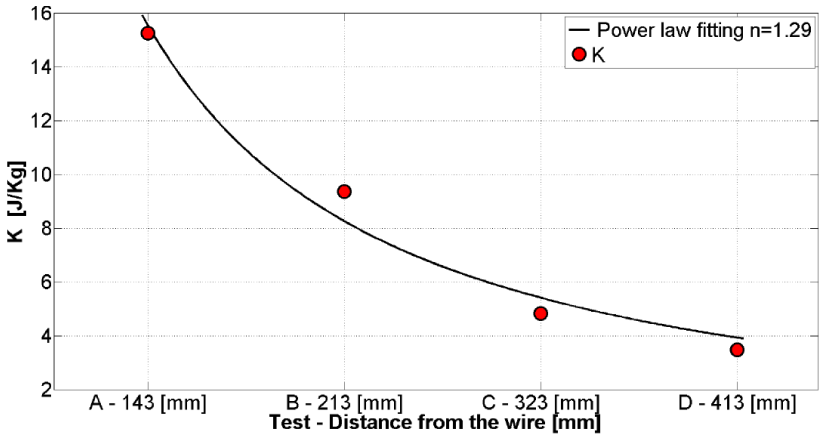

Figure 5.16: Measured turbulent kinetic energy against power law fitting (n=1.29)

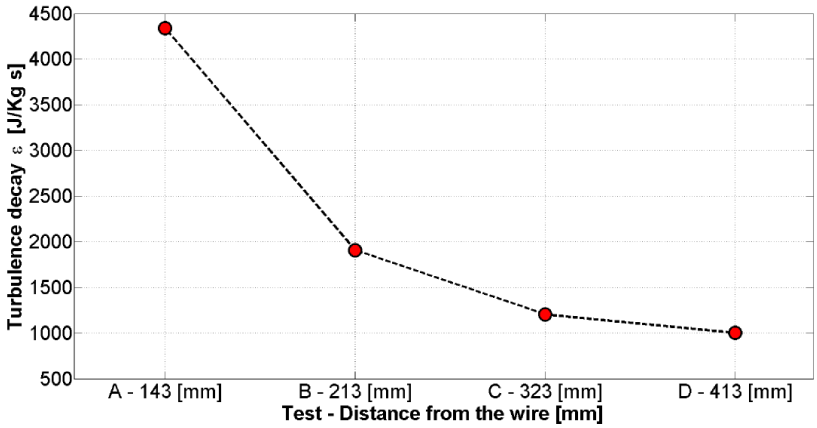

Figure 5.17: Turbulence rate of decay: distribution along the inlet duct

5.5.3 Turbulence length scales

The integral time scale τ was computed by integrating the autocorrelation coefficient $q(\tau)$ in time. By means of Taylor's frozen turbulence hypothesis the integral length scale L_1 was retrieved. Taylor's micro-scales were obtained by means of equation 5.3 and the frozen turbulence hypothesis with Re_l being the turbulent Reynolds number [42].

$$\lambda_1 = L_1 * \sqrt{\frac{15}{Re_l}} \tag{5.3}$$

Regarding the computation of the integral time scale, more details are given to describe the followed procedure. Because of the noise contamination of the measured data, the loss of correlation appears early, making the correlation coefficient distribution to oscillate. When approaching zero, these oscillations force $q(\tau)$ to assume negative values that could eventually lead to a negative integral value. To avoid this non-physical result, several methods are commonly used and discussed in literature (e.g. O'Neil et all. [60] and Theunissen et al. [63]). In the present application the first-zero-crossing stop criterion was adopted because it demonstrated to be the most

stable and reliable one.
The $q(\tau)$ distribution was stopped at the first crossing of the x-axis, fitted by means of a Gaussian fit [63] (see Fig. 5.18) and integrated. Different orders of the fitting function have been investigated to highlight the sensitivity of the computed values to the latter parameter. Even though they all demonstrated to provide consistent results, the most frequent value for each position along the channel was in the end selected.

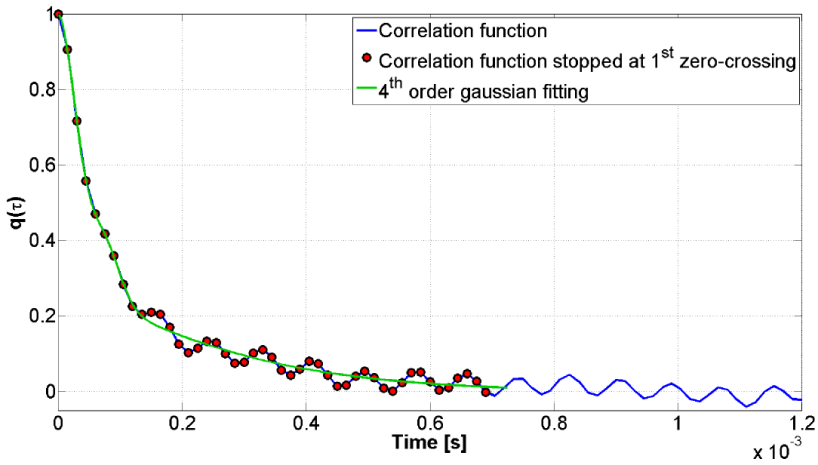

Figure 5.18: Typical example of fitted $q(\tau)$ distribution

The data scatter of the so computed τ is plotted for each position of the grid in Fig. 5.19 while the resulting integral length scale distribution is presented in Fig. 5.20 against a power law fitting.
The integral length scale L_1 monotonously grows when the grid is moved upstream, ranging from 7.5 $[mm]$ in position A up to 11 $[mm]$ for position D. These values are absolutely consistent with the geometry of the grid (3 [mm] cylinders, 12 [mm] pitch) that is in fact defining the main characteristic dimensions of the the flow field. The exponent of the power-law-fitted distribution (n=0.3495) is moreover in complete accordance with the one published by Valente et al. [56]: for grid-generated turbulence they report

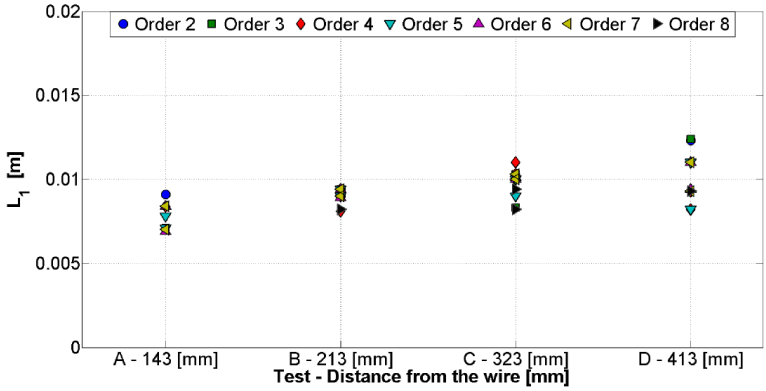

Figure 5.19: Sensitivity of the computation on L_1 to the order of the Gaussian fitting

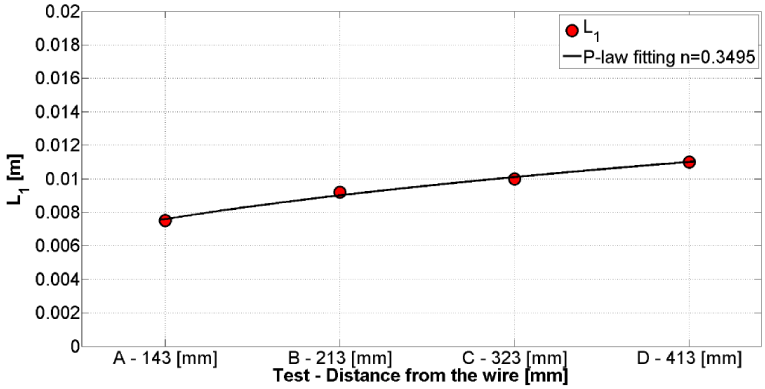

Figure 5.20: Integral length scale distribution along the channel against a power law fitting - n= 0.3495

in fact a value of n equal to 0.35.
Taylor's length scale evolution (Fig. 5.21) demonstrated to follow the trend of L_1: it constantly increases while the grid is moved further upstream, showing values that are absolutely consistent with the value of L_1 as well as with the characteristic dimensions of the flow field.

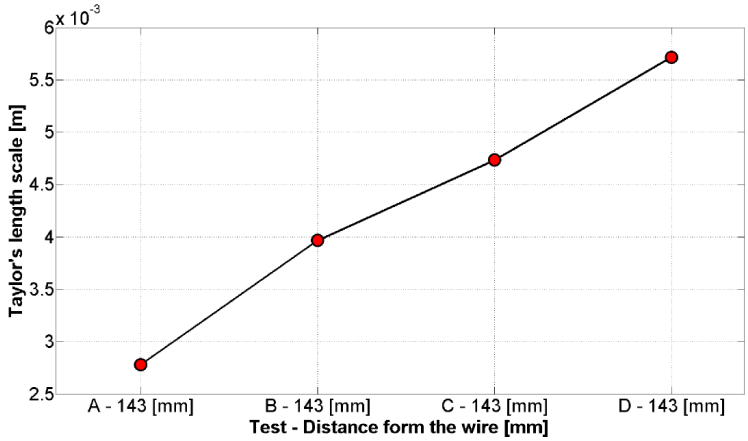

Figure 5.21: Taylor length scale distribution along the channel's length

5.6 Non-cooled cascade

When the cascade is operated without coolant injection, it is defined in the following as "non-cooled" case. The geometry remains anyway unchanged: film-cooling holes and feeding volumes were still present (see Sec. 5.3.2) while the coolant feeding system was blocked by closing a valve placed upstream the sonic orifice.

5.6.1 Aerodynamic performance of the cascade

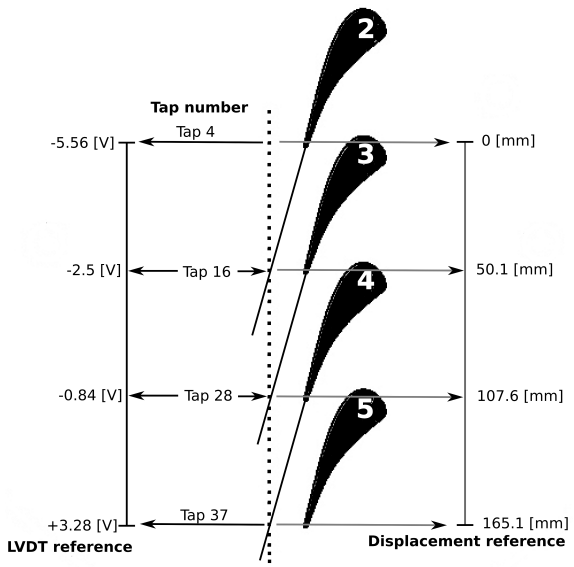

Figure 5.22: Frame of reference taps numbering, LVDT measured displacement [V] and displacement with respect to tap 4

A pneumatic three-hole probe was traversed along the pitch-wise direction at the mid section of the blade span. Along the traversing path, the total pressure wakes distribution ($P_{01} - P_{02}$) and the flow angle (β_2) were therefore retrieved. The performance of the cascade at different flow

regimes was then computed in terms of loss coefficient. Data were acquired at a sampling frequency equal to $f_s = 4$ [kHz] over an observation time of 0.55 [s]. Fig. 5.22 reports the frame of reference and the conventions used in the following chapter for the numbering of pressure taps, for the displacement given in volts of the LVDT equipping the pressure probe and for the corresponding displacement provided in millimeters.

Total pressure wakes

The results presented in this section have been all dynamically compensated before the application of the angular calibration. A demonstration of the validity of this correction can be found in Appendix C. When needed, a bow shock correction (Sec. 3.1.4) is automatically applied by taking the wall static pressure P_2 as representative of the flow field static pressure upstream the shock. The validity of the latter assumption is commented and demonstrated in Appendix D. In the end, it must be remarked that the presence of the probe in the flow field was found to provide a negligible effect as shown in Appendix E. Fig. 5.23 reports the downstream total pressure wakes evolution with Ma_{2s} for an isentropic Reynolds number nominally equal to $Re_{2s} = 1 \cdot 10^6$.

Within the subsonic range, an increase of the Mach number corresponds directly to an increase of the strength of the wakes. The latter do not move and cross the positions of taps 16 and 28, corresponding to the metallic exit angle definition (see Fig. 5.22). As soon as the sonic condition is reached, the wakes widen and shift towards the suction side while, in the middle of the channel, $P_{01} - P_{02}$ becomes noticeably higher than zero. This result can be only justified by the existence of shock waves upstream the measuring plane that degrade the local total pressure, also in the middle of the channel. The Schlieren visualization presented in Fig. 5.24 by Arts et al. [6] clearly supports this deduction: at $Ma_{2s} = 1.03$ a strong shock wave is generated by the rear part of suction side of the blade, extending further downstream until the wake of the adjacent blade highly weakens its strength.

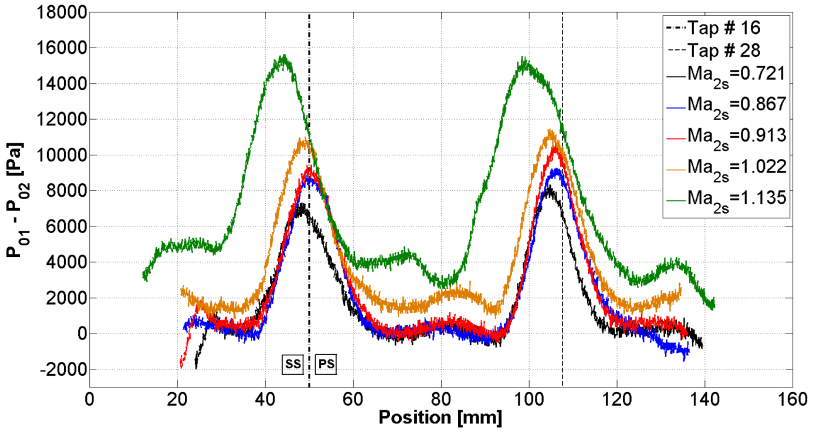

Figure 5.23: Non-cooled cascade: downstream total pressure wakes evolution for $Ma_{2s} = 0.7 - 1.1$ at $Re_{2s} = 10^6$

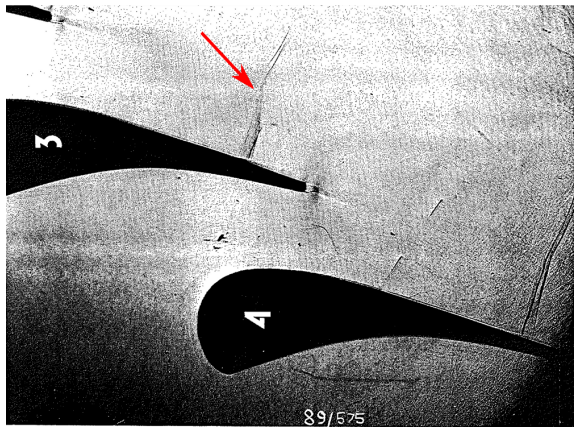

Figure 5.24: Schlieren photography of the LS-89 cascade at $M_{2s} = 1.03$ and $Re_{2s} = 10^6$ (Arts et al. - [6])

The evolution of the total pressure wakes with the Reynolds number is presented in Fig. 5.25 for a subsonic case (nominally $Ma_{2s} = 0.95$). As expectable, the intensity of total pressure wakes increases as the Reynolds number is augmented. Moreover, when increasing Re_{2s} from $0.5 \cdot 10^6$ up to one million, the pressure side region of the wake widens towards the center of the blade channel. The latter trend is inverted when the Reynolds number is further increased: by augmenting Re_{2s} from 10^6 up to $1.5 \cdot 10^6$, the suction side part of the wake experiences a relevant widening while the pressure side region is not affected at all. The latter region is probably laminar or transitional at $Re_{2s} = 0.5 \cdot 10^6$, and becomes fully turbulent when the Reynolds number is increased to one million. When the turbulent condition is reached, the smooth and continuous acceleration, almost independent of the Mach number (Arts et al. - [6]), is controlling the growth of the boundary layer and limiting its thickening, leading therefore to constant wake profile for high Reynolds numbers.
The behavior of the suction side area of the wake can be investigated by means of a comparison between the Schlieren photography reported in Fig. 5.27 ($Ma_{2s} = 1.03 - Re_{2s} = 10^6$) and the one presented previously in Fig. 5.24 ($Ma_{2s} = 1.03 - Re_{2s} = 2 \cdot 10^6$). It shows in fact that an increase of the Reynolds number implies a strengthening of the shocks generated in the rear part of the suction side. Given that the wakes evolution in Fig. 5.23 is referred to a high transonic flow condition, then it can be deducted that the scatter of a shock wave could be triggered by augmenting Re_{2s}, leading to a wider wake in this region.

In supersonic conditions (Fig. 5.26), the wakes distribution on the suction side area is instead completely dominated by the shock previously discussed. Wakes centres keep aligned and shifted towards the central part of the channel with a good matching of the suction side leg of the wake at high Reynolds numbers. The pressure side part experiences instead a slight but distinct widening when Re_{2s} is increased, according to the presence of a thicker boundary layer.

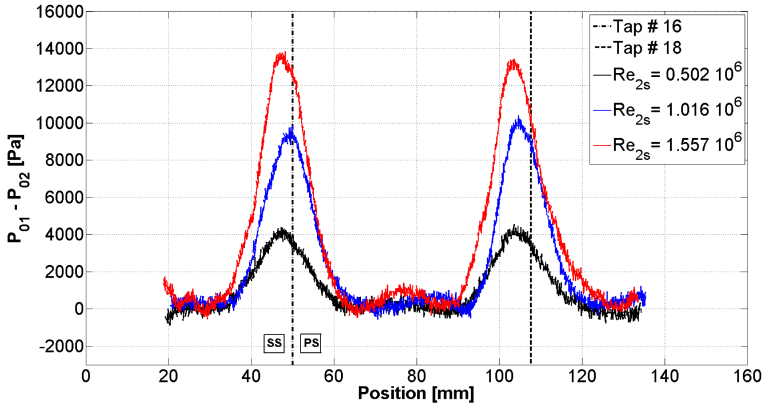

Figure 5.25: Non-cooled cascade: downstream total pressure wakes evolution with the Reynolds number for $Ma_{2s} = 0.95$

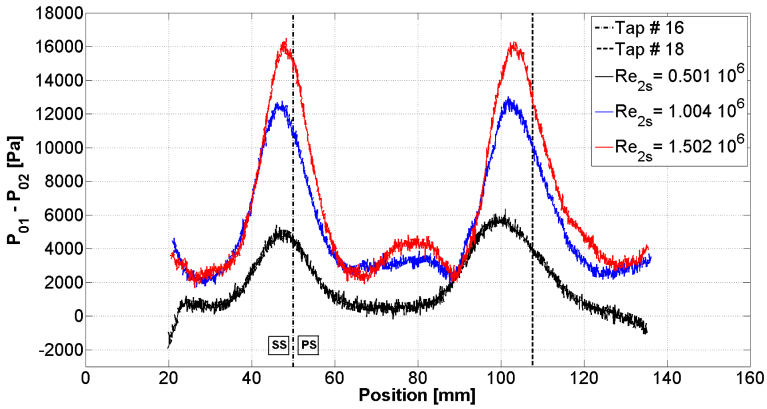

Figure 5.26: Non-cooled cascade: downstream total pressure wakes evolution with the Reynolds number for $Ma_{2s} = 1$

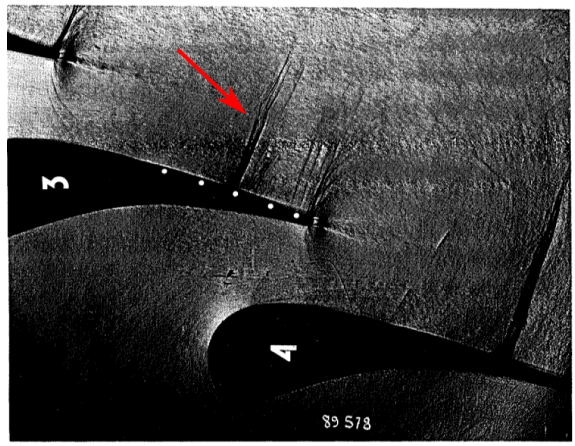

Figure 5.27: Schlieren photography of the LS-89 cascade at $M_{2s} = 1.03$ and $Re_{2s} = 2 \cdot 10^6$ (Arts et al. - [6])

5.6.2 Efficiency of the non-cooled cascade

The kinetic energy loss coefficient ζ was used to compute the performance of the cascade without injection. Its expression is reported in Eq. 2.9 (Gregory-Smith et al. [32]) where the superscript $\widehat{\ }$ indicates mass-averaged quantities.
Fig. 5.28 reports the mass-averaged loss coefficient evolution with respect to Ma_{2s}, for the tested Reynolds numbers. The three distributions present exactly the same behaviour: as soon as the sonic condition is approached, ζ increases drastically, reaching at $Ma_{2s} = 1.1$ a value 50% higher than the one in the subsonic range. This is clearly the effect of the shocks identified previously, that are strongly increasing the pressure drop also in the middle of the blade passage leading to a dramatic increase in terms of losses. The Reynolds number seems not to affect the performance at all: in both the subsonic and supersonic ranges, values are absolutely comparable for all three Re_{2s} conditions.
In plot 5.29, the loss distribution for $Re_{2s} = 10^6$ is plotted against the

one measured in the same flow conditions by Arts et al. [6] on the LS-89 geometry. The two trends present an identical dependency on Ma_{2s} but with higher values for the LS-94 film cooled profile at every Mach number. The latter is clearly an effect of the presence of the cooling holes that are triggering an early transition of the boundary layer, leading therefore to higher losses with respect to the non-cooled LS-89 geometry.

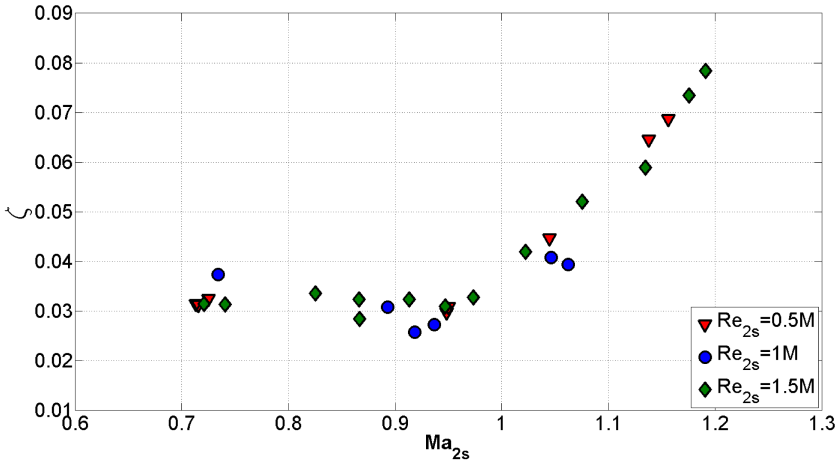

Figure 5.28: Non-cooled cascade: mass averaged loss coefficient ζ evolution with respect to the downstream isentropic Mach number for $Re_{2s} = 0.5 \cdot 10^6 \div 1.5 \cdot 10^6$

The evolution of the downstream mass averaged flow angle β_2 is presented in Fig. 5.30 for the three tested Reynolds numbers. The three of them tend to slightly increase towards the metal angle value (75 [°]) up to $Ma_{2s} = 0.9$ where it starts a constant and rapid decrease. Again, this is a consequence of the shock wave appearing as soon as the sonic condition is reached: by introducing a high total pressure drop, the turning of the cascade is necessarily affected and, consequentially, the efficiency degraded.

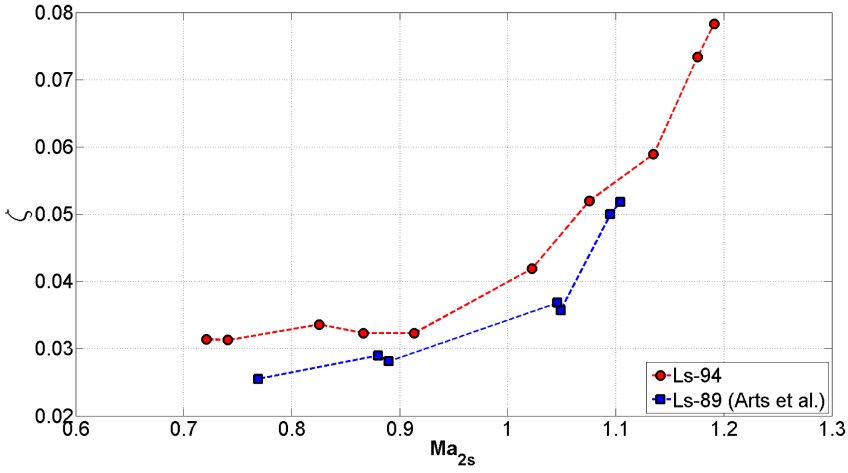

Figure 5.29: LS-94 (circles) and the LS-89 (squares) geometries: mass averaged loss coefficient ζ versus Ma_{2s} at $Re_{2s} = 10^6$

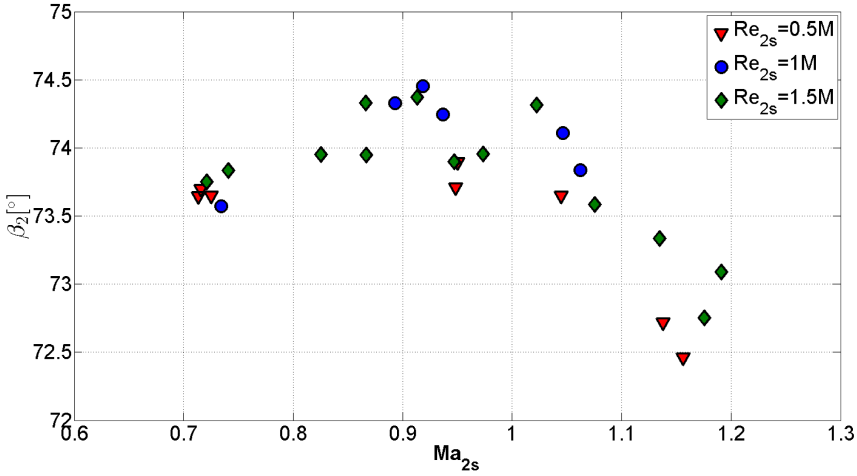

Figure 5.30: Non-cooled cascade: mass averaged downstream flow angle β_2 evolution with respect to the downstream isentropic Mach number for $Re_{2s} = 0.5 \cdot 10^6 \div 1.5 \cdot 10^6$

5.6.3 Thermal performance

The heat transfer characterization of the LS-94 was performed by means of the transient technique described in sec. 3.3 and using forty-two thin-films painted on the blade surface (coordinates are reported in Appendix F). Regarding the non-cooled cascade, the downstream isentropic Mach number M_{2s} was set at 0.9 while the effect of the isentropic Reynolds number Re_{2s} was investigated in a range spanning from $0.5 \cdot 10^6$ up to $1.5 \cdot 10^6$. The main-stream total temperature has been always kept equal to 420 [K].
Fig. 5.31 reports the results of the measurement campaign for the three tested Reynolds numbers. The first macroscopic effect related to a higher Re_{2s} coincides with a global augmentation of the value of h. In fact, an increase of the Reynolds number generally implies an enhancement of the energy transport inside the boundary layer and, above all, a diminishing of its thickness. This leads to more severe temperature gradients next to the surface and therefore to a worse thermal performance. The second effect of the Reynolds number can be highlighted instead when the evolution of the boundary layer along the blade surface is checked. At the lowest condition (circles), two distinct transition points are visible along the suction side at $S = 20$ [mm] and $S = 57$ [mm] respectively. As soon as the laminar boundary layer coming from the leading edge passes over the location of the holes ($S = 10 \div 20$ [mm]), a smooth but fast transition appears that ends in a fully turbulent state at $S = 30$ [mm]. The magnitude of h then decreases as the turbulent boundary layer develops and tends most probably to relaminarize under the effect of the acceleration of the second half of the suction side until the second transition appears. The second condition (squares) definitely presents the same evolution of the SS boundary layer even though the locations of the transition points is slightly shifted towards the leading edge. Moreover, the first transition results to be much more drastic than in the base case, providing a fully turbulent boundary layer right after the holes location.

If the Reynolds number is increased furthermore (triangles), the only modification that can be appreciated on the SS area is the tendency of the second transition point to disappear: in that condition the boundary layer

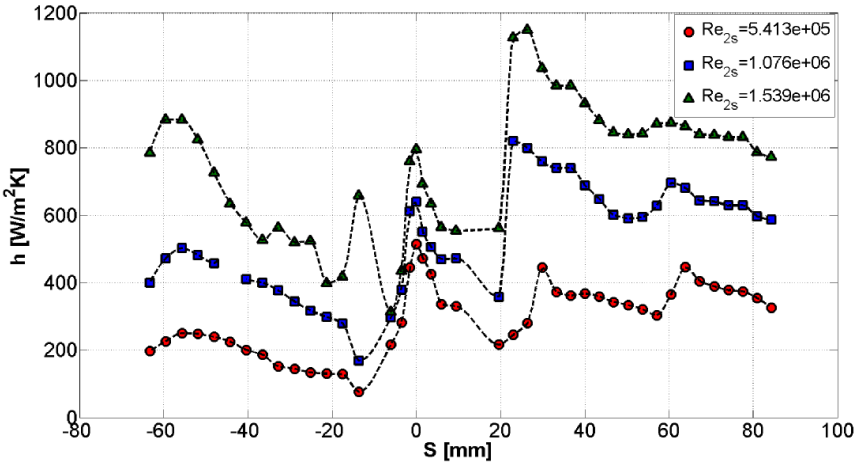

Figure 5.31: Non-cooled cascade: convective heat transfer coefficient distribution and its dependency of the Reynolds number

is most probably so energized that the beginning of the diffusive part of the blade (at about $S = 57$ [mm]) is not triggering any modification of its state. The pressure side evolutions present exactly the same behavior for first two cases (circles and squares): a laminar boundary layer develops in the LE area that becomes transitional as soon as the two rows of holes are crossed ($S = -6 \div -14$ [mm]). At this point, for the highest Reynolds number, the convective heat transfer coefficient distribution presents a drastic increase of h followed by a drop. This particular evolution on the boundary layer indicates most probably a holes-induced turbulent separation that is immediately damped by the acceleration imposed by the pressure side. After the re-impingement, a turbulent boundary layer develops up to the trailing edge. The distributions of h for the two lower Reynolds numbers do not present any turbulent separation behavior but, right after the holes, the boundary layer develops up to the trailing edge in a transitional state.

5.7 Suction side cooling

5.7.1 Cooling system characterization

The cooling system was characterized for an isentropic downstream Mach number ranging from 0.7 up 1.1 at $Re_{2s} = 1.5 \cdot 10^6$. The blade static pressure in correspondence of the exit of the cooling holes was measured by acquiring the feeding chamber pressure when injection was not taking place. The values of the ratio P_∞/P_{01} are summarized in table 5.5 for each tested Mach number. Fig. 5.32 reports the measured global discharge coefficient (Dc - Eq. 5.4) with respect to the blowing ratio (BR), as defined in Eq. 2.6.

Ma_{2s}	P_∞/P_{01}	δ
0.7	0.7312	$\pm$0.0039
0.9	0.6895	$\pm$0.0037
1	0.6861	$\pm$0.0036
1.1	0.6850	$\pm$0.0033

Table 5.5: Values of P_∞/P_{01} for the SS rows at the tested Mach numbers

$$Dc = \frac{\dot{m}_c}{\dot{m}_{sc}} \qquad (5.4)$$

Discharge coefficient values for the tested Mach numbers are all in accordance within the same blowing ratios range. They show moreover an asymptotic tendency to the chocked value that could be reached by increasing further the mass-flux ratio. In the same plot, the evolution of Dc for $Ma_{2s} = 1$ and $Re_{2s} = 0.5 \cdot 10^6$ is also shown (solid line). Even though it is presenting the same asymptotic tendency towards the chocked-condition, values are reduced by about 3%. The latter effect is probably a consequence of the combination of both, the variation of the density ratio ρ_c/ρ_∞ and a different evolution of the boundary layer along the first part of the SS, both of them functions of the Reynolds number (see Fig. 5.25).

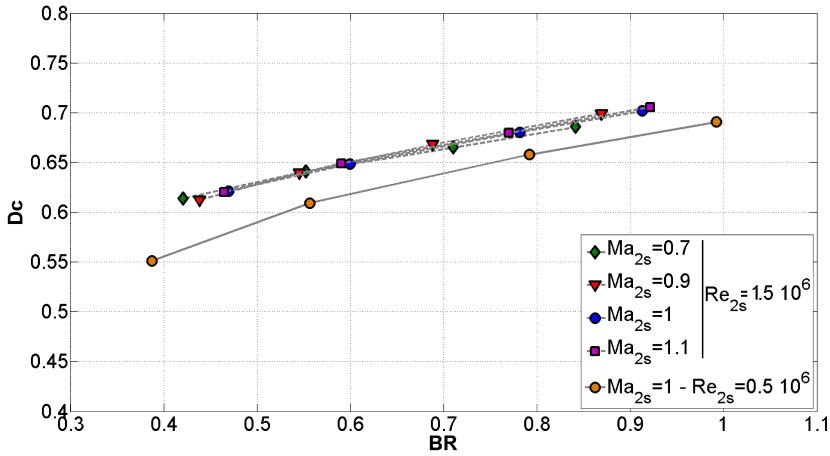

Figure 5.32: Suction side cooling: discharge coefficient evolution with respect to BR at $Re_{2s} = 1.5 \cdot 10^6$ and $Ma_{2s} = 0.7 - 1.1$

5.7.2 Total pressure wakes

To highlight the effect of injection on total pressure wakes, a comparison is made in Fig. 5.33 between the non-cooled case and two cooled ones at $BR = 0.438$ and $BR = 0.869$ respectively. Both of them are referred to a high subsonic case ($Ma_{2s} = 0.9$) at a downstream isentropic Reynolds number equal to $1.5 \cdot 10^6$.
When injection takes place, wakes widen towards the suction side and tend to increase. It has to be underlined how the smallest injection rate creates the biggest drift of the wake shape while, for the highest blowing ratio, the shift experienced by the suctions side region keeps generally smaller. In the latter condition, the injection process is in fact acting as a boost on the low-momentum flow next to the wall, leading to a more energized boundary layer and therefore to a thinner wake.

Fig. 5.34 reports the evolution of wakes with injection for a supersonic condition (nominally $Ma_{2s} = 1.1$). As already discussed in section 5.6.1,

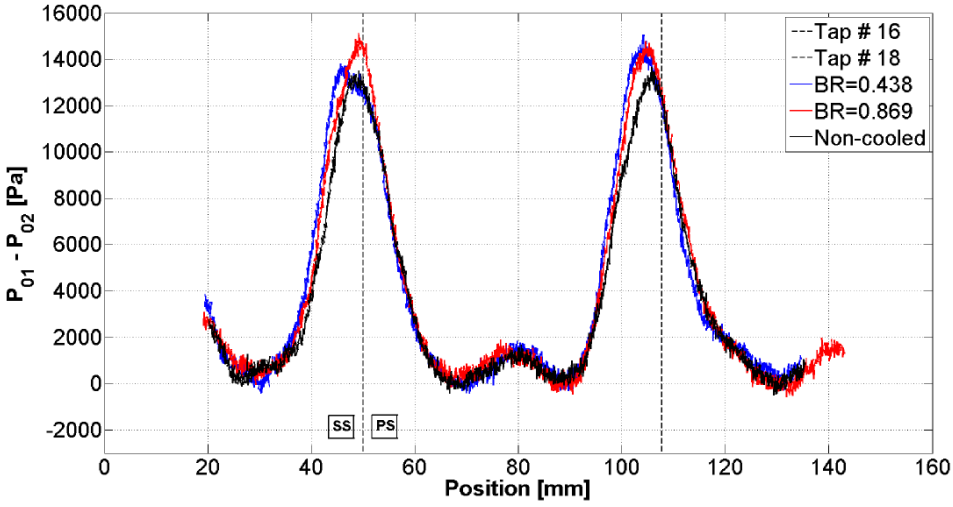

Figure 5.33: Suction side cooling: total pressure wakes evolution for two distinct injection conditions ($BR = 0.438\,/\,0.869$) compared to the non-cooled case at $Ma_{2s} = 0.9$ and $Re_{2s} = 1.5 \cdot 10^6$

at $Ma_{2s} = 1$ or higher, a strong shock wave is generated by the rear part of the suction side. Under these conditions, the effect of injection on total pressure wakes is damped by such a strong discontinuity, making the different profiles almost collapsing on the non-cooled case in the suction side region. Nevertheless injection produces anyway a deeper wake, characterized by a higher pressure drop peak value.

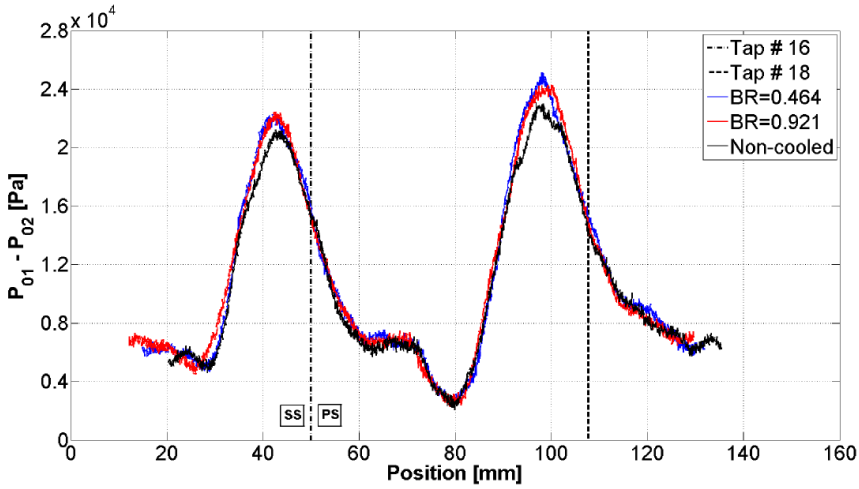

Figure 5.34: Suction side cooling: total pressure wakes evolution for two distinct injection conditions ($BR = 0.438\,/\,0.869$) compared to the non-cooled case at $Ma_{2s} = 1.1$ and $Re_{2s} = 1.5 \cdot 10^6$

Performance of the cooled cascade

Losses for cooled cascades are generally presented in terms of the thermodynamic loss coefficient ζ_c (Eq. 2.4), to take into account the different energy levels of both, the coolant and the main-stream. Since the main-stream mass-flow could not be measured with an acceptable accuracy, ζ_c was modified into the new formulation ζ_c^* (Eq. 5.5) where $\dot{m}$ is substituted with the main-stream mass-flow in chocked conditions $\dot{m}^*$.
In Fig. 5.35 the evolution of the loss coefficient is presented for the tested Mach numbers ($Ma_{2s} = 0.7 - 1.1$) at $Re_{2s} = 1.5 \cdot 10^6$. All the distributions present a minimum in the range $BR = 0.5 - 0.6$ followed by a continuous increase except for the case at $Ma_{2s} = 0.7$ that is in fact monotonously growing. The latter, moreover, shows the highest variation in terms of loss coefficient, increased by about 50% with respect to the first value and showing losses even higher than those for $Ma_{2s} = 0.9$.
The downstream flow angle β_2 is instead very little affected by the injection process. As clearly visible from Fig. 5.36, all the distributions appear almost flat with respect to BR, the highest variation being smaller than 0.5 [°] for $Ma_{2s} = 1.1$. In the end, a comparison between the two subsonic cases suggest that the cascade tends to perform better at $Ma_{2s} = 0.9$ than at $Ma_{2s} = 0.7$ (higher downstream discharge angle) as a consequence of the fact that the design Mach number was in fact equal to 0.9 .
A final conclusion on the effect of injection on the performance of the cascade, can be drawn by a comparison with the non-cooled results. The horizontal lines in Fig. 5.35 and Fig. 5.36 correspond respectively with the loss coefficient and the flow angle values of the non-cooled cascade at $Ma_{2s} = 1.1$. Generally speaking, the taking place of injection is responsible for an increasing of the aerodynamic loss and consequent reduction in terms of turning of cascade. This discrepancy, present since the lowest injection conditions, is then doomed to grow as soon as the blowing ratio is enhanced.

$$\zeta_c^* = 1 - \frac{\left[1 - \left(\frac{\widehat{P_2}}{\widehat{P_{02}}}\right)^{(\frac{\gamma-1}{\gamma})_m}\right][\dot{m}^* T_{01} + \dot{m}_c T_{0c}]}{\dot{m}^* T_{01}\left[1 - \left(\frac{\widehat{P_2}}{P_{01}}\right)^{(\frac{\gamma-1}{\gamma})_g}\right] + \dot{m}_c T_{0c}\left[1 - \left(\frac{\widehat{P_2}}{P_{0c}}\right)^{(\frac{\gamma-1}{\gamma})_c}\right]} \tag{5.5}$$

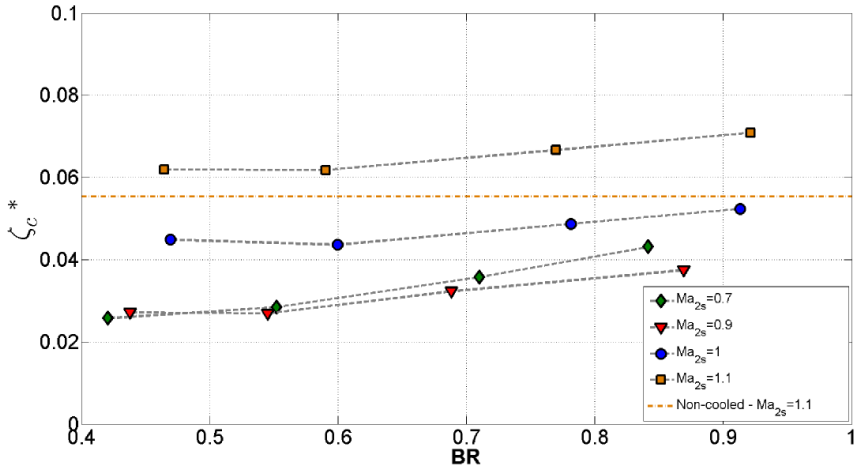

Figure 5.35: Suction side cooling: ζ_c^* distribution with respect to BR for varying exit isentropic Mach numbers at $Re_{2s} = 1.5 \cdot 10^6$

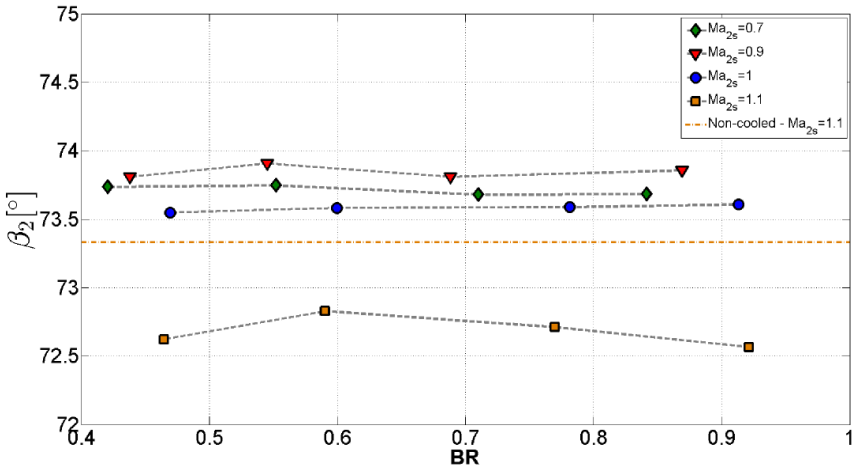

Figure 5.36: Suction side cooling: β_2 distribution with respect to BR for varying exit isentropic Mach numbers at $Re_{2s} = 1.5 \cdot 10^6$

5.7.3 Thermal performance

Cooled tests have been run at $M_{2s} = 0.8$ and $M_{2s} = 1.1$ for an isentropic Reynolds number nominally equal to $Re_{2s} = 1.5 \cdot 10^6$ and a measured turbulence intensity of $Tu = 5.3\%$. Two types of results are always shown. The first one is the evolution of the convective heat transfer coefficient along the suction-side from the non-cooled case to the highest injection condition. The second one corresponds to the distributions of the ratio h/h_{ref}, where h_{ref} is the measured convective heat transfer coefficient for the non-cooled case (same airfoil but without injection). Regarding the computation of the last parameter it has to mentioned that, given the availability of multiple tests at the same exact conditions, the non-cooled case distribution corresponds to an average of the existing dataset.

Downstream isentropic Mach number $M_{2s} = 0.8$

Figure 5.37-a reports the evolution of the convective heat transfer evolution for the suction side at different injection conditions. The main difference between the non-cooled and the cooled case is visible immediately after the holes ($S = 10 \div 20$ [mm]): the abrupt transition of the reference case is replaced by a smoother increase that ends in a plateau, providing, for each condition, a constant protection until the trailing edge. The highest injection rates show between $S = 20$ [mmm] and $S = 30$ [mmm] an evolution that recalls the case of a separation / reattachment, both with a positive peak at $S = 23$ [mmm] and a negative one at $S = 26$ [mmm]. This is probably caused by the too high momentum of the coolant that highly destabilizes the boundary layer when passing over the injection rows. In fact, the two highest injections provide right after the holes an increasing of the convective heat transfer coefficient of about 10% (box in Fig. 5.37-b). This indicates that the injection jets highly perturb the boundary layer, augmenting the turbulent mixing and therefore the heat transfer rate towards the surface. Fig. 5.37-b demonstrates the beneficial effect of an enhanced injection: starting from $S = 25$ [mm], increasing furthermore the blowing ratio always leads to a better protection of the suction side till the trailing edge that is the highest thermally-loaded area after the injection rows.

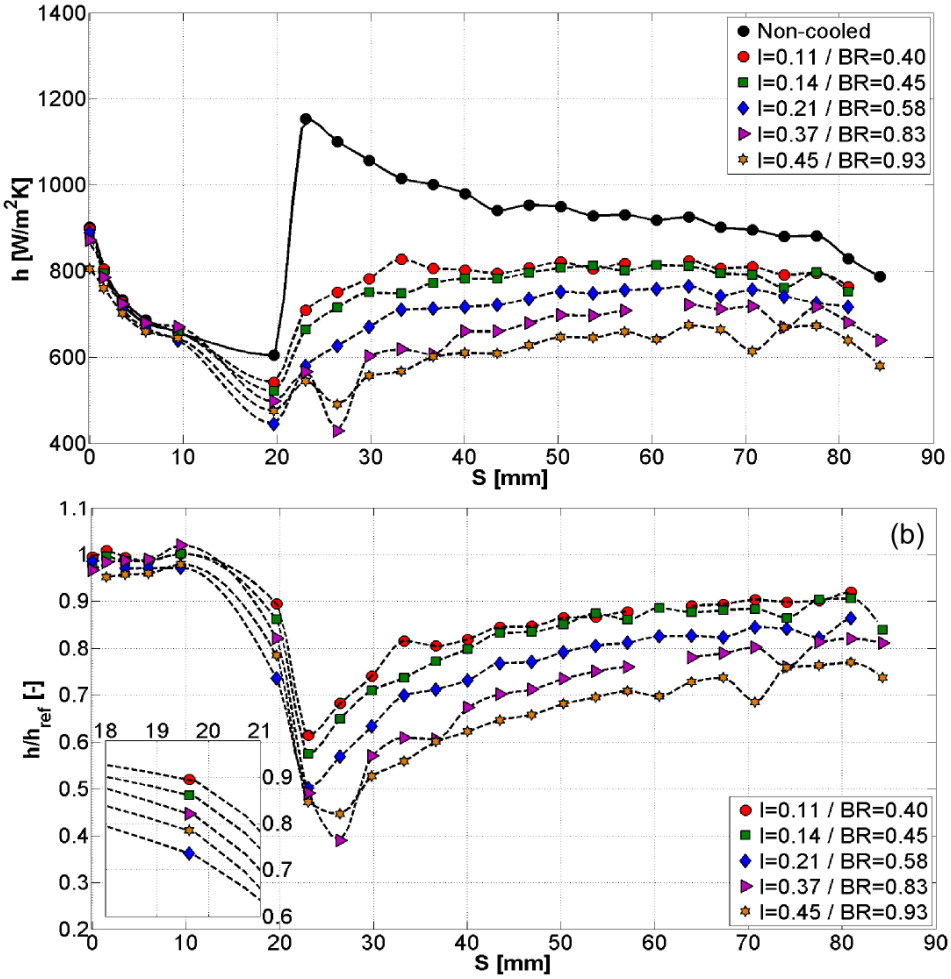

Figure 5.37: Suction side cooling at $M_{2s} = 0.8$, $Re_{2s} = 1.5 \cdot 10^6$ and $Tu = 5.3\%$: (a)- Evolution of $h[W/m^2K]$ for the suction side at different injection conditions ; (b)- h/h_{ref} evolution for the suction side at different injection rates, with h_{ref} the non-cooled case distribution

Downstream isentropic Mach number $M_{2s} = 1.1$

The evolution of h (Fig. 5.39-a) without injection and for $M_{2s} = 1.1$ is definitely close to the one of the subsonic case: a laminar boundary layer develops from the leading edge up to the location of the holes where a steep transition occurs. h starts then to decrease rapidly as the fully turbulent boundary layer develops until $S = 75$ [mm] where a peak is present. The latter must be related with the shock wave present in the rear part of the suction side as shown previously in Fig. 5.24 and Fig. 5.27 (red pointer). When injection is performed, the distributions generally become smoother. The drastic transition at $S = 20$ [mm] is highly damped as well as the peaks at the location of the shock wave while the short plateau shown at $S = 40$ [mm] by the non-cooled blade can still be recognized also in the cooled cases. After the cooling rows, the magnitude of the convective heat transfer distribution keeps generally lower than the non-cooled distribution. In fact, as presented in Fig. 5.39-b, the lowest injection rate produces at least a 5% reduction with respect to the non-cooled case and in correspondence of the trailing edge of the blade that results to be again the highest thermally loaded point of the cooled part of the blade. The main difference with respect to the distribution at $M_{2s} = 0.8$ lies right after the cooling rows. In the subsonic case, the non-cooled blade in this point was always performing worse than any other cooled case while, at $M_{2s} = 1.1$, values are much closer to each others. In particular the beneficial effect of injection is evident only for the third and the fourth cooled cases as the two lowest ones are providing almost the same values of the non-cooled distribution. An interpretation of this behavior can be given thanks to the work of F.L. Peña [23] that describes how a coolant jet tends to spread laterally rather than stream-wise at low injection rates, providing therefore a bad protection right downstream the exit of the hole. It is the author's opinion that even though Peña investigated one single row of holes, the given explanation should hold true also for the case of two staggered rows of film-cooling holes. Increasing the coolant mass-flow leads generally to a better protection of the surface. In particular it has to be highlighted how the first and second injection rates are providing almost the same values

while a clear improvement can be appreciated for $I = 0.24$ / $BR = 0.63$. At this flow regime is moreover evident the negative effect that a too high coolant momentum produces on the boundary layer: the highest injection rate provides, between $S = 20$ [mm] and $S = 30$ [mm], a worse protection than the two intermediate cooling conditions (box in Fig. 5.39-b).

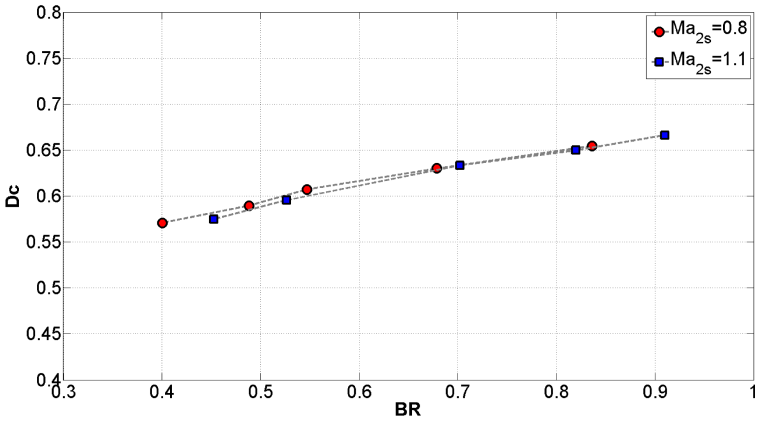

Figure 5.38: Suction side cooling, low temperature coolant: discharge coefficient evolution with respect to BR at $Re_{2s} = 1.5 \cdot 10^6$ and $Ma_{2s} = 0.8/1.1$ for the low-temperature-coolant tests

Low temperature coolant

The thermal performance of the cascade was also assessed by injecting coolant at about 265 [K]. Fig. 5.40(a,b) and Fig. 5.41(a,b) show the distributions of h and of the ratio h/h_{ref} for $M_{2s} = 0.8$ and $M_{2s} = 1.1$ respectively. All around the blade surface, values are generally lower than for the ambient coolant case, at every injection rate. The portion of the suction side that benefits the most from the lower temperature of the coolant is the region immediately downstream the cooling rows ($S = 20 - 25$ [mm]) where the convective heat transfer coefficient magnitude is reduced to almost 50%. The discharge coefficient evolution for the two tested Mach numbers is re-

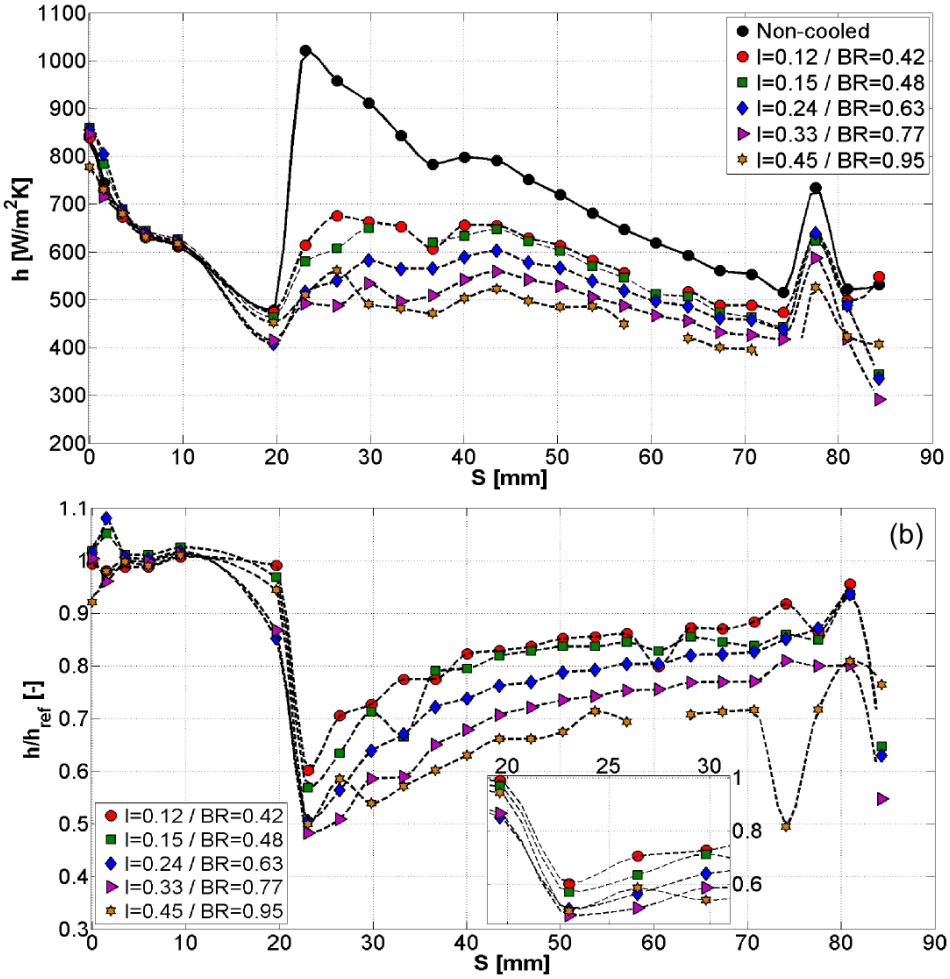

Figure 5.39: Suction side cooling at $M_{2s} = 1.1$, $Re_{2s} = 1.5 \cdot 10^6$ and $Tu = 5.3\%$: (a)- Evolution of $h[W/m^2K]$ for the suction side at different injection conditions ; (b)- h/h_{ref} evolution for the suction side at different injection rates, with h_{ref} the non-cooled case distribution

ported in Fig. 5.38 with respect to BR. The two distributions show the typical asymptotic behaviour towards the chocked condition values, with magnitudes of about 3% smaller than for the ambient coolant case.

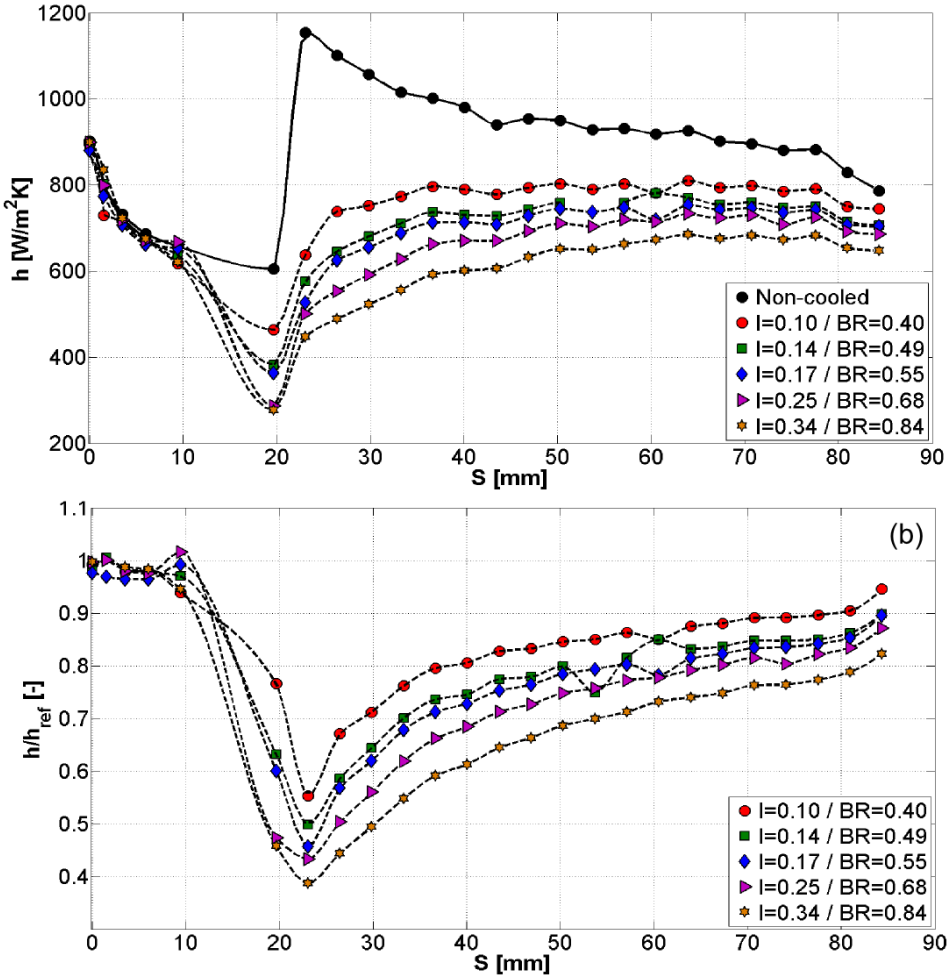

Figure 5.40: Suction side cooling, low temperature coolant at $M_{2s} = 0.8$, $Re_{2s} = 1.5{\cdot}10^6$ and $Tu = 5.3\%$: (a)- Evolution of $h[W/m^2K]$ for the suction side at different injection conditions ; (b)- h/h_{ref} evolution for the suction side at different injection rates, with h_{ref} the non-cooled case distribution

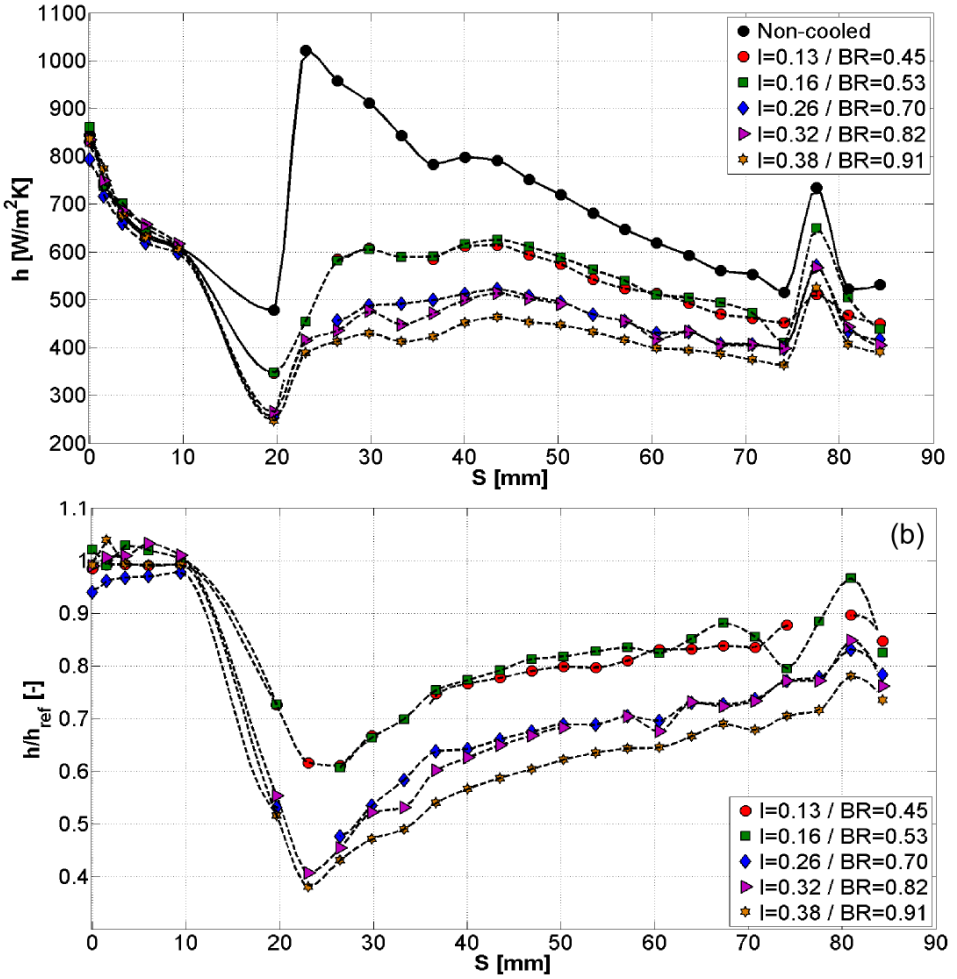

Figure 5.41: Suction side cooling, low temperature coolant at $M_{2s} = 1.1$, $Re_{2s} = 1.5{\cdot}10^6$ and $Tu = 5.3\%$: (a)- Evolution of $h[W/m^2K]$ for the suction side at different injection conditions ; (b)- h/h_{ref} evolution for the suction side at different injection rates, with h_{ref} the non-cooled case distribution

5.8 Pressure side cooling

5.8.1 Cooling system characterization

The cooling system was characterized for an isentropic downstream Mach number ranging from 0.7 up to 1.1 at $Re_{2s} = 1.5 \cdot 10^6$. The measured values of the P_∞/P_{01} ratio for the tested Mach numbers are reported in table 5.6. Fig. 5.42 presents the measured global discharge coefficient with respect to the blowing ratio (BR).

Ma_{2s}	P_∞/P_{01}	δ
0.7	0.9897	$\pm$0.0037
0.9	0.9899	$\pm$0.0041
1	0.9913	$\pm$0.0044

Table 5.6: Values of the ratio P_∞/P_{01} for the pressure side cooling rows at the tested Mach numbers

Discharge coefficient values are showing an increasing trend with BR, towards the limit value reached for the chocked condition. Within the investigated range of mass-flux ratios, they all provide similar values whose magnitude results to be less than 5% higher than the ones measured for the suction side case. The dependency on the Reynolds number is shown instead in Fig. 5.43 that reports the evolution of Dc with BR at $Ma_{2s} = 0.9$. As already documented in the previous chapter, by increasing Re_{2s}, discharge coefficients distributions are shifted towards higher values because of the joined effect of both, the density ratio and a different evolution of the boundary layer along the pressure side. Particularly, it has to be highlighted how the distributions for $Re_{2s} = 10^6$ and $Re_{2s} = 1.5 \cdot 10^6$ present exactly the same evolution, with a difference in magnitude of about 1%, while the lowest Reynolds number shows instead a maximum discrepancy of more than 6% and a distinctly different slope.

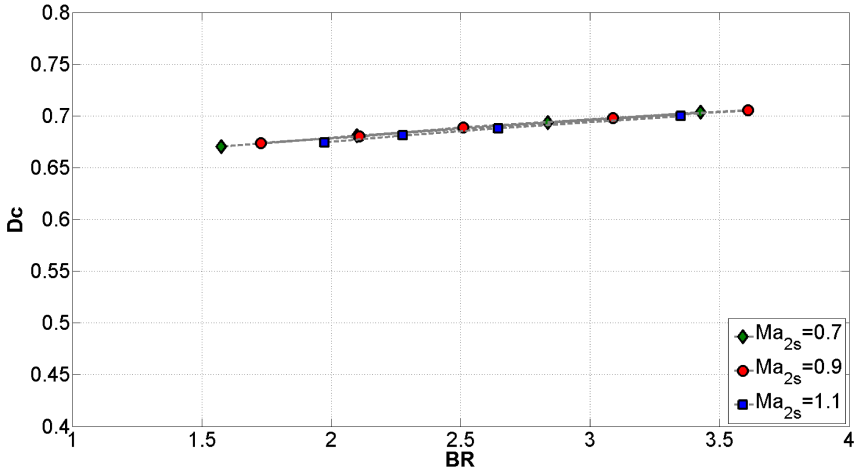

Figure 5.42: Pressure side cooling: discharge coefficient evolution with respect to BR at $Re_{2s} = 1.5 \cdot 10^6$ and $Ma_{2s} = 0.7 - 1.1$

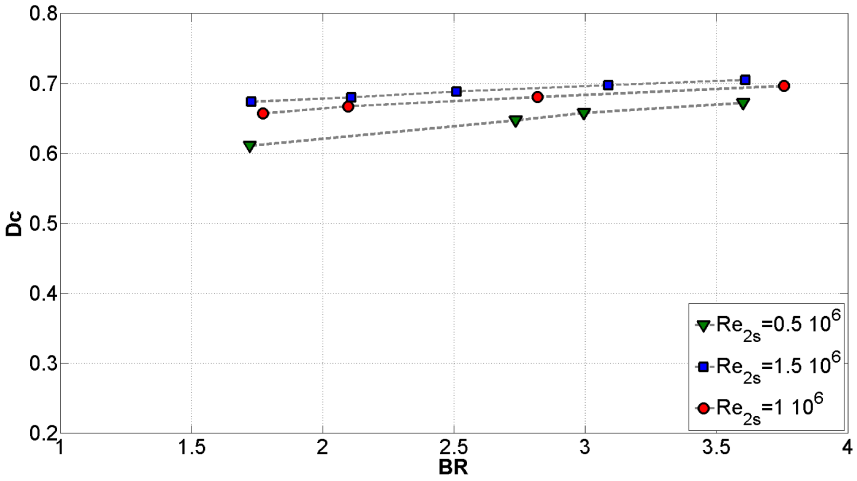

Figure 5.43: Pressure side cooling: discharge coefficient evolution with respect to BR at $Ma_{2s} = 0.9$ for $Re_{2s} = 0.5 \cdot 10^6$ (green symbols), $Re_{2s} = 10^6$ (red symbols) and $Re_{2s} = 1.5 \cdot 10^6$ (blue symbols)

5.8.2 Total pressure wakes

Fig. 5.44 presents the evolution of total pressure wakes for two different mass-flux ratios at $Ma_{2s} = 0.7$ and $Re_{2s} = 1.5 \cdot 10^6$. At the smallest injection rate, wakes keep aligned to the non-cooled case and they only experience a slight increase of their peak value. At a higher mass-flux ratio, the pressure side region widens with a further increase of the peak value. In the middle of the blade passage it is impossible to recognize any particular effect related to injection.

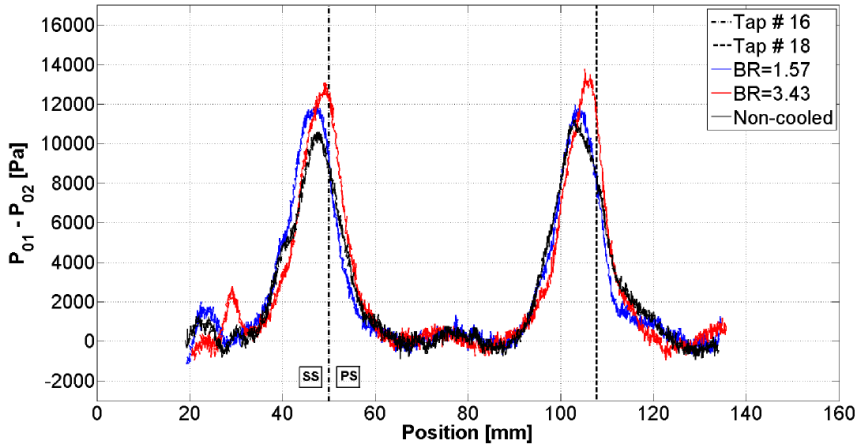

Figure 5.44: Pressure side cooling: pressure wakes evolution for two distinct injection conditions ($BR = 1.57/3.43$) compared to the non-cooled case at $Ma_{2s} = 0.7$ and $Re_{2s} = 1.5 \cdot 10^6$

By increasing the isentropic downstream Mach number up to a supersonic condition, the injection induced variations on pressure wakes distributions disappear. In Fig. 5.45 ($Ma_{2s} = 1.1$; $Re_{2s} = 1.5 \cdot 10^6$; $BR = 1.97\,/\,3.35$) one can see how well cooled pressure wakes are overlapping the non-cooled case one, without any relevant difference that could be linked to the injection phenomenon.

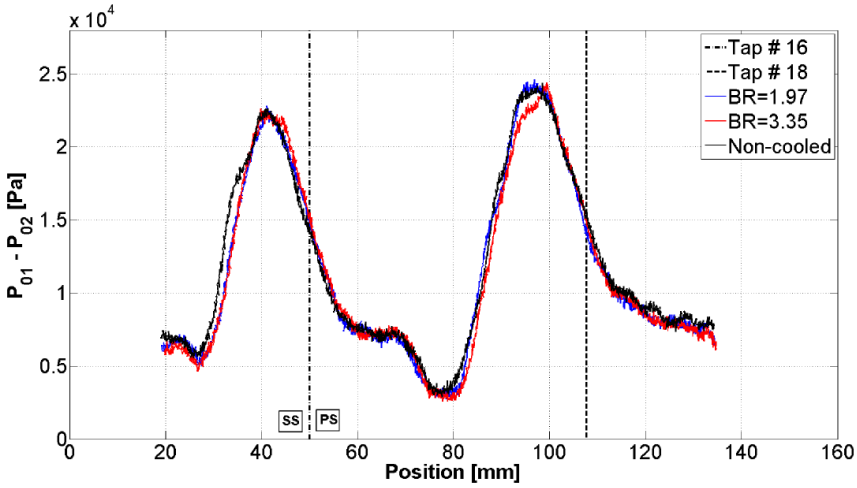

Figure 5.45: Pressure side cooling: pressure wakes evolution for two distinct injection conditions ($BR = 1.97\,/\,0.3.35$) compared to the non-cooled case at $Ma_{2s} = 1.1$ and $Re_{2s} = 1.5 \cdot 10^6$

Performance of the cooled cascade

The modified thermodynamic loss coefficient ζ_c^* evolution with respect to BR is presented in Fig. 5.46. In the subsonic range, losses increase with the increase of the injection rate with an almost linear trend. The same behaviour is shown also by the $Ma_{2s} = 1.1$ case even though with a less steep slope. The latter result indicates that losses are mainly driven by the poor performance of the cascade in supersonic conditions (see section 5.6.2) and it is also demonstrated by the previously commented Fig. 5.45, where it was impossible to appreciate any variation on total pressure wakes that could have been related to the injection process. The downstream measured flow angle is plotted for the three tested Mach numbers in Fig. 5.47, with respect to the mass-flux ratio. The three distributions suggest that β_2 is not affected at all by injection, showing an almost constant value all over the BR range. As documented already in section 5.7.2, here again it is demonstrated that the cascade tends to perform better at $Ma_{2s} = 0.9$ than at $Ma_{2s} = 0.7$ since it presents a value of the discharge angle closer to the metallic one (75 [°]). A comparison with the performance of the non-cooled cascade is also shown in the following plots, for an isentropic downstream Mach number of 0.9. As expected, the loss coefficient distribution (Fig. 5.46) of the cooled case keeps higher than the non-cooled one, at every injection condition. The injection-induced degradation of the performance is visible as well in the flow angle evolution (Fig. 5.47): the turning that the cooled cascade is able to provide, is always lower than the non-cooled one. The effect of the Reynolds number on the performance of the cascade is instead investigated by means of Fig. 5.48 and 5.49 where ζ_c^* and β_2 are presented with respect to BR at $Ma_{2s} = 0.9$. At low Reynolds number the cascade produces the lowest losses and therefore the highest turning. At higher Re_{2s} losses increase while β_2 is reduced, with the highest loss shown by the case at $Re_{2s} = 10^6$. The three distributions all present the same trend.

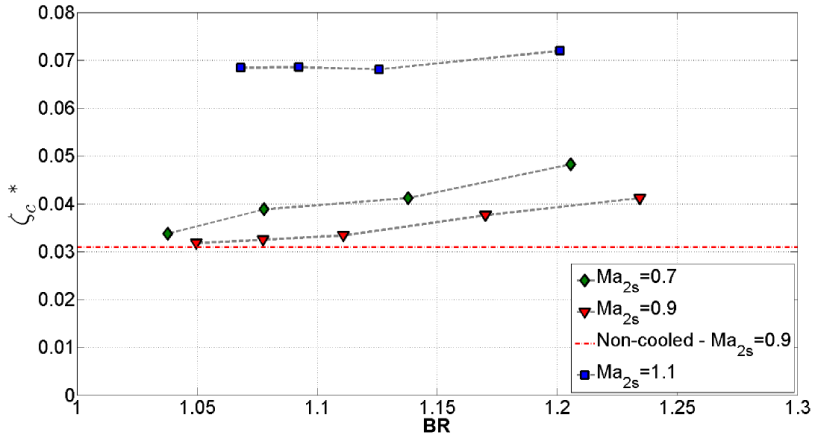

Figure 5.46: Pressure side cooling: ζ_c^* distribution with respect to BR for the tested isentropic Mach numbers at $Re_{2s} = 1.5 \cdot 10^6$

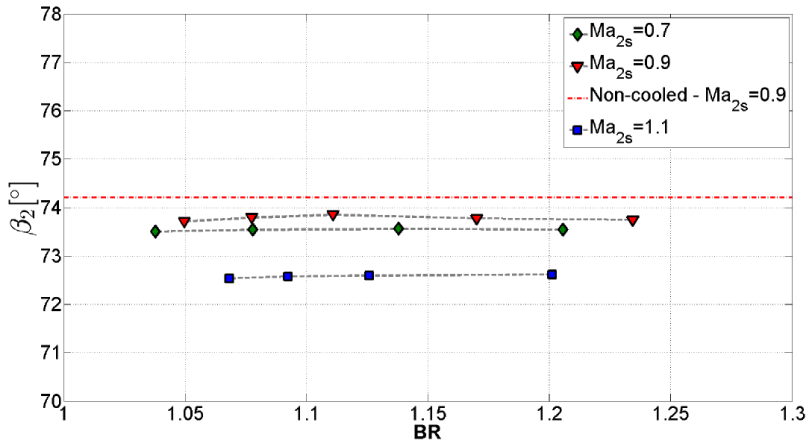

Figure 5.47: Pressure side cooling: β_2 distribution with respect to BR for the tested isentropic Mach numbers at $Re_{2s} = 1.5 \cdot 10^6$

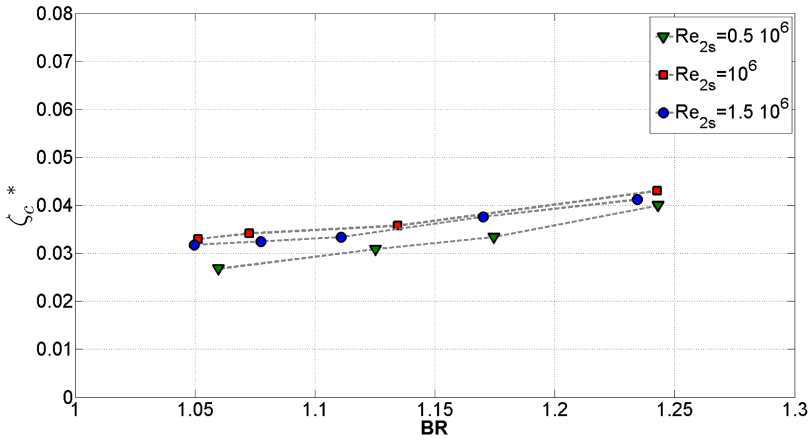

Figure 5.48: Pressure side cooling: ζ_c^* distribution with respect to BR for the tested Reynolds numbers at $Ma_{2s} = 0.9$

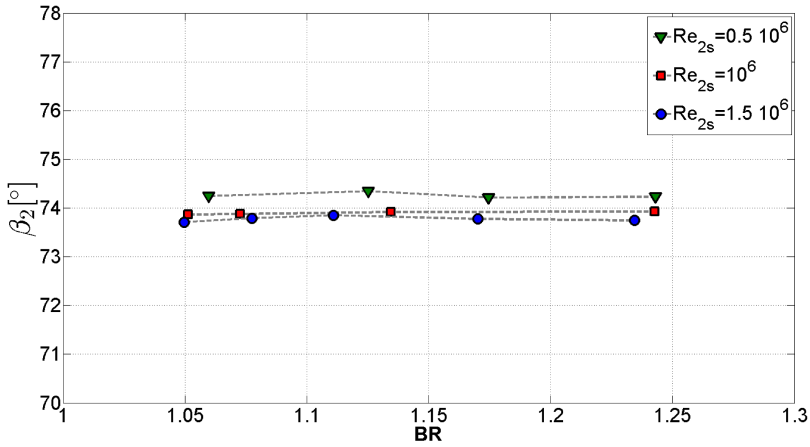

Figure 5.49: Pressure side cooling: β_2 distribution with respect to BR for the tested Reynolds numbers at $Ma_{2s} = 0.9$

5.8.3 Thermal performance

Downstream isentropic Mach number $M_{2s} = 0.8$

Fig. 5.50-a shows the evolution of the convective heat transfer coefficient along the pressure side with and without injection that is performed by means of two rows of staggered holes located between $S = 6$ [mm] and $S = 15$ [mm]. The boundary layer develops as laminar from the leading edge area up to the injection holes. At $S = 15$ [mm] the non-cooled blade distribution (solid line) presents a peak that most probably is linked to a local separation happening over the holes and followed by an impinging reattachment exactly in this point. A transitional boundary layer is then re-established that undergoes a long and smooth transition till the trailing edge, without showing any fully-turbulent characteristic. Injection on the pressure side area has a stronger effect of the evolution on the boundary layer than what found for the suction side. The re-attachment pattern is shown also by every other distribution apart for the lowest injection condition that, at $S = 15$ [mm], actually provides the best insulating performance. In Fig. 5.50-b the lowest inject rate shows a value of h that is in fact 60% lower than the non-cooled case even though starting from $S = 40[mm]$ no other beneficial effect can be appreciated. Increasing further the coolant mass-flow coincides, between $S = 15$ [mm] and $S = 25$ [mm], always with a worsening of the thermal performance until the most undesired condition is reached. For the highest injection rate in fact, the ratio between the cooled convective coefficient and the non-cooled one becomes higher than one. At $I = 9.82$ / $BR = 3.96$ the coolant jets have such a high momentum that they *drill* the boundary layer, destroying its front and increasing so much the mixing that hot main-stream air is entrained and put in contact with the blade surface. Immediately after the boundary layer is reconstructed and it starts developing with a transitional behaviour. The back part of the pressure side generally benefits from an enhanced injection even though the two highest injection rates provide a better protection only from $S = 30$ [mm] and $S = 40$ [mm] respectively.

Downstream isentropic Mach number $M_{2s} = 1.1$

At $M_{2s} = 1.1$ the non-cooled case distribution of the convective heat transfer coefficient (Fig. 5.51-a) strongly recalls the one obtained for the subsonic case. The laminar boundary layer created in the leading edge area tends to detach over the holes and to re-impinge immediately after, creating the typical peak at $S = 15$ [mm]. The remaining part of the pressure side is characterized by a transitional boundary layer that gets to the trailing edge without reaching a fully turbulent state. In supersonic conditions, injection does not really modify the evolution of the boundary layer: apart for the lowest injection rate that shows a plateau between $S = 5$ [mm] and $S = 15$ [mm], the remaining distributions all show the re-impinging peak and the long transitional evolution up to the trailing edge. From Fig. 5.51-b it can be appreciated how the lowest injection condition provides the best performance immediately after the cooling rows and the worse in the rear part of the pressure side. At this flow regime, the boundary layer appears to be much more sensible to the perturbation introduced by injection as the three higher injection rates already provide values of h/h_{ref} bigger than one. The last condition, in particular, is able to provide better performance only after $S = 45$ [mm] while the second case ($I = 3.81$ / $BR = 2.38$) is able to guarantee the best protection for the majority of the pressure side.

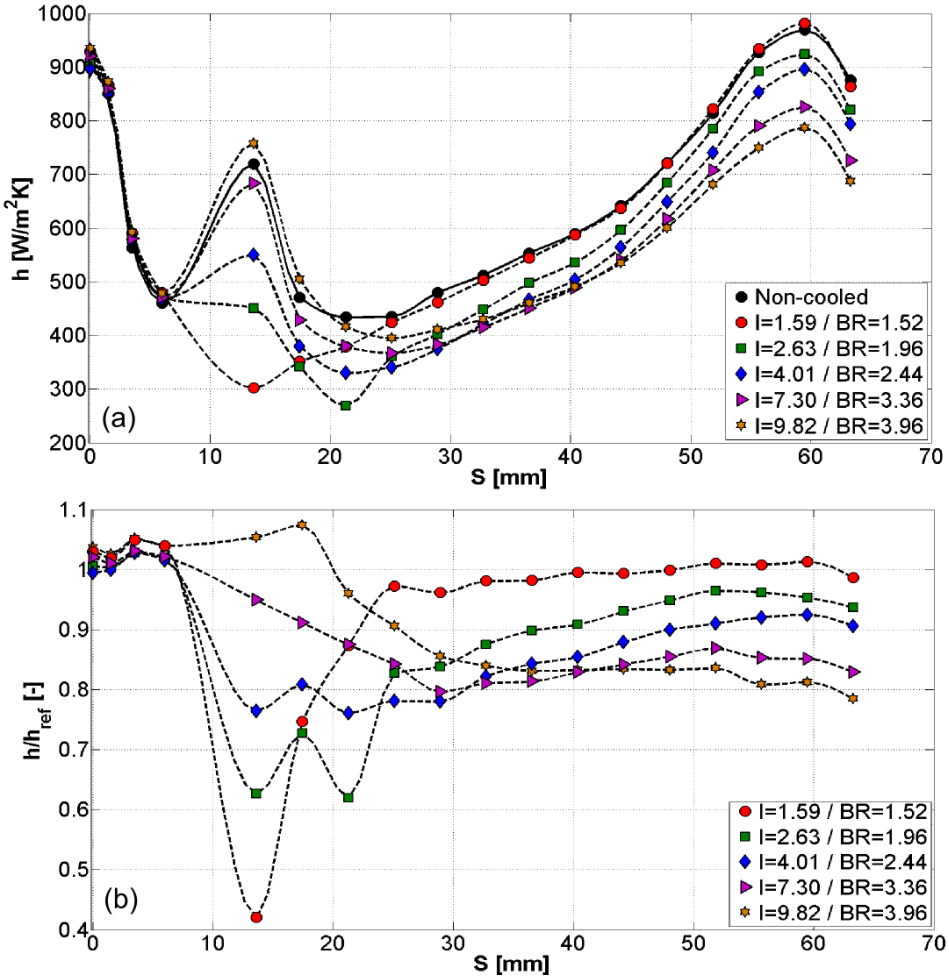

Figure 5.50: Pressure side cooling at $M_{2s} = 0.8$, $Re_{2s} = 1.5 \cdot 10^6$ and $Tu = 5.3\%$: (a)- Evolution of $h[W/m^2K]$ for the pressure side at different injection conditions ; (b)- h/h_{ref} evolution for the suction side at different injection rates, with h_{ref} the non-cooled case distribution

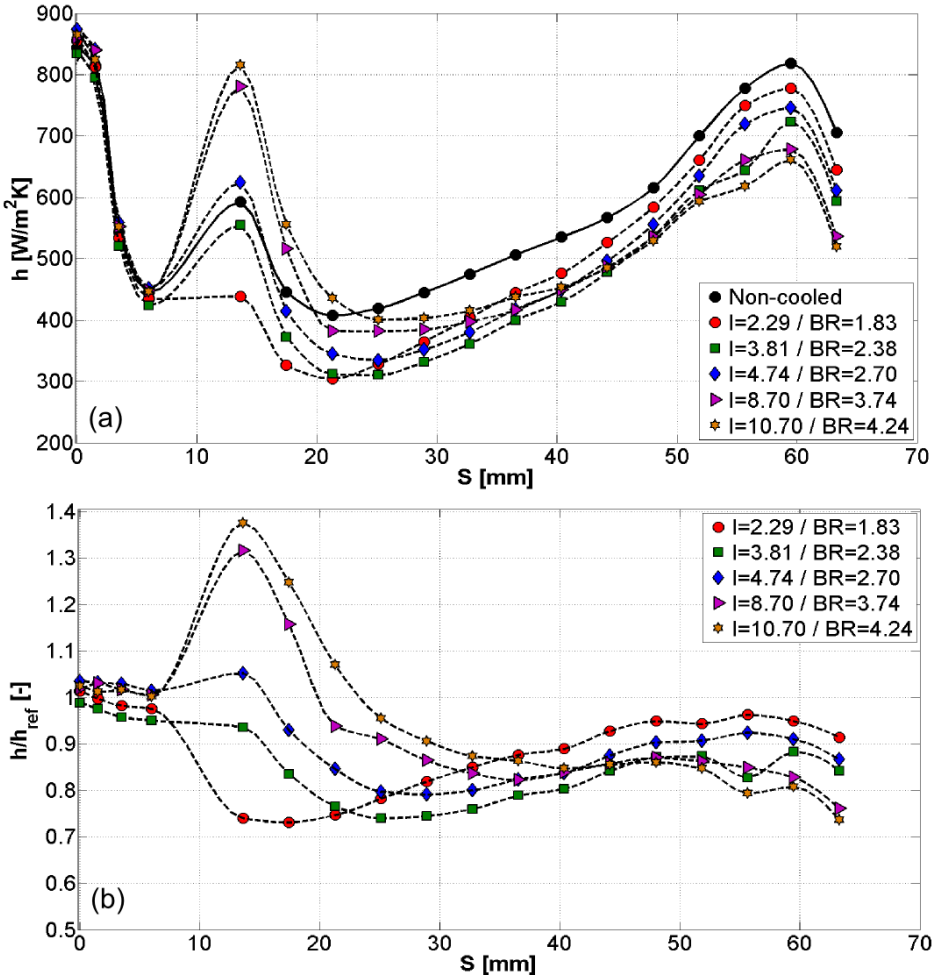

Figure 5.51: Pressure side cooling at $M_{2s} = 1.1$, $Re_{2s} = 1.5 \cdot 10^6$ and $Tu = 5.3\%$: (a)- Evolution of $h[W/m^2K]$ for the pressure side at different injection conditions ; (b)- h/h_{ref} evolution for the suction side at different injection rates, with h_{ref} the non-cooled case distribution

Low temperature coolant

Fig. 5.53(a,b) and Fig. 5.54(a,b) show the evolution of the convective heat transfer coefficient and the ratio h/h_{ref} at $M_{2s} = 0.8$ and $M_{2s} = 1.1$ respectively. Along the pressure side the convective heat transfer coefficient distribution is not particularly affected by the lower temperature of the coolant: values are absolutely comparable with those measured for the tests at ambient conditions. This insensitivity to the temperature of the cooling flow derives from the strong interaction in the proximity of the cooling rows between the cooling jets and the boundary layer: the latter is not able to entrain the high momentum cold coolant that directly passes to the main-stream, providing no further improvement to the protection of the substrate. The discharge coefficient evolution for the two tested Mach numbers is reported in Fig. 5.52 with respect to BR. An asymptotic behaviour towards the chocked condition can be recognized with a maximum difference between the the two distribution of about 1%.

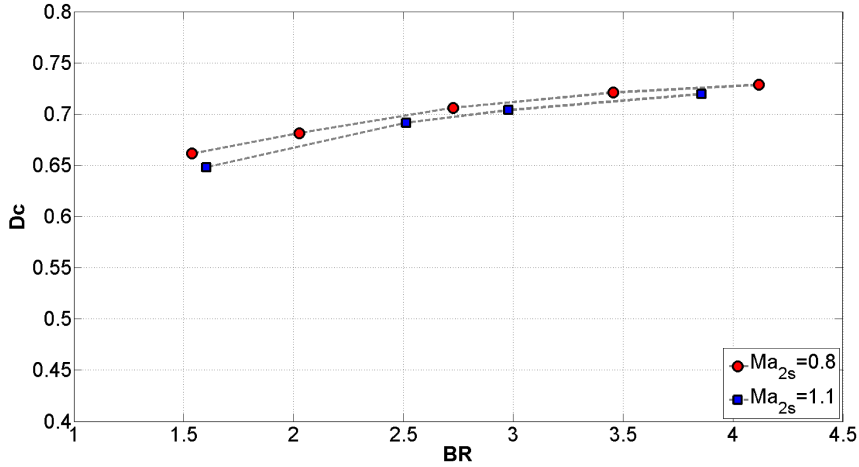

Figure 5.52: Pressure side cooling, low temperature coolant: discharge coefficient evolution with respect to BR at $Re_{2s} = 1.5 \cdot 10^6$ and $Ma_{2s} = 0.8/1.1$ for the low-temperature-coolant tests

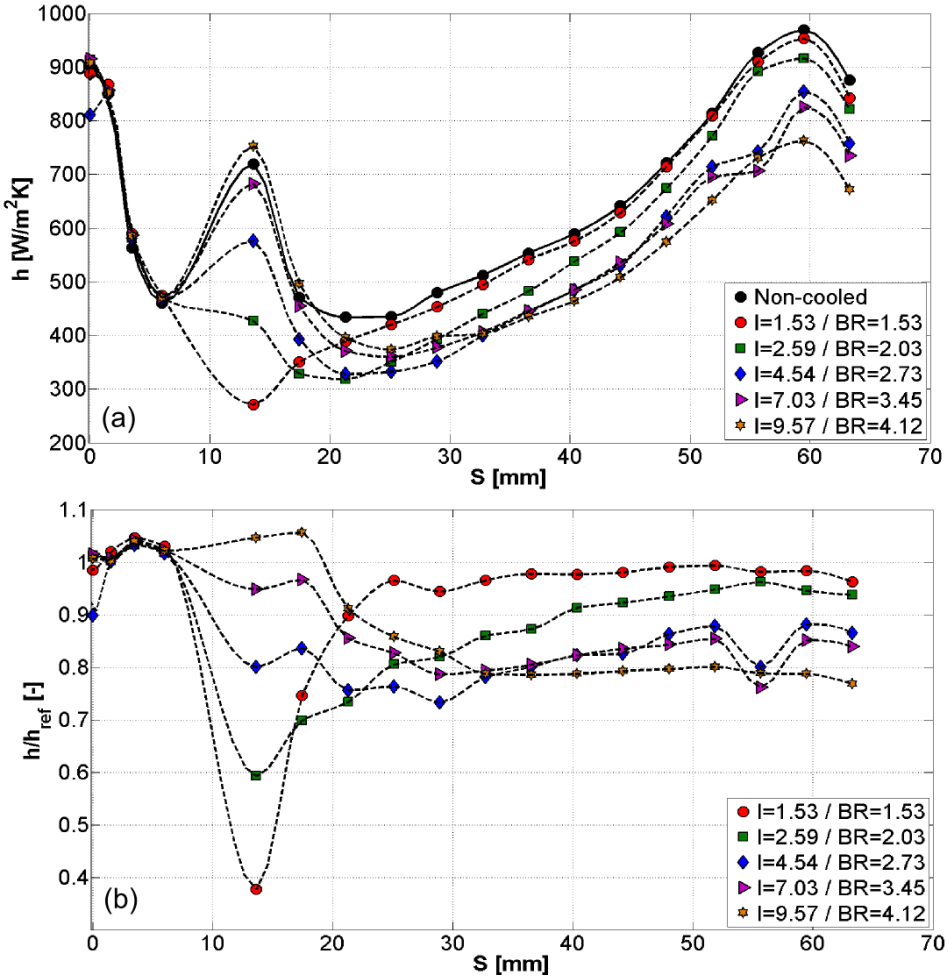

Figure 5.53: Pressure side cooling, low temperature coolant at $M_{2s} = 0.8$, $Re_{2s} = 1.5{\cdot}10^6$ and $Tu = 5.3\%$:(a)- Evolution of $h[W/m^2K]$ for the pressure side at different injection conditions ; (b)- h/h_{ref} evolution for the pressure side at different injection rates, with h_{ref} the non-cooled case distribution

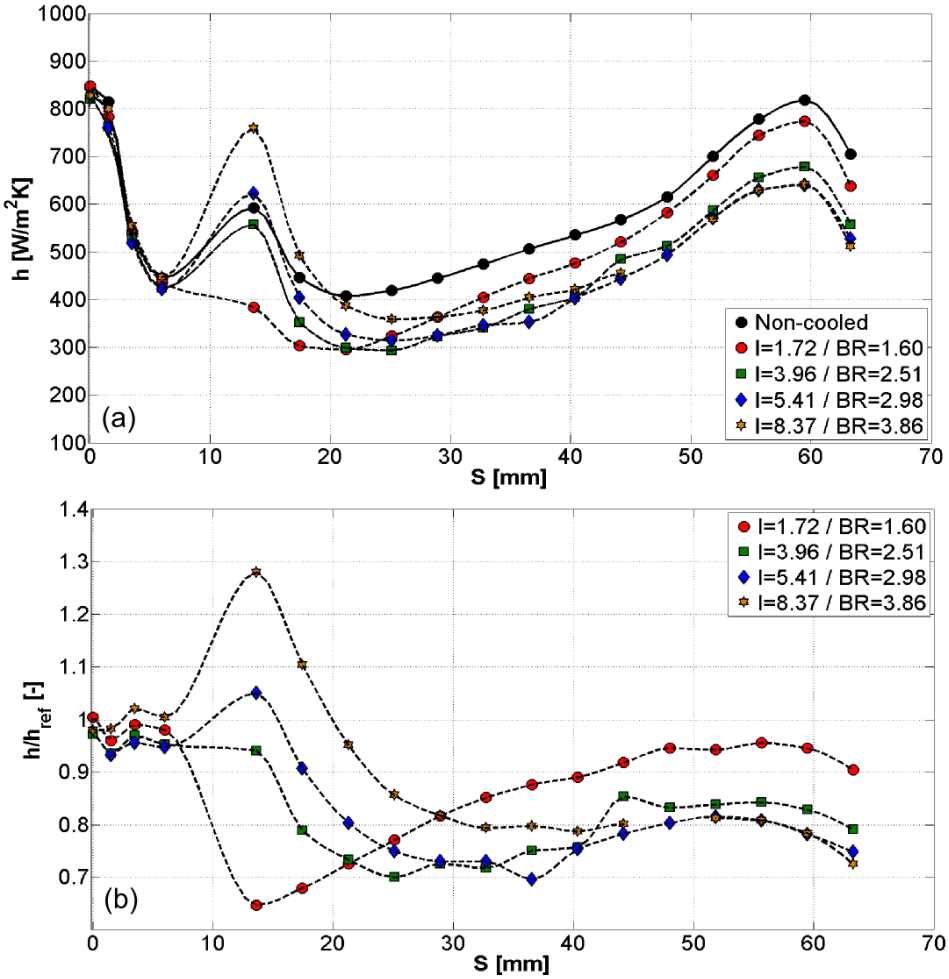

Figure 5.54: Pressure side cooling, low temperature coolant at $M_{2s} = 1.1$, $Re_{2s} = 1.5{\cdot}10^6$ and $Tu = 5.3\%$:(a)- Evolution of $h[W/m^2K]$ for the pressure side at different injection conditions ; (b)- h/h_{ref} evolution for the pressure side at different injection rates, with h_{ref} the non-cooled case distribution

5.9 Uncertainty analysis

The uncertainty analysis presented herein is referred to a 95% confidence interval. When a fitting is used in place of a direct measurement, the fitting error is always taken into account and computed as the standard deviation of a population with respect to the fitted curve. When possible, the data-sheet of the transducer was used to retrieve the uncertainty for directly measured quantities. When this could not be performed, the standard deviation from a typical measurement was used as an indication of the noise level affecting the reading. The uncertainty of derived quantities (e.g. Mach number and Reynolds number) were computed by means of the perturbation method.
At the inlet section, the uncertainty on the temperature measurement was set to be equal to $\delta T_{01} = \pm 0.5$ [K] while the error related to pressure measurements was computed from the variance of the slope value of several calibration curves and found to be approximately equal to ± 10 [mbar]. The lack of precision in the measurement of total and static pressures, leads to an uncertainty in the computation of the inlet Mach number equal to $\delta M_1 = \pm 0.05$, corresponding to more than 30% of the real value. Physical quantities computed from the inlet Mach number (i.e. ρ_1 and T_1) are anyway weakly affected by the uncertainty on M_1: an error of ± 0.05 on the inlet Mach number leads to an uncertainty of $\delta \rho_1 = \pm 0.015$ $[kg/m^3]$ for density and $\delta T_1 = \pm 3$ [K] in the case of the static temperature.
Although static and total temperatures, density and Mach number are all used for the derivation of the instantaneous velocity from hot-wire measurements, in the present analysis the uncertainty on Nu_w was taken to be dependent only on the noise level of the bridge voltage E_b and T_{01}. The latter simplification is well justified by the weak dependency of the Nusselt number on T_1, M_1 and ρ_1 that provides an error at least one order of magnitude smaller than the one deriving from E_b and T_{01}. A computed uncertainty of $\delta Nu_w = \pm 0.02$ when $Nu_w = 7$, implies an error on the fitted Reynolds number of the wire Re_w equal to 2.8% of the value which, in turn, produces an uncertainty on the velocity slightly higher than 3% of the mean.

Downstream total pressure P_{02} and flow angle β_2 vary along the traversing plane as pressure levels differ between the center of the channel and the wake region. Uncertainties have been therefore computed for every position of the probe and their distribution in the pitch-wise direction was investigated. The analysis takes into account the uncertainty of pressure transducers (0.25% of full span) as well as of the iterative procedure that computes the previously cited quantities (angular calibration).
Fig. 5.55 (a) reports the evolution of the uncertainty for the downstream flow angle $\delta\beta_2$ with respect to Ma_{2s}. A variation of the flow conditions seems to not affect at all the error on the evaluation of β_2 that keeps constantly equal to ± 0.16 [°]. The uncertainty on the computation of the downstream total pressure δP_{02} is given in percentage of the mass averaged value $\widehat{P_{02}}$ and presented in Fig. 5.55 (b). Even though it is impossible to recognize a dependency of the error on Ma_{2s}, it is clearly evident that values keep always smaller than the 2% for every flow condition.

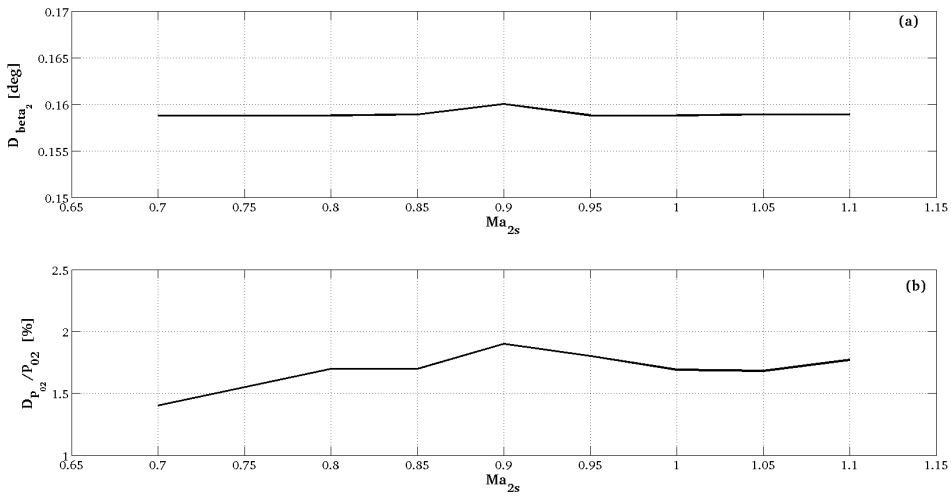

Figure 5.55: Uncertainty dependency on the downstream isentropic Mach number: (a) for downstream flow angle ; (b) for downstream total pressure

The error on the computed loss coefficient ζ depends on P_{02}, P_{01} and P_2 and tends to decrease when increasing the discharge isentropic Mach number. It decreases linearly from $\delta\zeta = \pm 0.32\%$ at $Ma_{2s} = 0.8$ ($\zeta = 3\%$) to $\delta\zeta = \pm 0.19\%$ at $Ma_{2s} = 1.1$ ($\zeta = 5.5\%$). The main source of uncertainty for the latter parameter is given by the poor performance of the transducer measuring P_{01} (as discussed above) and secondly by the uncertainty on P_{02}. The uncertainty related to the thermodynamic loss coefficient ζ_c^* is computed for all the injection conditions at $Ma_{2s} = 0.8$ and $Re_{2s} = 10^6$. It is a function of T_{01}, P_{01}, P_{02}, P_2, the coolant total pressure P_{0c} and temperature T_{0c} and the coolant mass-flow $\dot{m}_c$. The latter parameter is known within an uncertainty of $\pm 0.4\%$ of the total coolant mass-flow computed for the worst condition (lowest P_{0c}/P_{01}). The error related to the thermodynamic loss coefficient therefore varies only slightly with the different injection pressures and is equal to $\delta\zeta_c^* = \pm 0.26\%$ for $\zeta_c^* = \pm 2.5\%$.
The error analysis for the convective heat transfer distribution was performed for the thin-film placed at the leading edge and in the worst condition (lowest Reynolds number). It takes into account the uncertainty on wall temperature measurements $\delta T_w = \pm 0.5$ [K], the uncertainty on T_{01}, the error committed on the measurement of the initial temperature $\delta T_i \pm 0.5$ [K] and the uncertainty on the characteristics of the substrate $\delta\sqrt{\rho c K} = 3\%$. The latter parameter is the highest contribution to the error committed on h that was found to be as big as the 6.8% of the measured value.

5.10 Summary of the measurement campaign

The lack of a reliable and complete experimental test case for Turbomachinery codes validation was the motivation for two different measuring campaigns carried out at VKI and whose results were published in the technical note TN-174 [6], in the journal paper [5] and in occasion of the lecture series LS-94 [4]. The first contribution provided a complete characterization of the highly loaded transonic turbine vane LS-89 while the second work focused on the wall heat-transfer distribution of the film-cooled version of

the blade, the LS-94.

The present campaign, configured as a follow up of the previously cited works, investigated the LS-94 geometry with the intent to complement the dataset already present by characterizing the free stream inlet turbulence and the aerodynamic performance with and without injection of cooling flow, in order to obtain a complete experimental test case for numerical codes validation.

The model consisted of a five blades linear cascade tested in the VKI CT-2 facility. The test section was designed to carry "*on board*" the inlet and outlet boards as well as the entire coolant feeding system. Endwalls were also equipped with a rack of wall pressure taps and a slit in the downstream section in order to provide the static pressure distribution and to traverse a pneumatic 3-holes probe.

Inlet turbulence was assessed by means of hot-wire anemometry. A novel calibration technique developed by Cukurel [7] was implemented because it demonstrated to provide stable and reliable calibration curves, independent from temperature fluctuations during the tests. Turbulence intensity was varied by means of a turbulence generator shifted at four different positions upstream of a fixed hot-wire probe.
Turbulence spectra (PSD) were retrieved at each position of the grid, showing a decreasing content of energy as the turbulence generator was shifted further upstream. The typical slopes of turbulence ("-1","-5/3","-3" and "-7",) could be partially recognized.
Turbulence intensity (Tu), turbulent kinetic energy (K) and decay rate (ϵ) all showed a trend in complete accordance with literature: they all decrease as the grid is shifted further upstream. Moreover, the exponent of the fitted power-laws for K matched with what reported by Valente et. al [56] for grid-generated turbulence.
The integral length scale (L_1) and the Taylor's length scale were found to follow the expected trend: they increased as the turbulent kinetic energy decreases, following the mechanism of decay. In particular, the power-law

exponent for L_1 was found to completely agree with what published by Valente et al. [56].

The aerodynamic performance of the cascade was assessed by traversing a pneumatic pressure probe in the downstream section. Measurements have been all dynamically compensated and, when needed, a bow-shock correction was also applied for supersonic flow fields.
The non-cooled cascade presented higher losses than those measured by Arts et al. [6] on the LS-89. This degradation in efficiency was related to the existence of the two rows of cooling holes on both, the suction and the pressure sides. Losses increased as the flow regime was augmented up to a value of $Ma_{2s} = 1$ where a drastic variation in the slope led to values up to 40% higher than those in subsonic conditions. This is due to the setting up of strong shocks in the blade channel: as soon as the flow regime got to a supersonic condition, total pressure wakes widened and shifted towards the suction side. The effect of the Reynolds number was found to affect only the measured flow angle in the downstream section, providing a higher turning at high Reynolds numbers.

The cooling system for the suction side was characterized at $Re_{2s} = 1.5 \cdot 10^6$ at different exit isentropic Mach numbers. The global discharge coefficient (Dc) increased asymptotically to the chocked value when the mass-flux ratio BR increased, being independent on Ma_{2s}. A comparison was also made at a subsonic flow condition between $Re_{2s} = 1.5 \cdot 10^6$ and $0.5 \cdot 10^6$, showing that Dc values reduced because of the effect of both, the density ratio and a different evolution of the boundary layer.
Total pressure wakes showed a moderate widening towards the suction side when injection took place and only in subsonic condition. Therefore, to better visualise the effect of injection, a new loss coefficient ζ_c^* was defined with respect to the main-stream chocked mass-flow. Losses presented in general a minimum at $BR = 0.5 - 0.6$ with a following linear increase up to values about 50% higher for the last injection condition. The downstream flow angle seemed to be not affected at all.

The pressure side cooling system showed Dc values 5% higher than those for the suction side at $Re_{2s} = 1.5 \cdot 10^6$. The Mach number variation did not affect at all the distributions that were presenting a typical asymptotic trend. An increase in terms of Reynolds number was found to enhance the injection process by providing higher discharge coefficients.
In a subsonic condition, pressure wakes became stronger when injection took place, with a moderate widening in the pressure side region only for the lowest injection condition. At a supersonic regime it was impossible to experience injection-induced effect. Losses increased almost linearly with BR while the downstream exit angle β_2 was not affected at all by the injection rate.

The convective heat transfer coefficient distribution along the blade surface was assessed by means of a transient measurement technique. Tests were run at $Re_{2s} = 1.5 \cdot 10^6$ and $Tu = 5.3\%$ for two downstream isentropic Mach numbers, $Ma_{2s} = 0.8$ and $Ma_{2s} = 1.1$ respectively. Cooled tests were performed at two different coolant temperatures, at ambient temperature and at about $265[K]$. An increase of the injection rate always led to a better protection of the suction side with respect to the non-cooled case for both the tested Mach numbers. Immediately downstream the injection rows, the highest injection condition showed anyway a worse protection: the coolant momentum was high enough to increase the turbulent mixing inside the boundary layer leading therefore to an enhancement of the heat flux towards the surface and, consequentially, of the convective heat transfer coefficient. The pressure side boundary layer was much more affected by injection than the suction side. Right downstream the injection rows, a small increase of the injection rate led to values of h higher than those measured for the non-cooled case. This was due to the fact that the momentum of the cooling jets was so high that jets were able to *drill* the boundary layer, making the surface of the substrate accessible to hot main-stream flow. The rear part of the pressure side anyway benefited from injection and the heat transfer coefficient tended always to diminish as injection is further enhanced.

Chapter 6

Conclusions

The present thesis critically addresses two distinct but complementary experimental investigations on typical film-cooled-high-pressure turbine geometries. The measurement campaigns aimed to provide an enhanced understating of the phenomenology of the flow field generated by these turbomachinery components while providing, at the same time, an accurate experimental benchmark for an in-depth validation of numerical codes.
A particular attention was devoted therefore to the the characterization of the cascade inlet flow, in order to clearly identify its effect on the global performance, as well as to provide a complete and detailed set of measurements of the quantities which set the boundary conditions of any numerical simulation. In particular, the inlet free-stream turbulence was deeply investigated by measuring the evolution of the turbulence intensity, the turbulent kinetic energy and decay along the inlet channel and by computing the typical scales of turbulence as well as its spectrum. If, on one hand, the knowledge of these quantities allows for a more complete understanding of the aero-thermal performance of the cascade, on the other hand it also provides a complete dataset for a critical review of the turbulence models which are implemented in the modern codes.
The performance of the cascade was necessarily assessed by coupling the

aerodynamic and the thermal fields characterization. Extensive comparisons have been produced between the aerodynamic loss distribution and the heat load of the profile, in order to precisely describe the state of the boundary layer and to link it with the overall aerodynamic efficiency.
The same type of comparisons was extended to the investigation of the effects of film-cooling on both the aerodynamic and the thermal performance, at different injection rates and coolant temperatures. In every condition, the film-cooling system was fully characterized by measuring the coolant local conditions at the injection point as well as by providing the coolant global parameters.
The production of an experimental dataset for the validation of numerical codes necessarily implies a critical reexamination of the measurement techniques adopted in the frame of the investigation in quest of an enhanced accuracy of the measured data. The latter requirement deals, at first instance, with the definition of the sources of measurement errors and with the adoption of efficient strategies for their reduction. According to this need, a recent calibration and data-reduction procedure was applied to hot-wire measurements for turbulence characterization which actually allowed to obtain accurate velocity measurements by getting rid of the effect of the flow temperature. Another example of the importance given to the accuracy of the measurements, is the dynamic calibration of the pressure probe used for the aerodynamic characterization of the cascade: in order to compensate for the natural damping/delay of such a pneumatic system, every measurement was dynamically compensated in the frequency domain.
Any measurement cannot be considered as accurate if its uncertainty is not stated. In the frame of the present work, a severe and well documented uncertainty analysis was carried out for every measurement and every derived parameter.

The detailed experimental characterization of the inlet flow, the extensive aero-termal investigation of the flow field downstream the cascades and the efforts made to maximize as much as possible the accuracy of the measurements, provide all together a clear and robust insight into the phenomenology of the flow in typical film-cooled-high-pressure turbine com-

ponents and guarantee, at the same time, the availability of an accurate and comprehensive experimental test-case contributing to the validation of advanced numerical codes.

Appendices

Appendix A

Effect of the regression method applied to hot-wire measurements

In the present section, the effect of the regression procedure applied to hot-wire measurements presented in Sec. 5.5 is investigated in terms of mean flow parameters as well as turbulent quantities.
As shown in Fig. A.1 the averaged inlet Reynolds number (Re_1) varies slightly when the regression method is applied, completely preserving the order of magnitude and therefore its effect on turbulent quantities. The averaged isentropic downstream Mach number (Fig. A.2) seems instead to be not affected at all: for every test, the values of Ma_{2s} computed with and without the regression approach show a negligible variation.
By applying the regression method also the turbulent intensity is very slightly affected: at every location of the grid, the Tu computed value undergoes to a variation that keeps smaller than 0.5% as presented in Fig. A.3.
What is instead showing the highest impact of the regression procedure are the spectra of turbulence. Fig. A.4 reports a comparison of the two approaches for the 3.9% turbulent intensity case: even though the original data spectrum appears to be only a little noisier at low frequency range,

evident discrepancies appear at about 10 [kHz]. A new peak appears at 13 [kHz] while, above 15 [kHz], the spectrum clearly reduces its slope, resulting therefore in higher values than for the regressed spectrum. The applied procedure demonstrated therefore to be able to tackle correctly the mean flow behaviour as well as to respect the main turbulent quantities. On the other hand it greatly increases the legibility of the spectrum in the high frequency range, highlighting a behaviour that was completely hidden by the noise content of the non-regressed case.

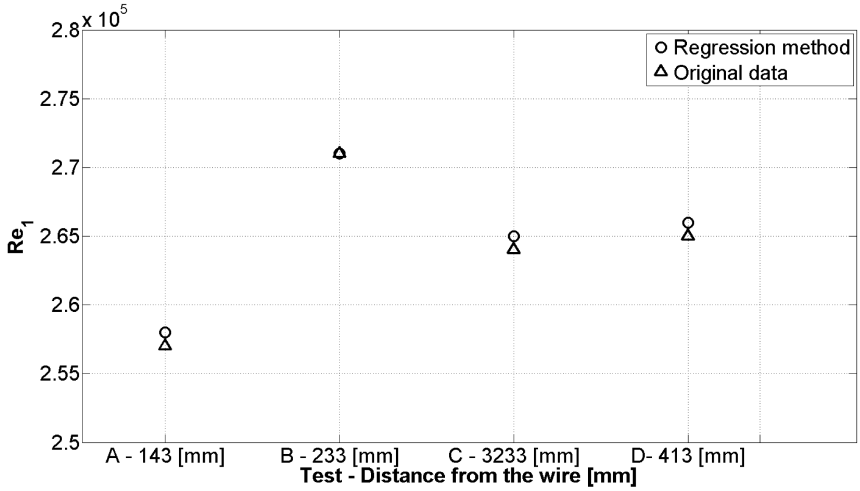

Figure A.1: Inlet averaged Reynolds number (based on blade chord) with and without regression method

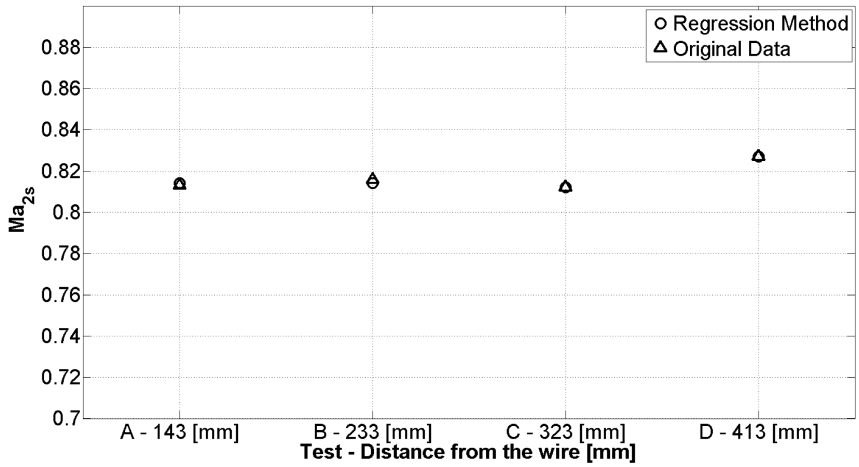

Figure A.2: Downstream averaged isentropic Mach number computed with and without regression method

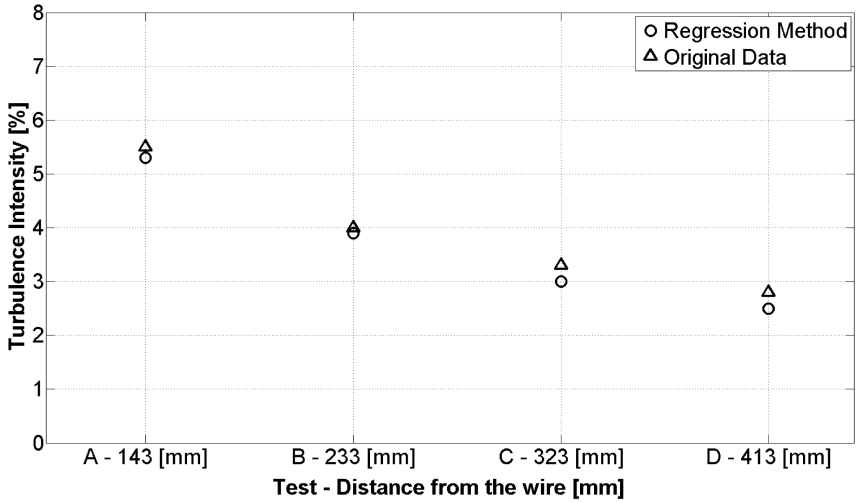

Figure A.3: Computed turbulence intensity for the original and regressed data

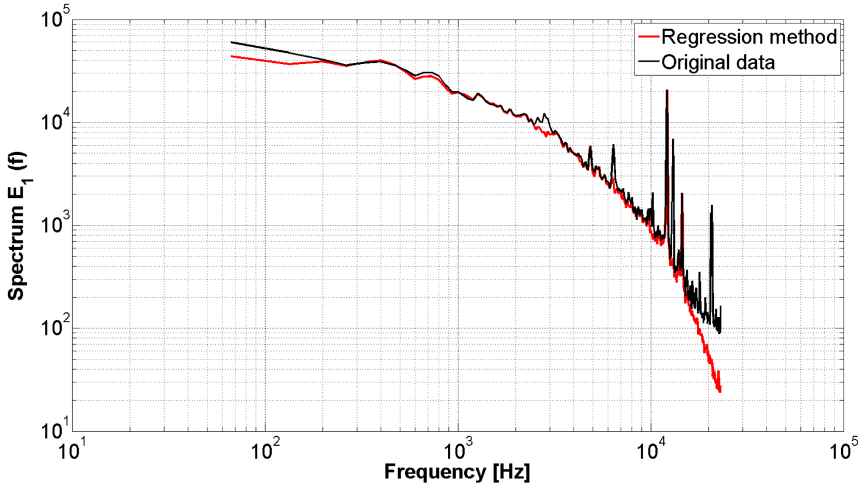

Figure A.4: Power spectral density before and after the application of the regression method

Appendix B

Dynamic calibration of a pneumatic pressure probe: data processing in the frequency domain

As mentioned Sec. 3.1.3, a pressure step excites all the frequencies of the system but with an equal amount of energy. This produces a particularly noisy spectrum that necessarily requires an averaging procedure over different time records: in the present application, the TF of the 3-hole probe was computed by averaging the spectra of 12 different bursts of the balloon. Moreover, it has to be remarked that the phase distribution corresponds to the delay with respect to the first point of the spectrum. In presence of an imperfect trigger, the acquisition starting point could vary from test to test, producing a different phase pattern in the low frequency range. When averaging the different spectra, a mean value among all the signals is computed that leads to the loss therefore of any possible deterministic oscillations of the phase (Fig. B.1-a). The resulting TF will be therefore necessarily misleading and the reconstructed signal non-physical. To avoid this kind of artefacts, the time series have been shifted with respect to a known unequivocal point (e.g. the half-step point) before transforming

them in the frequency domain. The result, presented in Fig. B.1-b, shows is fact a well organized distribution of the TF phase, with a drastic reduction of the degree of randomness at low frequencies.

Since the sampling rate could be varied from the one adopted during the dynamic calibration, steps have been acquired at a high frequency (1 [MHz] - much higher than the cut-off frequency of the probe itself) in order to allow the re-sampling of the calibration time series to match the maximum spectrum frequency. A low-pass Butterworth filter set to the half of the re-sampling frequency has been always applied to avoid any aliasing artefact. The acquisition time of a record determines the spectral resolution of its Fourier Transform and the best practice would be in fact to guarantee that the data to be compensated are acquired over the same observation time, to exactly match the spectral resolution. When dealing with the burst of a balloon, this is almost impossible to obtain (because of the short characteristic time of the phenomenon) and therefore a different way has to be followed. In the present work, each time series was elongated by adding blocks of the first portion of the record at the beginning of the time series and blocks of the last data at its end, providing to increase the two sides of the signal with the same quantity of points. This process produces a high resolution TF that can be interpolated locally in the complex domain when the spectral resolution of the compensated signal is not precisely corresponding.

Windowing of the signal is mandatory. The high frequency components introduced by the FFT to approximate the non-periodicity of the step signal critically affect the quality of the reconstruction. Thus, a custom window was created as shown by Fig. B.2: a common Hanning window was split in two symmetric parts and as many unitary values as needed to match the length of the data vector were added among them.

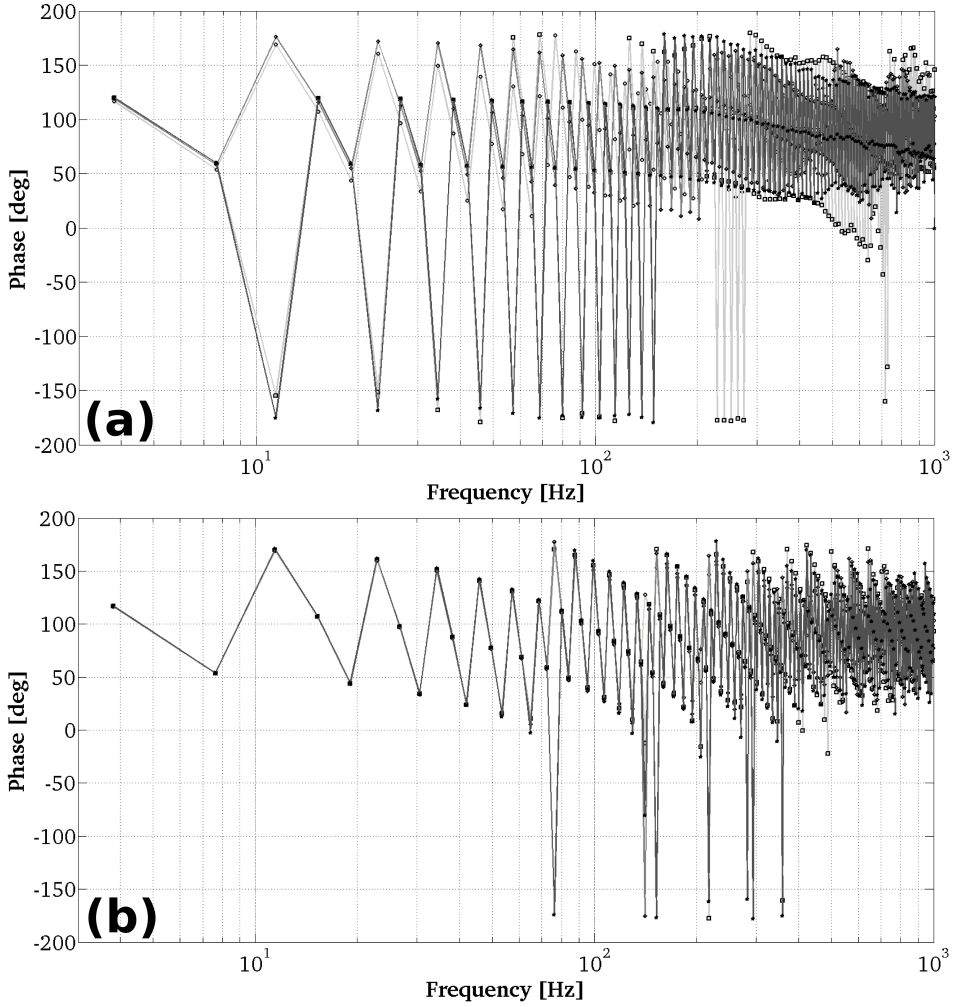

Figure B.1: Comparison among 4 different records of the same phenomenon before (a) and after (b) re-phasing with respect to the half step point

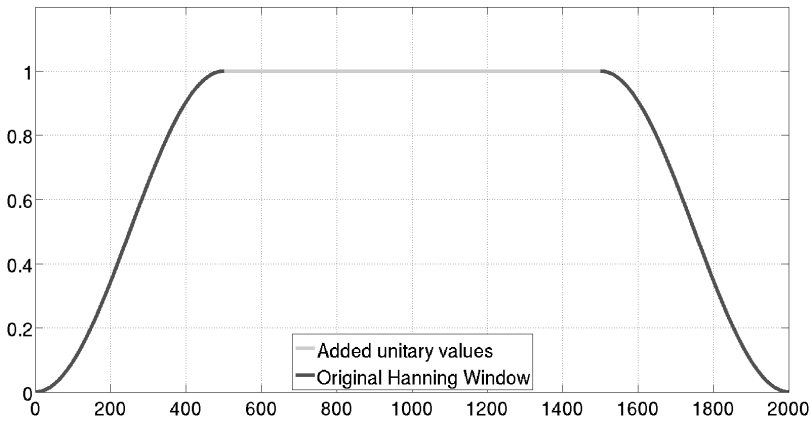

Figure B.2: Custom Hanning window

Appendix C

Quality of the dynamic compensation of pneumatic pressure probe measurements

Before submitting the data to the angular calibration process, the natural damping-delaying behaviour of the pneumatic total pressure probe was compensated by means of the dynamic calibration described in section 3.1.3. The quality of this correction can be verified in Fig. C.1 and Fig. C.2 where total pressure wakes and flow angles raw traverses are plotted together with the compensated counterparts and a series of measurements acquired by fixing the probe in several points along the traversing path.
As clearly visible, the compensated signal matches perfectly with the reference measurements, demonstrating that the dynamic calibration of the piping system allowed to retrieve the genuine pressure levels and angles of the flow field. Given the demonstrated effectiveness of the correction, all the downstream pressure probe measurements have been dynamically compensated.

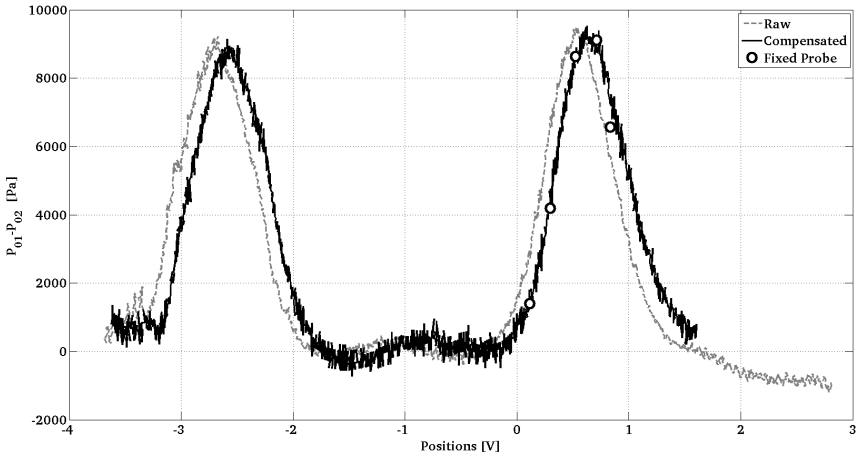

Figure C.1: Quality of the dynamic compensation: total pressure wakes before compensation, after compensation and fixed-probe measurements

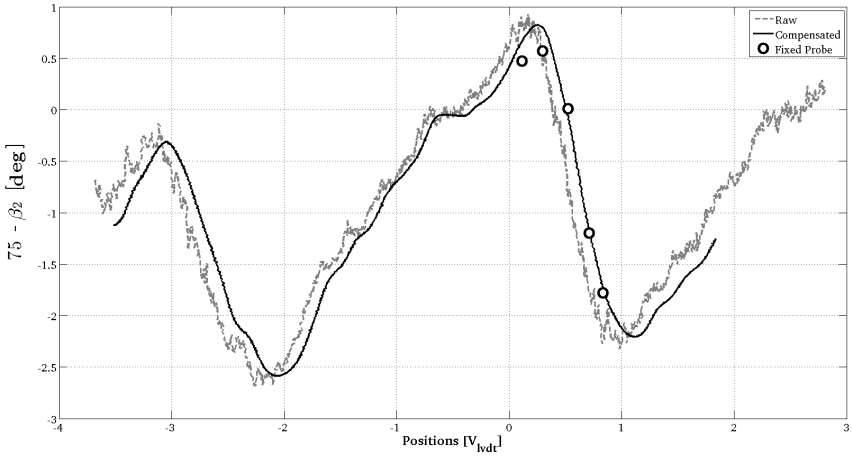

Figure C.2: Quality of the dynamic compensation: flow angle before compensation, after compensation and fixed-probe measurements

Appendix D

Validity of the assumptions taken in the applied bow-shock correction procedure

As mentioned already in section 3.1.4, when the flow regime is supersonic, a bow-shock is created in front of the head of the probe that leads to misleading pressure measurements. In order to correct for this effect and therefore to retrieve the true pressure value, the static undisturbed pressure has to be known. By analysing the same type of contour plot of the one presented in the latter section for a supersonic flow condition, one can retrieve the magnitude of the effect that the shock has on the static pressure. Given that in Fig. D.1 the distribution of $P_{2_{traversing}} - P_{2_{notraversing}}$ keeps generally close to zero at every location of the probe trajectory, no effect can be addressed to its presence. Hence, P_2 distribution can be always considered as representative of the undisturbed flow-field and can be therefore used to retrieve the true total pressure by means of equations 3.9 and 3.10. When, therefore, the ratio between P_2 and P_{02} becomes smaller than the critical value ($(P_2/P_{02})_{crit} = 0.5283$), the bow-shock correction is automatically applied by considering the local static pressure as representative of the one

upstream the shock. The corrected local total pressure and Mach number can be therefore retrieved.

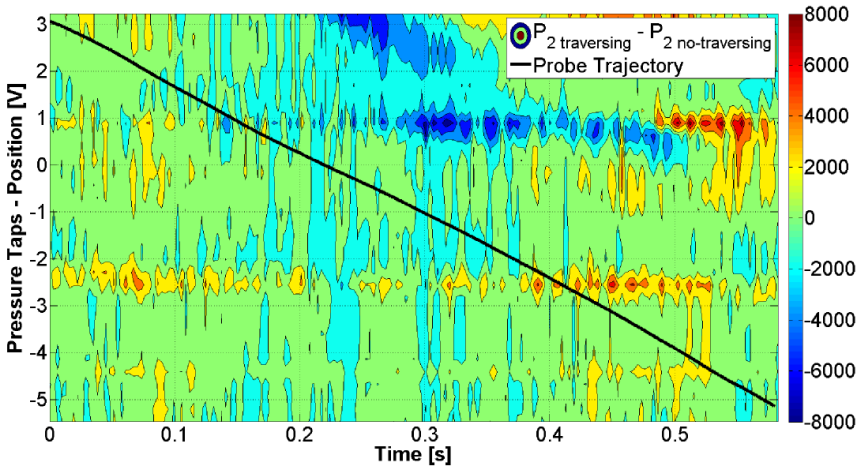

Figure D.1: $P_{2_{traversing}} - P_{2_{traversing}}$ versus the probe trajectory for $Ma_{2s} = 1.1$

Appendix E

Effect of the presence of the probe

The presence of the probe in the flow field could drastically affect its pattern (e.g. blockage effect), leading to inconsistent and misleading results. To verify that the presence of the probe had no impact on the natural behaviour of the flow, the downstream static pressure distribution with and without traversing were compared for a sub-sonic case. Figure E.1 reports the difference between the downstream wall static pressure distribution measured during a traversing of the probe and the one without the probe in the flow field. In abscissa the time coordinate is reported, while the ordinate axis corresponds to the position of the static wall taps expressed in terms of voltages of the LVDT measuring the displacement of the probe. This allows therefore to superimpose to the pressure contour plot the trajectory followed by the device during the traversing (dotted line in E.1). Given the random and almost null distribution in proximity of the probe trajectory, it is impossible to recognize any deterministic effect addressable to the presence of the head of the probe at a certain location: the downstream static pressure distribution seems to be not affected at all.

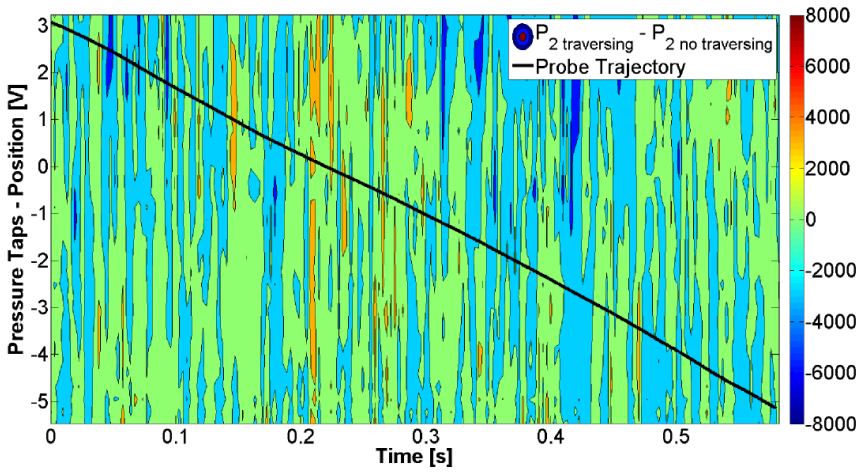

Figure E.1: $P_{2_{traversing}} - P_{2_{notraversing}}$ versus the probe trajectory for $Ma_{2s} = 0.8$

Appendix F

Ls-94 transonic turbine vane: thin-films gages coordinates

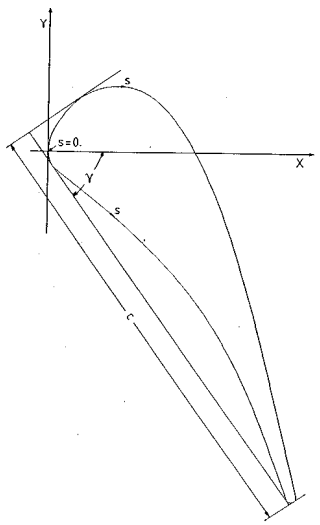

Figure F.1: Thin-films gages coordinates frame of reference

Suction Side

X [mm]	Y [mm]	S [mm]
0	0	0
0.177	1.511	1.521
0.787	3.393	3.506
2.132	5.493	6.002
4.444	7.981	9.41
14.078	8.997	19.631
16.796	6.954	23.042
18.986	4.36	26.441
20.835	1.498	29.849
22.446	-1.509	33.261
23.866	-4.597	36.661
25.157	-7.752	40.07
26.326	-10.954	43.479
27.387	-14.185	46.88
28.379	-17.445	50.287
29.323	-20.724	53.7
30.224	-24.001	57.098
31.082	-27.303	60.51
31.914	-30.612	63.922
32.725	-33.923	67.331
33.523	-37.228	70.731
34.324	-40.542	74.14
35.125	-43.855	77.549
35.924	-47.16	80.949
36.726	-50.476	84.36

Pressure Side

X [mm]	Y [mm]	S [mm]
0.353	-1.471	1.514
1.651	-2.948	3.5
3.604	-4.511	6.001
9.496	-9.373	13.641
12.337	-11.926	17.46
15.093	-14.569	21.279
17.733	-17.333	25.102
20.206	-20.24	28.919
22.494	-23.301	32.741
24.584	-26.495	36.559
26.49	-29.806	40.38
28.224	-33.21	44.2
29.806	-36.684	48.018
31.256	-40.221	51.841
32.609	-43.793	55.66
33.926	-47.378	59.48
35.242	-50.963	63.299

Bibliography

[1] *Preliminary measurements of velocity, density and total temperature fluctuations in compressible subsonic flow* (Jan. 1983).

[2] Abdullah, N., Talib, A. R. A., Jaafar, A. A., Salleh, M. A. M., and Chong, W. T. The basics and issues of thermochromic liquid crystal calibrations. *Experimental Thermal and Fluid Science 34*, 8 (2010), 1089 – 1121.

[3] Albert, J., Bogard, D., and Cunha, F. Adiabatic and overall effectiveness for a film cooled blade. In *Proceedings of the 2004 International Joint Power Generation Conference* (2004), ASME.

[4] Arts, T. Highly Loaded Transonic and Film Cooled Linear Turbine Guide Vane Cascade LS94. In *VKI LS 94-06 - Numerical Methods in Turbomachinery* (1994).

[5] Arts, T., and De Rouvroit, M. L. Aero-thermal performance of a two-dimensional highly loaded transonic turbine nozzle guide vane: A test case for inviscid and viscous flow computations. *Journal of turbomachinery 114*, 1 (1992), 147–154.

[6] Arts, T., Rutherford, A., and De Rouvroit, M. Aero-thermal investigation of a highly loaded transonic linear turbine guide vane cascade. Tech. rep., Von Karman Institute for Fluid Dynamics, 1990.

[7] B. Cukurel, S. Acarer, T. Arts. A novel perspective to high-speed cross-hot-wire calibration methodology. *Experiments in Fluids 53* (2012), 1073–1085.

[8] Baldauf, S. a., Scheurlen, M., Schulz, A., and Wittig, S. Correlation of film-cooling effectiveness from thermographic measurements at enginelike conditions. *Journal of turbomachinery 124*, 4 (2002), 686–698.

[9] Blair, M. An experimental study of heat transfer and film cooling on large-scale turbine endwalls. *Journal of Heat Transfer 96* (1974), 524.

[10] Bradley, R. G., Bhateley, I. C., and Howell, G. A. Computational fluid dynamics: Transition to design applications. In *Supercomputing in Aerospace* (Mar. 1987), pp. 69–76.

[11] Bruun H.H. *Hot-Wire Anemometry.* Oxford Science Publications, 1995.

[12] Bunker, R., and Arts, T. *Film cooling science and technology for gas turbines: state-of-the-art experimental and computational knowledge.* Von Karman Institute for Fluid Dynamics, 2007.

[13] Cresci, R.J.; Librizzi, J. Transpiration cooling of a turbulent boundary layer in an axisymmetric nozzle. *AIAA Journal 2* (1964), 617–624.

[14] Cutbirth, J., and Bogard, D. Thermal field and flow visualization within the stagnation region of a film-cooled turbine vane. *Journal of turbomachinery 124*, 2 (2002), 200–206.

[15] Cutbirth, J., and Bogard, D. Effects of coolant density ratio on film cooling performance on a vane. In *Proceedings of the 2003 International Joint Power Generation Conference* (2003), ASME.

[16] D., P. A review of rgb color spaces: from xyy to rgb. *Babel Color* (2003).

[17] D. Olivari, C. Benocci . *CN 157 - Introduction to Mechanism of Turbulence*. von Karman Institute, 2010.

[18] Denton, J. Loss mechanisms in turbomachines. *Journal of Turbomachinery;(United States) 115*, 4 (1993).

[19] Doerffer, P., and Amecke, J. Secondary flow control and streamwise vortices formation. *ASME Paper 94* (1994).

[20] Drost, U., and Blcs, A. Investigation of Detailed Film Cooling Effectiveness and Heat Transfer Distributions on a Gas Turbine Airfoil. In *Proceedings of the ASME Turbo Expo 1998 Conference* (1998), no. 20 in 98-GT.

[21] Drost, U., and Blcs, A. Performance of a Turbine Airfoil with Multiple Film Cooling Stations - Part II : Aerodynamic Losses. In *Proceedings of the ASME Gas Turbine & Aeroengine Congress & Exhibition* (1999), no. 171 in 99-GT.

[22] Dunham, J. CFD Validation for Propulsion System Components. Tech. rep., AGARD, 1998.

[23] Fernando López Peña. *Aerodynamic Aspects of Film Cooling*. von Karman Institute, 1992.

[24] Fitt, A., Ockendon, J., and Jones, T. Aerodynamics of slot-film cooling - Theory and experiment. *Journal of Fluid Mechanics 160* (Nov. 1985), 15–27.

[25] Forth, C. J. P., and Jones, T. V. Scaling parameters in film-cooling. In *Heat transfer 1986; Proceedings of the Eighth International Conference* (1986), C.-L. Tien, V. P. Carey, and J. K. Ferrell, Eds., pp. 1271–1276.

[26] Friedrichs, S., Hodson, H., and Dawes, W. Distribution of film-cooling effectiveness on a turbine endwall measured using the ammonia and diazo technique. *Journal of turbomachinery 118*, 4 (1996), 613–621.

[27] Friedrichs, S., Hodson, H., and Dawes, W. Aerodynamic aspects of endwall film-cooling. *TRANSACTIONS-AMERICAN SOCIETY OF MECHANICAL ENGINEERS JOURNAL OF TURBOMACHINERY 119* (1997), 786–793.

[28] Friedrichs, S., Hodson, H., and Dawes, W. The design of an improved endwall film-cooling configuration. *TRANSACTIONS-AMERICAN SOCIETY OF MECHANICAL ENGINEERS JOURNAL OF TURBOMACHINERY 121* (1999), 772–780.

[29] G. K. Batchelor. *The Theory of Homogeneous Turbulence*. Cambridge University Press, 1953.

[30] Goldstein, R., Eckert, E., and Burggraf, F. Effects of hole geometry and density on three-dimensional film cooling. *International Journal of Heat and Mass Transfer 17*, 5 (1974), 595 – 607.

[31] Gregory-Smith, D. Test case 3: Durham low speed turbine cascade. In *ERCOFTAC seminar and workshop on 3D turbomachinery flow prediction II (Val dIsère) Part* (1994), vol. 3, pp. 96–109.

[32] Gregory-Smith, D., Graves, C., and Walsh, J. Growth of secondary losses and vorticity in an axial turbine cascade. *Journal of turbomachinery 110*, 1 (1988), 1–8.

[33] Gunston, B. *Jane's: Aero-engines*. Jane's Information Group, 2005.

[34] H. Bergh, H. Tijdeman. Theoretical and Experimental Results for the Dynamic Response of Pressure Measuring Systems. NLR-TRF 328, Dutch National Aero and Astronautical Research Institute, 1965.

[35] H. Tennekes and J. L. Lumley. *A First Course in Turbulence.* The MIT Press, 1972.

[36] Han, S., and Goldstein, R. Influence of blade leading edge geometry on turbine endwall heat (mass) transfer. *Journal of turbomachinery 128*, 4 (2006), 798–813.

[37] Harrison, K. L. *Computational and Experimental Study of Film Cooling Performance Including Shallow Trench Configurations.* PhD thesis, University of Texas at Austin, 2006.

[38] Hirsch, C. CFD methodology and validation for turbomachinery flows. In *AGARD, Turbomachinery Design Using CFD 44 p (SEE N95-14127 03-34)* (May 1994).

[39] Irwin H.P.A.H. , Cooper K.R., Girard R. Correction of distortion effects caused by tubing systems in measurements of fluctuating pressures. *Journal of Industrial Aerodynamics 5* (1979), 93–107.

[40] Ito, S., Goldstein, R., and Eckert, E. Film cooling of a gas turbine blade. *Journal of Engineering for Power 100* (1978), 476.

[41] J. Ruud van Ommen, C. Scouten, M. vander Stappen, M. van den Bleek. Response characteristic of probe-transducer system for pressure measurements in gas-solid fluidized beds: how to prevent pitfalls in dynamic pressure measurements. *Powder Technology 106* (1999), 199–218.

[42] J.P.A.J. van Beeck, C. Benocci. *CN 168 - Spectral Analysis of Turbulent Flows.* von Karman Institute, 2012.

[43] Kadotani, K., and Goldstein, R. Effect of mainstream variables on jets issuing from a row of inclined round holes. *Journal of engineering for power 101* (1979), 298.

[44] King, L. On the convection of heat from small cylinders in a stream of fluid: determination of the convection constants of small platinum wires, with applications to hot-wire anemometry. *Proceedings of the Royal Society of London. Series A 90*, 622 (1914), 563–570.

[45] Lakshminarayana, B. *Fluid Dynamics and Heat Transfer of Turbomachinery*. Wiley Online Library, 1996.

[46] Liess, C. Experimental investigation of film cooling with ejection from a row of holes for the application to gas turbine blades. *Journal of Engineering for Power 97* (1975), 21.

[47] Ligrani, P. Aerodynamic losses in turbines with and without film cooling, as influenced by mainstream turbulence, surface roughness, airfoil shape, and mach number. *International Journal of Rotating Machinery 2012* (2012).

[48] M., P. The Hallcrest handbook of thermochromic liquid crystal technology. *Hallcrest, Glenview* (1991).

[49] Marvin, J. G. Wind tunnel requirements for computational fluid dynamics code verification. *NASA STI/Recon Technical Report N 87* (July 1987), 27150.

[50] M.V. Morkovin. Fluctuations and Hot-Wire Anemometry in Compressible Flows. AGARDograph 24, AGARD, 1954.

[51] N. Gourdain, F. Duchaine, L. Gicquel, E. Collado. Advanced Numerical Simulation Dedicated to the Prediction of Heat Ttansfer in a Highly Loaded Turbine Guide Vane. In *Proceeding to ASME TURBO EXPO Conference* (2010), ASME.

[52] Nagabushana, K., and Stainback, P. Heat transfer from cylinders in subsonic slip flows. *NASA STI/Recon Technical Report N 92* (Feb. 1992), 21248.

[53] Osnaghi, C., Perdichizzi, A., Savini, M., Harasgama, P., and Lutum, E. Influence of film-cooling on the aerodynamic performance of a turbine nozzle guide vane. In *The 1997 International Gas Turbine & Aeroengine Congress & Exposition* (1997).

[54] P., C. Introduction to Signal and Image Processing. Digital image fundamentals, MIAC University of Basel, 2012.

[55] Paniagua G. , Dénos R. Digital compensation of pressure sensors in the time domain. *Experiment in Fluids 32* (2002), 417–424.

[56] P.C. Valente, J.C. Vassilicos. The decay of turbulence generated by a class of multi-scale grids. *Journal of Fluid Mechanics* (2011).

[57] Pedersen, D., Eckert, E., and Goldstein, R. Film cooling with large density diffferences between the mainstream and the secondary fluid measured by the heat-mass transfer analogy. *ASME Transactions Journal of Heat Transfer 99* (1977), 620–627.

[58] Perdichizzi, A. Mach number effects on secondary flow development downstream of a turbine cascade. *Journal of turbomachinery 112*, 4 (1990), 643–651.

[59] Persico, G., Gaetani, P., Dossena, V., D'Ippolito, G., and Osnaghi, C. On the definition of the secondary flow in three-dimensional cascades. *Proceedings of the Institution of Mechanical Engineers, Part A: Journal of Power and Energy 223*, 6 (2009), 667–676.

[60] P.L. O'Neil, D. Nicolaides, D. Honnery and J. Soria. Autocorrelation functions and the determination of integral length with reference to experimental and numerical data. In *15th Australian Fluid Mechanic Conference* (2004).

[61] Polanka, M., Witteveld, V, C., and Bogard, D. Film cooling effectiveness in the showerhead region of a gas turbine vane part i: Stagnation region and near-pressure side. *ASME Paper* (1999), 48.

[62] P.T., I., and T.V., J. The response time of a surface thermometer employing encapsulated thermochromic liquid crystals. *Journal of Physics E: Scientific Instruments 20*, 10 (1987), 1195.

[63] R. Theunissen, A. Di Sante, M.L. Riethmuller, R.A. Van de Braembussche. Confidence estimation using dependent circular block bootstrapping: application to the statistical analysis of PIV. *Experiments in Fluids* (2008).

[64] S. Ravelli. Indagine aerodinamica e termica su una palettatura rotorica con endwall raffreddato mediante film cooling. Contract report addendum, Energy Systems and Turbomachinery Laboratory - Bergamo University, 2011.

[65] Sacher, P., Bradley Jr, R., and Schmidt, W. Validation of computational fluid dynamics. *NASA STI/Recon Technical Report N 89* (1989), 27104.

[66] Sauer, H., Müller, R., and Vogeler, K. Reduction of secondary flow losses in turbine cascades by leading edge modifications at the endwall. *Journal of turbomachinery 123*, 2 (2001), 207–213.

[67] Schmidt, D., and Bogard, D. Effects of Free-Stream Turbulence and Surface Roughness on Film Cooling. In *Proceedings of the ASME Turbo Expo 1996 Conference* (1996), no. 462 in 96-GT, ASME.

[68] Schmidt, D., and Bogard, D. Effects of Free-Stream Turbulence and Surface Roughness on Laterally Injected Film Cooling. *ASME-PUBLICATIONS-HTD 350* (1997), 233–244.

[69] Schultz and Jones. Heat-Transfer Measurements in Short-Duration Hypersonic Facilities. AGARDograph 165, AGARD, 1973.

[70] Sharma, O., and Butler, T. Predictions of endwall losses and secondary flows in axial flow turbine cascades. *Journal of turbomachinery 109*, 2 (1987), 229–236.

[71] Sieverding, C. Recent progress in the understanding of basic aspects of secondary flows in turbine blade passages. *Journal of Engineering for Gas Turbines and Power 107*, 2 (1985), 248–257.

[72] Sillekens, J., Rindt, C., and van Steenhoven, A. Development of laminar mixed convection in a horizontal square channel with heated side walls. *International Journal of Heat and Fluid Flow 19*, 3 (1998), 270 – 281.

[73] Sinha, A., Bogard, D., and Crawford, M. Film cooling effectiveness downstream of a single row of holes with variable density ratio. In *ASME, 35th International Gas Turbine and Aeroengine Congress and Exposition* (1990), vol. 1.

[74] Stephen B. Pope. *Turbulent Flows.* Cambridge University Press, 2000.

[75] T. Takahashi, T. Arts, T. Verstraete, J. Prinsier. Benchmark Simulation of RANS CFD for Heat Transfer Evaluation on the VKI LS89 Blade. In *Proceeding to the IGTC Conference* (2011), AIAA.

[76] Thole, K., Sinha, A., Bogard, D., and Crawford, M. Mean temperature measurements of jets with a crossflow for gas turbine film cooling application. In *Rotating Machinery - Transport Phenomena;* (1992), J. H. Kim and W.-J. Yang, Eds., pp. 69–85.

[77] Wagner, E., and Stephan, P. Frequency response of a surface thermometer based on unencapsulated thermochromic liquid crystals. *Experimental Thermal and Fluid Science 31*, 7 (2007), 687 – 699.

[78] Wang, H.-P., Olson, S. J., Goldstein, R. J., and Eckert, E. R. Flow visualization in a linear turbine cascade of high performance turbine blades. *Journal of turbomachinery 119*, CONF-950629– (1997).

[79] W.D., W. 50 years of the 1931 CIE standard observer for colorimetry. In *AIC Color* (1981), vol. 81.

[80] Yasa, T., Paniagua, G., and Dénos, R. Hot wire anemometry for non-isothermal flows and effects of aging of the sensor wire. In *Data Acquisition and Signal Processing for Turbomachinery Applications* (2005), von Karman Institute for Fluid Dynamics, Ed.

[81] Zess, G., and Thole, K. Computational design and experimental evaluation of using a leading edge fillet on a gas turbine vane. *Transactions of the ASME-T-Journal of Turbomachinery 124*, 2 (2002), 167–175.